



Fatigue and Fracture Assessment of Butt Welded Joints and Thermal Cut Edges under Axial and Bending Loads

Jorge Duarte Benther

Master Thesis

presented in partial fulfillment
of the requirements for the double degree:
“Advanced Master in Naval Architecture” conferred by University of Liege
“Master of Sciences in Applied Mechanics, specialization in Hydrodynamics,
Energetics and Propulsion” conferred by École Centrale de Nantes

developed at University of Rostock, Rostock
in the framework of the

**“EMSHIP”
Erasmus Mundus Master Course
in “Integrated Advanced Ship Design”**

Ref. 159652-1-2009-1-BE-ERA MUNDUS-EMMC

Supervisor: Prof. Patrick Kaeding, University of Rostock

Internship Supervisor: Dr. Hubertus von Selle, DNV GL Hamburg

Reviewer: Prof. Maciej Taczala, West Pomeranian University of Technology

Rostock, February 2016



ABSTRACT

The aim of this work is to provide a research for fatigue of structures applied on container vessels. Considerable increase on size and capacity of container ships has led to the utilization of thicker plates and higher tensile materials. For instance, it is highly observed on upper flange, especially hatch corners, and also for butt welds. This work intends to verify the influence of internal flaws on butt welded joints for different loading types on thick plate; and to check the consequences on fatigue life of thermal cut edges considering distinct in service edge treatments, materials, loading type and plate thickness.

For the first part, experimental fatigue tests previously carried out by DNV GL for several butt welded joints specimens with thickness of 50 mm made of high tensile material with pre-established internal defect were considered for analysis. In each specimen, the lack of fusion was measured by ultrasonic test and, after cyclic loading test, the S-N curve is obtained. Linear elastic fracture mechanics approach is used to simulate one selected specimen and the results are compared. Parameters of *Paris-Erdogan* equation are taken from well-known references. Differences between pure axial and pure bending loads are verified, including a comparison with literature. Embedded elliptical crack model with same area of the actual internal lack of fusion can represent the expected life of the specimen. It is shown that IIW2008 parameters are much more conservative than the parameters taken from DNV GL butt welded joints lab tests; also that the specimen subjected to pure bending load presents higher life than when only axial acting load is applied. On the other hand, a deeper research for fatigue enhancement due to bending needs to be carried out for internal defects.

Second part of this work presents a finite element analysis of specimens with distinct thicknesses and different edge treatments established after thermal cut procedure is adopted. Analytical calculation for no edge treatment is determined and kept as reference value for axial and bending cases. Stress concentration and maximum stresses influenced by various edge treatments are determined for pure axial and pure bending loads, including a comparison between the different edge treatments. Later on, fracture mechanics analysis is performed providing a reliable outcome about the fatigue life for different crack models that are considered to simulate actual cracks evidenced on previous tests and references, along with a small initial crack size that was carried out for axial and bending loads. Parameters for base material are obtained from notable reference and results from this analysis will be used by DNV GL in the future, in which the simulation results achieved herein will be confronted

with the experimental tests. Comparison between axial and bending is once more performed for each crack model. Lastly, a real case scenario investigated by fracture mechanics based on GL report, standards and guidelines considering variable loads using straight line spectrum is also included. No considerable difference was observed for notch stress on the specimen due to edge treatment. Simulation for corner crack model presented more impact in fatigue life of materials than semi-elliptical surface crack model; for same material and crack model, thicker specimens achieved higher fatigue life; and high tensile materials results are not completely agreeing with formulation based on classification societies standards, thus further analysis is proposed. Influence on lifetime of container ship's structures due to different crack sizes and models is verified for variable loads, leading to better consideration on inspection and maintenance.

Finally, conclusions are summarized for both parts of this research and future works are recommended, along with all references that were used on the elaboration of this master thesis.

CONTENTS

ABSTRACT	3
TABLE OF FIGURES	7
TABLE OF TABLES	9
DECLARATION OF AUTHORSHIP	10
1. INTRODUCTION.....	11
1.1 EVOLUTION OF CONTAINERSHIPS	12
1.2 MATERIALS USED ON HIGH CAPACITY CONTAINERSHIPS	14
1.3 FATIGUE ANALYSIS OF CONTAINERSHIPS	14
1.4 THERMAL CUTTING	16
1.5 BUTT WELDED JOINTS AND THERMAL CUT EDGES	17
1.6 ORGANIZATION OF THE MASTER THESIS	18
2. BASIC THEORY	19
2.1 BASIC FATIGUE PRINCIPLES	19
2.2 FRACTURE MECHANICS.....	21
3. FRACTURE ASSESSMENT SIMULATION.....	25
3.1 SIMULATION FOR SPECIMEN 18	29
3.1.1 <i>Simulation Input Data for Fraunhofer IWM VERB</i>	29
3.1.2 <i>Results for Pure Axial Load with Constant Stress</i>	30
3.1.3 <i>Results for Pure Bending Load with Constant Stress</i>	33
3.1.4 <i>Results for Pure Bending Load for Constant Number of Cycles</i>	34
3.1.4.1 <i>Comparison to Maddox</i>	36
4. THERMAL CUT EDGES ANALYSIS	39
4.1 ANALYTICAL RESULT.....	40
4.2 LOADS AND BOUNDARY CONDITIONS FOR 2D AND 3D ANALYSES	43
4.2.1 <i>Symmetry Evaluation of Specimen</i>	43
4.2.2 <i>Boundary and Load for 2D and 3D Axial Analysis</i>	45
4.2.3 <i>Boundary and Load for 2D and 3D Bending Analysis</i>	46
4.3 2D MODEL PLAIN STRESS ANALYSIS	47
4.3.1 <i>2D Mesh Convergence</i>	47
4.3.2 <i>2D Model – Tensile Simulation</i>	47
4.3.3 <i>2D Model – Bending Simulation</i>	48
4.4 3D MODEL SOLID ANALYSIS.....	49
4.4.1 <i>3D Mesh Convergence Analysis</i>	49
4.4.2 <i>3D Model – Tensile Simulation</i>	50
4.4.2.1 <i>3D Model Thickness 80mm 3C – Tensile Simulation</i>	50
4.4.2.2 <i>3D Model Thickness 50mm 3C – Tensile Simulation</i>	50

4.4.2.3	<i>3D Model Thickness 25mm 3C – Tensile Simulation</i>	50
4.4.2.4	<i>Summary of 3D Model Results for Tensile Simulation</i>	51
4.4.3	<i>3D Model – Bending Simulation</i>	53
4.4.3.1	<i>3D Model Thickness 80mm 3C – Bending Simulation</i>	53
4.4.3.2	<i>3D Model Thickness 50mm 3C – Bending Simulation</i>	53
4.4.3.3	<i>3D Model Thickness 25mm 3C – Bending Simulation</i>	53
4.4.3.4	<i>Summary of 3D Model Results for Bending Simulation</i>	54
4.5	CRACK PROPAGATION ANALYSIS OF THERMAL CUT EDGE SPECIMEN	56
4.5.1	<i>Thermal Cut Edge Crack Propagation Analysis for Axial Load</i>	57
4.5.1.1	<i>Thermal Cut Edge Quarter Corner Crack Results for Axial</i>	57
4.5.1.2	<i>Thermal Cut Edge Semi-Elliptical Crack Results for Axial</i>	61
4.5.2	<i>Thermal Cut Edge Crack Propagation Analysis for Bending Load</i>	62
4.5.2.1	<i>Thermal Cut Edge Quarter Corner Crack Results for Bending</i>	62
4.5.2.2	<i>Thermal Cut Edge Semi-Elliptical Crack Results for Bending</i>	62
4.6	COMPARISON BETWEEN AXIAL AND BENDING LOADS FOR THERMAL CUT EDGES.....	63
4.6.1	<i>Crack Propagation Comparison for Quarter-Elliptical Crack</i>	63
4.6.2	<i>Crack Propagation Comparison for Semi-Elliptical Crack</i>	64
4.7	FRACTURE ASSESSMENT UNDER VARIABLE LOAD	65
4.7.1	<i>Crack Propagation for Quarter Corner Crack under Variable Load</i>	69
4.7.2	<i>Crack Propagation for Semi-Elliptical Crack under Variable Load</i>	70
4.7.3	<i>Crack Propagation for Extended Surface Crack under Variable Load</i>	71
5.	CONCLUSION	72
6.	ACKNOWLEDGEMENTS	73
7.	REFERENCES.....	74

TABLE OF FIGURES

Figure 1 – Growth of Containership (1956-2007) (Rizvi 2011)	12
Figure 2 – Evolution in Containership Fleet (Ashar, A. and Rodrigue, J.-P. 2012)	13
Figure 3 – Monthly Index of World Trade Advanced and Emerging Economies (Brooks, Pallis, T. and Perkins, S. 2013)	13
Figure 4 – Hatch Coaming Sketch	15
Figure 5 – Oxy-Fuel Cutting, Plasma Cutting and Laser Metal Cutting.....	16
Figure 6 – Schematic of Material Fatigue (Radaj, Sonsino, C. M. and Fricke, W. 2006)	19
Figure 7 – Crack and Failure Examples (Moore, P. and Booth, G. 2015)	20
Figure 8 – Examples of Fatigue Failures: Propeller Shaft and Amidship of a Tanker (Lassen, T. and Récho, N. 2006)	20
Figure 9 – Example of S-N Curve for Thickness Investigation on Butt Welded Joints (Pedersen, Andersen, J. G. and Ólafsson, Ó. M. 2012).....	21
Figure 10 – Different Modes of Crack Extension (Hertzberg 1996)	22
Figure 11 – Fracture Mechanics Fatigue Crack Growth Relationship (Maddox 2003).....	23
Figure 12 – Dimensions of Specimen (DNV GL 2015).....	25
Figure 13 – Angular Distortion of Specimen (DNV GL 2015)	25
Figure 14 – Milling of the Camping Area (DNV GL 2015)	26
Figure 15 – Location of Internal Defect for Specimen 18 by UT (DNV GL 2015)	26
Figure 16 – Coordinate System for UT Indications of Specimens (DNV GL 2015).....	26
Figure 17 – Crack Surface Result for Specimen 18 after Testing (DNV GL 2015)	27
Figure 18 – Strain Gauges Position and Measurement for Spec. 18 (DNV GL 2015)	27
Figure 19 – Test Results S-N Curves (DNV GL 2015)	28
Figure 20 – Sketch of Geometries for Each Test and Crack Model from <i>Fraunhofer IWM Verb (Fraunhofer 2008a, 2008b)</i>	30
Figure 21 – Specimen 18 Crack Propagation for Each Model in Axial Load	31
Figure 22 – Simulation Results for Crack Propagation of Specimen 18 for Pure Axial Load	32
Figure 23 – Crack Propagation for Pure Axial and Bending Loads with Same Stress Range.	34
Figure 24 – Crack Propagation in Specimen 18 for each Model under Bending Load	35
Figure 25 – Crack Propagation for Bending with Same Number of Cycles of Axial.....	36
Figure 26 – Effect of Degree of Bending on Relative Fatigue Strength of Joints Failing from Weld Toe as Determined Using Fracture Mechanics (Maddox 2015).....	37
Figure 27 – Weld Geometry taken from Fricke, W. and Paetzold, H. (2012)	38
Figure 28 – Comparison Result from Fracture Mechanics Simulation with Available Literature	38
Figure 29 – Edge Treatment Identification	39
Figure 30 – Thermal Cut Edge Specimen Geometry	39
Figure 31 – Identification of Lines 1-2 and Points 3-4 for Stress Values	41
Figure 32 – SCFs K_m for a Flat Test Specimen with Opposite Shallow U-Shaped Notches in Tension	42
Figure 33 – SCFs K_m for Bending of a Flat beam with Opposite Shallow U Notches	43
Figure 34 – Complete 2D and 3D Model Stress Result for Axial and Bending	44
Figure 35 – Complete 2D and 3D Model Strain Result for Axial and Bending	44
Figure 36 – Load and Boundary Conditions Configuration for 2D and 3D Axial.....	45
Figure 37 – Additional Boundary Condition for 3D	46
Figure 38 – Load and Boundary Conditions Configuration for 2D and 3D Bending	46
Figure 39 – Convergence Analysis Result for 2D Axial.....	47
Figure 40 – Convergence Stress Result for 2D Axial	48

Figure 41 – Convergence Stress Result for 2D Bending	48
Figure 42 – Convergence Analysis Result for 3D Axial.....	49
Figure 43 – Subdivision of Mesh for 3C Edge Treatment Surface	49
Figure 44 – Result for 3D Axial 3C with Thickness 80mm.....	50
Figure 45 – Result for 3D Axial 3C with Thickness 50mm.....	50
Figure 46 – Result for 3D Axial 3C with Thickness 25mm.....	51
Figure 47 – Summary of Stress Result adopting FE for 3D Axial.....	51
Figure 48 – Stress Distribution for 3C Thickness 80mm under Axial Load.....	52
Figure 49 – Stress Distribution Values for 3C under Axial Load.....	52
Figure 50 – Result for 3D Bending 3C with Thickness 80mm.....	53
Figure 51 – Result for 3D Bending 3C with Thickness 50mm.....	53
Figure 52 – Result for 3D Bending 3C with Thickness 25mm.....	54
Figure 53 – Summary of Stress Result adopting FE for 3D Bending.....	54
Figure 54 – Stress Distribution for 3C Thickness 80mm under Bending Load.....	55
Figure 55 – Stress Distribution Values for 3C under Bending Load.....	55
Figure 56 – Sketch for Specimen Geometries and Stress Distribution.....	57
Figure 57 – Quarter Corner Crack Depth Propagation for YP36 for Different Stress Ranges under Axial Load.....	58
Figure 58 – Quarter Corner Crack Length Propagation for YP36 for Different Stress Ranges under Axial Load.....	58
Figure 59 – Quarter Corner Crack Depth Propagation for YP40 for Different Stress Ranges under Axial Load.....	59
Figure 60 – Quarter Corner Crack Length Propagation for YP40 for Different Stress Ranges under Axial Load.....	59
Figure 61 – Quarter Corner Crack Depth Propagation for YP47 for Different Stress Ranges under Axial Load.....	60
Figure 62 – Quarter Corner Crack Length Propagation for YP47 for Different Stress Ranges under Axial Load.....	60
Figure 63 – Summary of Quarter Corner Crack Propagation for TCE under Axial	61
Figure 64 – Summary of Semi-Elliptical Crack Propagation for TCE under Axial Load	61
Figure 65 – Summary of Quarter Corner Crack Propagation for TCE under Bending Load ..	62
Figure 66 – Summary of Semi-Elliptical Crack Propagation for TCE under Bending Load ..	63
Figure 67 – Crack Propagation Comparison for Quarter Corner TCE under Axial Load	64
Figure 68 – Crack Propagation Comparison for Semi Elliptical TCE under Axial Load.....	64
Figure 69 – Standard Stress Range Spectra A, B and C (Germanischer Lloyd 2015).....	65
Figure 70 – Part of Catalogue of Details for Unwelded Base Materials and f_n Factor (Germanischer Lloyd 2015)	66
Figure 71 – Part of Factor f_n Table (Germanischer Lloyd 2015).....	66
Figure 72 – Graphical Summary of Variable Stress Values	68
Figure 73 – Crack Propagation for Quarter Corner Crack under Variable Load.....	69
Figure 74 – Crack Propagation for Semi-Elliptical Crack under Variable Load.....	70
Figure 75 – Crack Propagation for Extended Surface Crack under Variable Load.....	71

TABLE OF TABLES

Table 1 – Structural for Fatigue Evaluation of Containers Carries (DNV 2014)	15
Table 2 – Test Results for All Specimens (Except Specimen 23)	28
Table 3 – Test Results for Specimen (Run Out)	28
Table 4 – Common Parameters of Specimen 18	29
Table 5 – Parameters for Simulation of Specimen 18 on <i>Fraunhofer IWM VERB</i>	29
Table 6 – Comparison between Experimental and Simulation Results for Specimen 18.....	33
Table 7 – Results for Pure Axial and Bending Loads with Same Stress Range	34
Table 8 – Results for Pure Axial and Bending Loads with Same Number of Cycles for Each Model	35
Table 9 – Material Properties for FEM Investigation of Thermal Cut Edge Specimen.....	40
Table 10 – Nominal Stress for Tensile and Bending	41
Table 11 – Stress Concentration Factor Result for 3D under Axial Load	52
Table 12 – Stress Concentration Factor Result for 3D under Bending Load.....	55
Table 13 – <i>Paris-Erdogan</i> Parameters for Thermal Cut Edges Simulation (Berger et al. 2009)	56
Table 14 – Stress Values Adopted for Crack Propagation of Thermal Cut Edges	56

DECLARATION OF AUTHORSHIP

I declare that this thesis and the work presented in it are my own and have been generated by me as the result of my own original research.

Where I have consulted the published work of others, this is always clearly attributed.

Where I have quoted from the work of others, the source is always given. With the exception of such quotations, this thesis is entirely my own work.

I have acknowledged all main sources of help.

Where the thesis is based on work done by myself jointly with others, I have made clear exactly what was done by others and what I have contributed myself.

This thesis contains no material that has been submitted previously, in whole or in part, for the award of any other academic degree or diploma.

I cede copyright of the thesis in favour of the University of Rostock.

Date:

Signature

1. INTRODUCTION

As usual practice of ship industry, strength analysis is performed mostly considering design loads under static condition (Fricke, Petershagen, H. and Paetzold, H. 1998a). However, it is highly noted that fluctuation on time and variation of some parameters, such as applied stress, can seriously affect structural elements. Consequences can be observed, not only on ships, but also on many naval and marine structures that are as well influenced by local loads or surroundings, *e.g.* wind turbines, wave energy converters and several others.

Sea waves, propulsion system and cargo condition, among others can arise stresses that are repeated throughout the lifetime of the ship and structures. It can be highlighted the fact that these stresses are mostly below the stress necessary to determine the failure of the structure, nevertheless it is possible to generate non-reversible small damage in the material along each cycle. Therefore, it is verified a decrease on strength to resist the acting loads due to accumulated damage.

What was briefly explained before is the so-called fatigue, also known as a failure behavior and a basic known type of failure mode (Rigo, P. and Rizzutto, E. 2003), which will be given more information in Subsection 2.1.

Some other aspects can amplify the influence on fatigue strength, such as corrosion and temperature related to environmental conditions; shape, size and dimensions with respect to structural member; roughness, hardness and residual stress for surface aspects; material, cut edge procedure and edge treatment, among others that are evidentially combined with loading type and ship's course (Radaj, Sonsino, C. M. and Fricke, W. 2006).

According to Moraitis (2014) and previously published by Battelle Columbus Laboratories (1983) and National Corrosion Service (1983), around 90% of mechanical service failures is due to fracture and considerable cost has been evidenced about material fracture. Fatigue plays an important role in that statistic, where its consequences are verified in most of the moving components or parts of mechanical systems, which shows the importance of the subject and also the motivation for researches and seek of solutions, in order to overcome such problem and minimize its cost.

As result for the investigation on fatigue field, one concludes that it is not possible to assist all the structural analysis based on the engineering conventional concept of adopting safety factors or acceptable stress ranges. For currently structural problems, considering advances on engineering fields especially for high strength materials and including also the increase on thick plate for high/low cyclic loads, one must perform deep research for fatigue and establish

improvements, placing more importance in special cases such as the design of details like welded joints and hatch corners of container ships. This type of ship is highly affected by its constant evolution on capacity and size growth.

1.1 Evolution of Containerships

Containerships have a huge importance in the worldwide goods trade and they are also considered to be a helpful key element to the world globalization. The first containership was a converted tanker attributed to Malcom McLean (Cudahy 2006) and, since then, the growth of such type of vessel presents a considerable rate, as observed in Figure 1.

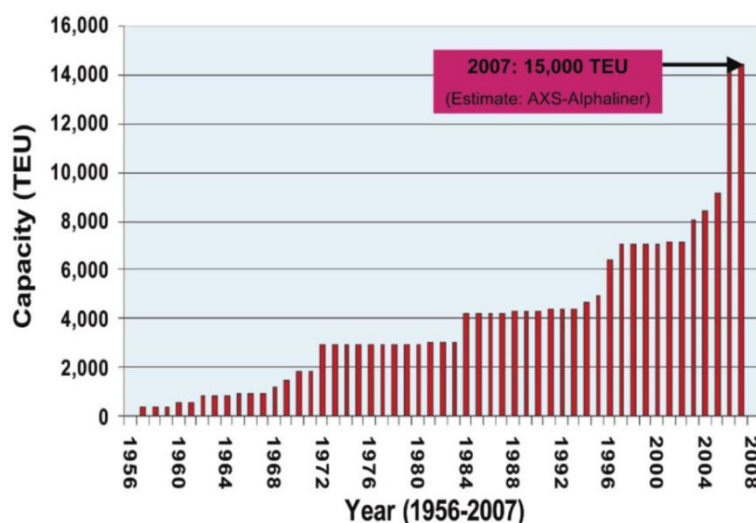


Figure 1 – Growth of Containership (1956-2007) (Rizvi 2011)

Evolution and different classes of containerships are verified in Figure 2, where in 2005 the containership fleet presented a preponderant capacity compared to others general cargo classes by that time (Montes, Seoane, M. J. F. and Laxe, F. G. 2012).

For future years, the containerships are expected to increase in size and capacity, based on information provided by Brooks, Pallis, T. and Perkins, S. (2013) and as seen in Figure 3 about the increase on world trade of goods, which are mostly performed by containerships, obviously depending on the status of world economy (Altena 2013).

As mentioned above, the growth in the container traffic motivates the increase on the capacity of the containerships and ship owners are choosing higher classes of ships, due to less cost in goods transportation. On the other hand, some limitations can be found for larger sizes of the containerships, which are mainly because of geographical (Brooks, Pallis, T. and Perkins, S. 2013) and then technical.

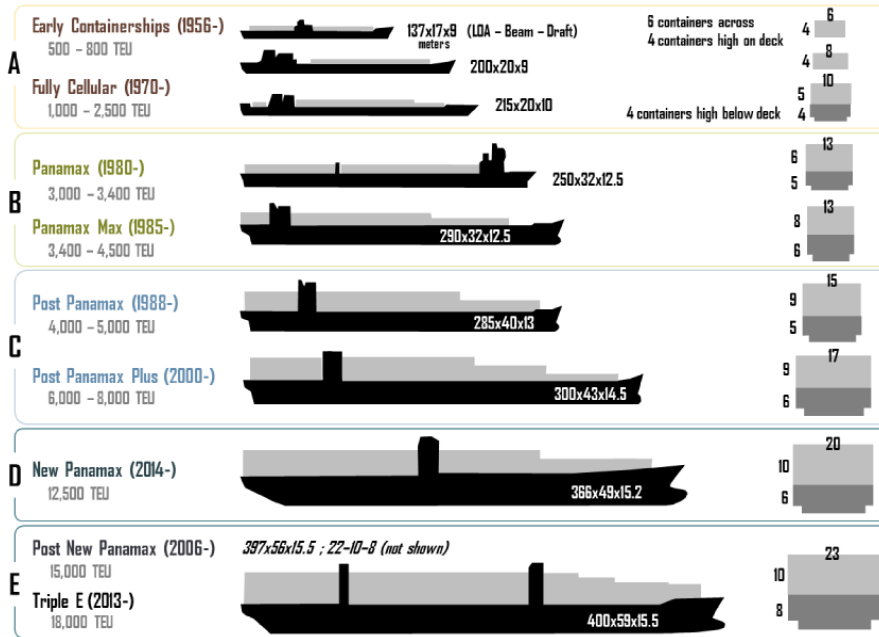


Figure 2 – Evolution in Containership Fleet¹ (Ashar, A. and Rodrigue, J.-P. 2012)

About the first limitation, the port infrastructure plays an important role. Also, it should be considered the allowed routes considering the draft of larger vessels and port capacity. The latter restraint is considered in this work, mostly as result of the utilization of thicker plates made of high tensile material that can be obtained also by thermal cut techniques applied on containership as exemplified in some works (Lotsberg 2014; Doerk, O. and Rörup, J. 2009; Li, G. and Wu, Y. 2010) and for being a complex subject for classification societies (Fricke et al. 2002), therefore the need for a more accurate analyses on fatigue assessment of such structures is crucial.

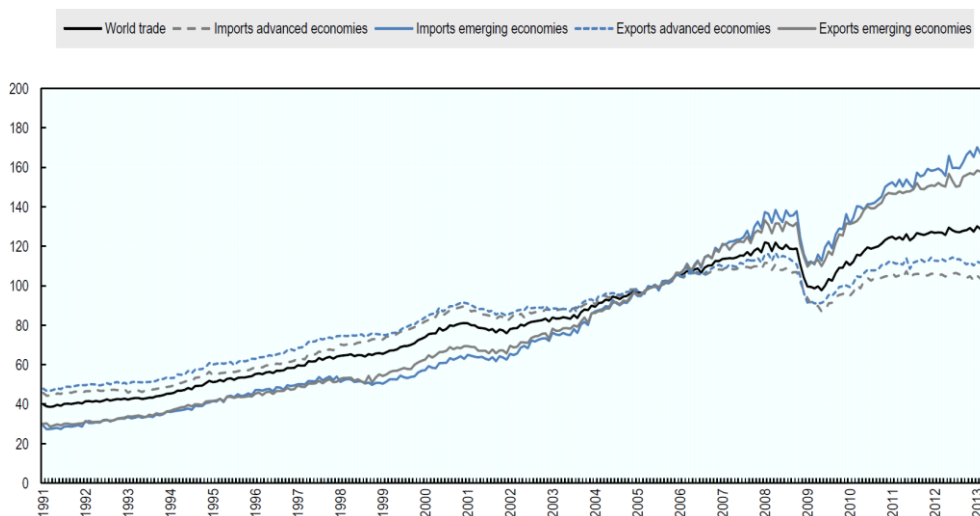


Figure 3 – Monthly Index of World Trade Advanced and Emerging Economies (Brooks, Pallis, T. and Perkins, S. 2013)

¹ Dimensions in meters; LOA is length overall.

1.2 Materials Used on High Capacity Containerships

Maritime industry had a significant development for the past years. For the ship sector, it is directly connected to the increase on the size and thus in capacity of the recent constructed vessels, in which was given special attention to tankers, bulk carriers and, mainly, containerships.

Due to this fact, the utilization of materials with higher mechanical properties has been widely adopted, also considering the increment on the thickness of plates, initially on deck, where more complex structures are likely to present imperfections and stress concentration regions (Chakarov, Garbatov, Y. and Soares, C. G. 2008; Fricke, Petershagen, H. and Paetzold, H. 1998b), then bottom in order to increase hull girder strength and, subsequently, in local structures. Thereat, the fatigue issue has turn into a concern for big containerships (DNV 2014).

Slightly new steel material has been applied to withstand loads acting in containerships, exemplified by YP36 (355 N/mm²), GL E40 (Selle et al. 2011) and YP40 (390 N/mm²) and YP47 steel (460 N/mm²) (IACS 2013a, 2013b), among others. These strong and good weld ability materials have yield point above 355 N/mm² and are examples used by some shipyards in order to turn possible the utilization of extremely thick plates and withstand the acting loads (MarineLink.com 2008).

1.3 Fatigue Analysis of Containerships

As observed from acquired experience from classification society, fatigue damages may occur with more frequency for some types of ship than others, also for some kind of categories of hull structure elements.

There is a relation between fatigue life and the magnitude of the dynamic stress level, including also the external environmental effect like corrosiveness of the surroundings, and the magnitude of notch and stress concentration factors of the structural details, considered to be different according to the type of ship or structure. Each type of ship will present possible fatigue damage with respect to the number of inherent damage locals.

As described in DNV (2014), highest percentage of fatigue damages on ship structures may be assigned on the tank boundaries of ballast and cargo tanks; and in panel stiffeners, side and bottom of the ship. In containership case, it is highly important to pay attention to the coaming and coaming top plate (Selle et al. 2011; Selle, Doerk, O. and Scharrer, M. 2009;

Germanischer Lloyd 2011). Therefore, depending on the type of stiffeners used and detail design (connection to supporting girder webs and bulkheads) the calculated fatigue life can change accordingly.

For the influence of sea, the dynamic wave loading on the hull is function of draught and load distribution. Thus, one must consider more than one loading condition in the fatigue assessment. Obviously, one should take into account the most frequently adopted situation of the ship for cargo and ballast condition. Normally, values of fraction of the conditions are provided or estimated, reflecting the operational trading pattern of the ship.

Once more adopting the containership example with the information provided by DNV (2014), one can elucidate on Table 1 the following structural elements in the cargo area that are more affected and hence should be considered for fatigue evaluation of containerships.

Table 1 – Structural for Fatigue Evaluation of Containers Carries (DNV 2014)

Hull Member	Structural Detail
Side and bottom longitudinal	Butt joints and attachment to transverse webs, transverse bulkheads and intermediate longitudinal girders
Upper deck	Plate and stiffener butt joints, hatch corner curvatures and support details welded on upper deck for container pedestals, among others

Hatch corners have been verified as structure likely to present fatigue damage, thus it is recommended to investigate such region for stress concentration and fatigue behavior. As observed in Figure 4, hatch coaming is defined as a raised rim of vertical plating around a hatchway to prevent entrance of water, the upper edge of which forms a sealing surface with the hatch-lid or cover.

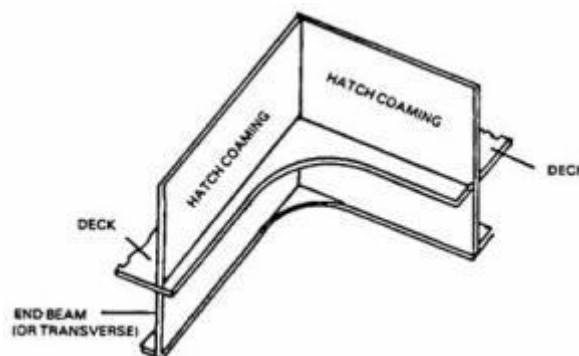


Figure 4 – Hatch Coaming Sketch²

² <http://officerofthewatch.com/tools/maritime-dictionary/>

1.4 Thermal Cutting

Thermal cutting processes are applied to produce components, plates, prepare welding edges, to obtain sophisticated structures and also structural parts that can be assembled later on. This technique is widely used in several different fields, especially to provide material for shipyards and others maritime and mechanical industries, in order to later on produce ships, cars, wind turbines and platforms, among others.

In summary as stated in literature (DIN 2003; ISF Welding and Joining Institute 2005), the cutting process can be classified according to the involved physics, such as:

- flame cutting, in which the material is mostly oxidized (burnt);
- fusion cutting, where the material is primarily fused; and
- sublimation cutting, in which the material is essentially evaporated.

Ejection procedure for the molten material or slag is mostly provided by a gas jet and/or evaporation expansion.

Energy involved in thermal cutting processes can be by use of gas, electrical gas discharge or beams, in which respectively some examples are observed in Figure 5 using oxy-fuel, plasma technique and laser cutting approach.



Figure 5 – Oxy-Fuel Cutting³, Plasma Cutting⁴ and Laser Metal Cutting⁵

Each technique presents advantages and disadvantages, including type of material that can be cut, precision of cutting, quality of cut surface and heat affected zone, cutting speed (Berglund 2006), thickness allowed to be cut, cost (VDI 3258 Blatt 2 1964), necessity of pre-treatment and post treatment of the cutting material, among several others.

Risk of cracking is inherent when thermal cutting process is used for cutting materials made of high strength steel, especially for thick plates and oxy-fuel cutting is adopted. The reason behind is the high quantity of heat transferred during the process, sometimes the bad quality of the surface after cutting or due to composition of the material, which can be more crack

³ <http://www.kerfdevelopments.com/oxy-fuel-cutting-machines/>

⁴ <http://www.lehtosenkonepaja.fi/www/news/machine-investment-thermal-cutting-machine/>

⁵ <http://www.rentapen.com/2012/01/05/laser-metal-cutting-services-verses-water-jet/>

susceptible, even more when heat modify the microstructural. Residual stresses are also non desirable consequences after thermal cutting, which increases with plate thickness and hardness of material (Berglund 2006).

When noticed, cracks are machined or a new better quality cut can be necessary. If the cut piece was supposed to be welded afterwards, joint preparation by machining is recommended (grinding). Edge treatments have been used for improving fatigue life of thick plates of high tensile material (Selle et al. 2011), including also ways to reduce the risk of cut edge cracking such as preheating, cutting speed control, controlled cooling temperature, among others.

1.5 Butt Welded Joints and Thermal Cut Edges

Welding is widely used as a versatile joining process by several industries. It has been observed welds from long time in the past, where the necessity to keep pieces together was accomplished by heating the material and assembling them by mechanical effort. Welding techniques have been improved and researches started to be decisive, in order to understand failures that were observed in civil and naval engineering (Moore, Booch 2015) and, then, being able to avoid the premature happening of them.

Following that improvement trend, massive welding rules, quality systems and standards have been developed and updated with objective of ensuring the safety of welds and welding procedures. Nonetheless, welds are still the main location in structures most susceptible to cracks and other defects, if not properly understood and prevent. Welds are associated with a number of other features such as residual stress and distortion, which should also be considered.

Basically, butt weld joints are type of joints in which the butting ends of two or more work pieces are aligned in approximately the same plane and welded together (American Institute of Welding 2010).

Fabrication of entire ships and structural elements are normally performed by assembling and welding plates and components that in some cases may need to be obtained from thermally cut bigger elements (AcerlorMittal 2015). It is also considered as a way to cut plates into shape and prepare welding grooves (Ruukki Metals Oy 2011). Hence, it is important to understand how the quality of the thermal cutting affects the fatigue strength of structure (Goldberg 1973).

In few words, thermal cut is understood as a group of cutting processes severing or removing metal by means of localized melting, burning, or vaporizing of the work pieces (American

Institute of Welding 2010). Commonly, one adopts flame, plasma or laser cuts techniques, as already verified in Figure 5.

In work performed by Goldberg (1973), it was studied the influence of several thermal cutting procedures on fatigue strength of steel material and also the surfaces roughness. Among the conclusions, many parameters can impact negatively the fatigue strength of thermal cut, especially defects in the thermal cut surfaces and the quality grade of surface.

It has been seen that for constant stress amplitude the benefit of post weld treatment is considerable (Selle et al. 2011) and also the edge preparation for high and ultra-high strength steels (Laitinen, Valkonen, I. and Kömi, J. 2013). However, it is still needed more investigation on the consequences for thicker plates and different type of edge treatment. Herein, only the effects of the edge preparation are investigated (notch).

1.6 Organization of the Master Thesis

The present work comprises seven Chapters in total.

Chapter 1 provides a general overview of the master thesis with its main objectives.

In Chapter 2, basic principles for fatigue and fracture mechanics are described in order to ease further chapters.

Chapter 3 intends to verify the influence of internal flaws on butt welded joints for different loading types on thick plate made of high tensile material by experimental fatigue analysis and fracture mechanics simulation approach.

In Chapter 4, research is carried out to check the consequences on fatigue life of thermal cut edges considering distinct in service edge treatments, materials, loading type and plate thickness. Initially, finite element analysis is performed to verify the influence of edge treatments and specimen thickness on stress intensity factor under axial and bending loads. Fracture mechanics approach is used to determine the lifetime of considered crack models, thickness and distinct high tensile materials. Lastly, fatigue lifetime is investigated under variable loads applied to real case scenario by fracture mechanics.

Along with future recommendations, a summary of main conclusions of the present study for all investigations is included in Chapter 5.

Chapter 6 is the acknowledgement; Chapter 7 gives all references used in the elaboration of this work and aside Appendices are provided with more information from Chapters 3 and 4.

2. BASIC THEORY

2.1 Basic Fatigue Principles

Fatigue was identified as a chronic industry problem in 19th century, after several observed occasions that happened in Europe and made the scientists start to investigate the reason why some components of structural facilities, like railroads and bridges, were cracking when subjected to repeat loadings. Furthermore, increase of metallic structures and components utilization was observed due to the improvements in the machinery production and even more failures like the previously mentioned ones were registered.

According to Selle (2014), benefits of knowledge and application of the fatigue assessment for the clients are mentioned below:

- Usage of structural components at a balanced level;
- Provide reliable ships; and
- Decrease the repair cost during service time of ship, becoming more competitive.

Fatigue can be simply described by the steps according to schematic as shown in Figure 6.

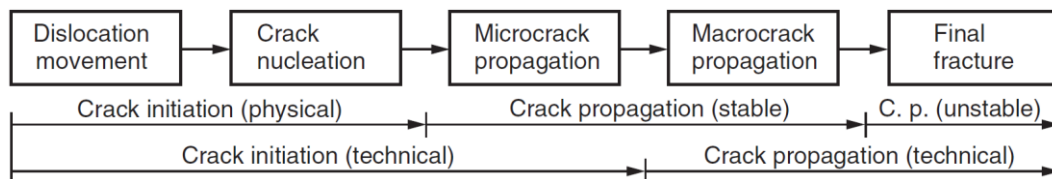


Figure 6 – Schematic of Material Fatigue (Radaj, Sonsino, C. M. and Fricke, W. 2006)

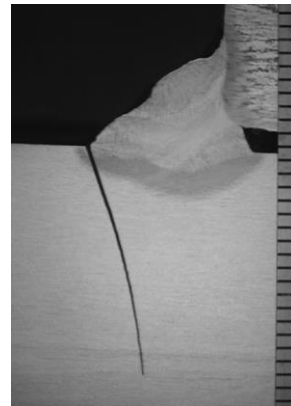
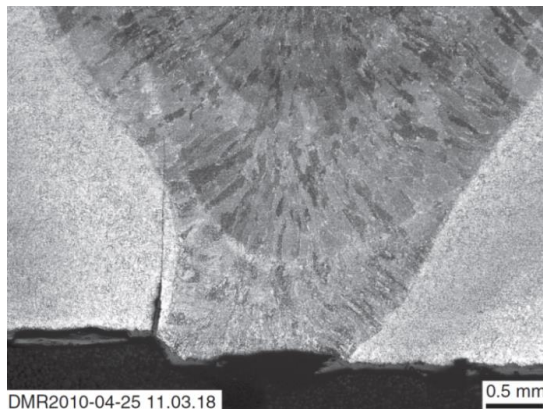
One can mention the main principles, such as:

- Crack Initiation Phase
 - During this phase, one may observe microscopic fatigue cracks being formed, as exemplified in Figure 7 (a), consequence of the accumulation from alternating plastic deformation. Thus, there are local structural changes that may also happen (microstructural changes, precipitation, among others); and
 - Afterwards, those macrocracks can originate more microcracks running along slip bands.
- Crack Propagation Phase
 - In this phase, the macrocracks present an increase following the direction of the most notable principal stress that may be influenced by stress concentration factor, among others. As mentioned by Fricke, Petershagen, H. and Paetzold, H. (1998a), the crack propagation rate is about the order of 10^{-8} and 10^{-3} mm per cycle. It is not perfectly guarantee that one will observe failure of the

structure in this phase, defining then the stable crack propagation. However, it can be seen inadmissible damage sometimes, such as leakage and others.

- Damage of the Structure

- Since the considered structure is deeply weakened and if no further action is embraced, one probably will observe the failure of the structure on future cycles (final fracture), as observed in Figure 7 (b).



(a) Crack Initiating at the Toe of the Weld Root (b) Fatigue Failure from the Toe of a Fillet Weld

Figure 7 – Crack and Failure Examples (Moore, P. and Booth, G. 2015)

Some examples of failures occurred in ship industry can be observed in Figure 8, which the consequences can be catastrophic and result in high cost.

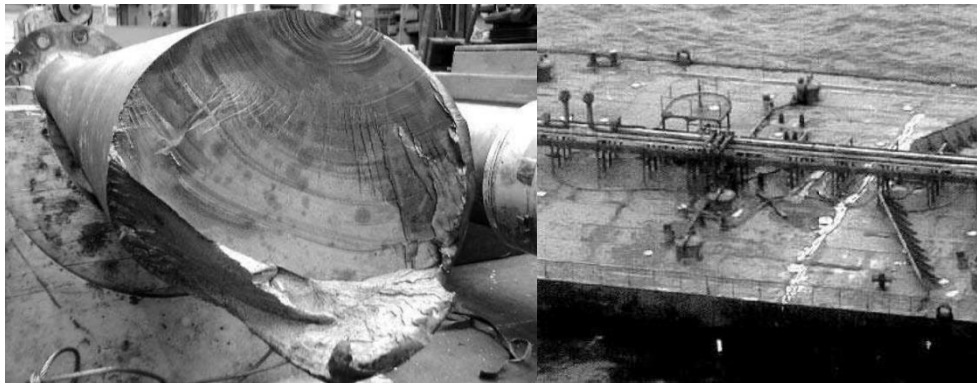


Figure 8 – Examples of Fatigue Failures: Propeller Shaft and Amidship of a Tanker (Lassen, T. and Récho, N. 2006)

Before deep research from microstructural point of view, concept of the S-N curves relies on the fact of quantifying lifetime according to applied constant cyclic stress on certain specimen. Normally, axial loads are considered for S-N curves. Some materials can present what is called endurance limit, stress value which below failure does not occur, independently from the number of cycles (Roylance 2001).

Many factors already mentioned before can vary the result on S-N curve, *e.g.* thickness, stress, material properties and weld details, among others.

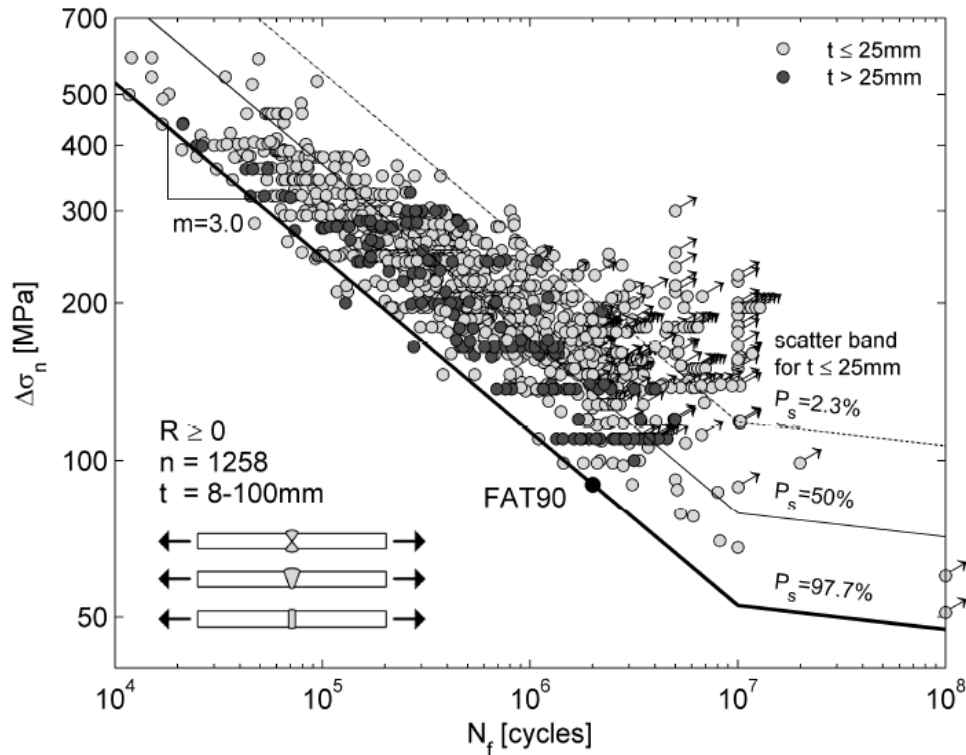


Figure 9 – Example of S-N Curve for Thickness Investigation on Butt Welded Joints (Pedersen, Andersen, J. G. and Ólafsson, Ó. M. 2012)

2.2 Fracture Mechanics

Manufactured materials usually contain microscopic cracks, which were initiated due to several reasons before its service utilization. For instance, defects or small surface/internal cracks are introduced during manufacturing and machining, also inclusions from fabrication, incomplete welds from assembly and impact with sharp hard materials during service, among others, which may nucleate and grow in the structure under fatigue loading.

Presence of such defects, especially in brittle materials, becomes unsafe when structures are under cyclic loading, being likewise dangerous in some ductile metals during conditions of low temperature environment and when subjected to a high rate of loading.

Fracture mechanics are well developed approaches that can predict when inherent flaws become critical, *i.e.* when a size is reached and, afterwards, the crack grows abruptly during short period causing failure of such structure at an operational stress under the material yield (Farahmand 2001).

Linear Elastic Fracture Mechanics (LEFM) provides estimation for the total number of cycles to failure that a material part with given initial crack can withstand subjected to a known load.

In summary, LEFM are based on already established flaws, like fatigue crack, and further study on the crack propagation, without considering the initiation phase described in Section 2 and included in Section 2.1. By non-destructive test (NDT), one can detect and obtain a roughly measurement of the flaw in real situation, which will be accomplish by the measurement device limitation.

It is important to review the modes in which a crack can extend. In summary, three modes can be verified by LEFM concepts as seen in Figure 10, where:

- Mode I is the crack opening mode. It is the most common mode, particularly in fatigue, because cracks tend to grow on the plane of maximum tensile stress. This type of failure represents most frequent type of separation that engineers design against and must be prevented (Farahmand 2001);
- Mode II is the in-plane shearing or sliding mode;
- Mode III is the tearing or anti-plane shear mode, associated with a pure shear condition of a round notched bar loaded in torsion; and
- Combinations of these crack extension modes can also occur.

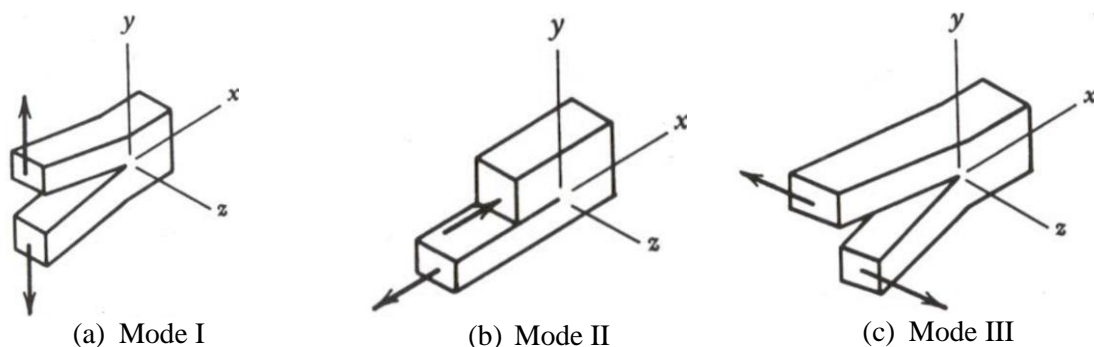


Figure 10 – Different Modes of Crack Extension (Hertzberg 1996)

Basically, a fracture mechanics assessment is similar in matter to S-N curves approach for design calculations. Nevertheless, the representation of fatigue resistance is performed by fatigue crack growth rate for a specific material, where well-known expression is verified regarding the fracture mechanics stress intensity factor parameter (ΔK). The stress intensity factor is directly connected to the applied stress range ($\Delta\sigma$) and the crack depth (a), such as follows:

$$\Delta K = Y \cdot \Delta\sigma \cdot \sqrt{\pi \cdot a} \quad (1)$$

being function of geometry and loading, represented by the term Y dimensionless factor that accounts for the crack geometry.

With this approach, the relationship between crack growth rate and ΔK will be according to a described law for a material type of any predetermined geometry. Previous cited law is approximated by linear relationship, normally referenced as *Paris-Erdogan* Law represented by the equation below:

$$\frac{da}{dN} = C \cdot (\Delta K)^n, \quad \text{for } \Delta K_{th} \leq \Delta K \leq \Delta K_c \quad (2)$$

Range of validity of Paris-Erdogan Law is also visualized in Eq. (2). Any value of ΔK below the threshold value of the material ΔK_{th} (or ΔK_0) will result in negligible crack growth.

On the other hand, if the resulting values reach K_{max} (or K_c), then the material will experience unstable crack growth and, consequently, it approaches the critical value for fracture as illustrated in Figure 11, where C is the *Paris-Erdogan* Constant.

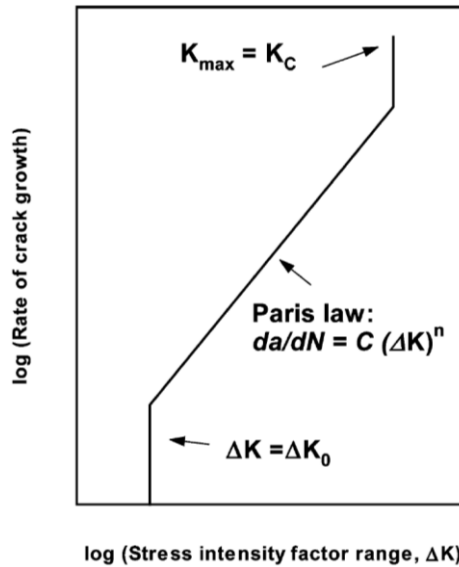


Figure 11 – Fracture Mechanics Fatigue Crack Growth Relationship (Maddox 2003)

Under constant load, the remaining fatigue life N under stress range ($\Delta\sigma$) of a piece is obtained by integrating Eq. (2) for a flaw size a_i and a critical fatigue crack size of a_f :

$$\int_{a_i}^{a_f} \frac{da}{\left(Y \cdot \Delta\sigma \cdot \sqrt{\pi \cdot a}\right)^n} = C \cdot N \quad (3)$$

For variable amplitude loading, it is necessary to perform the integration for each individual cycle (or block of equal stress cycles), such as exemplified below:

$$\int_{a_i}^{a_1} \frac{da}{\left(Y \cdot \Delta\sigma_1 \cdot \sqrt{\pi \cdot a}\right)^n} + \int_{a_1}^{a_2} \frac{da}{\left(Y \cdot \Delta\sigma_2 \cdot \sqrt{\pi \cdot a}\right)^n} + \dots + \int_{a_{j-1}}^{a_j} \frac{da}{\left(Y \cdot \Delta\sigma_j \cdot \sqrt{\pi \cdot a}\right)^n} = C \cdot N \quad (4)$$

Several experimental tests have been carried out for fatigue assessment of predetermined flaw, providing diversified parameters for *Paris-Erdogan* Law, C and n (or m). In addition,

brittle fracture works have been established and the stress intensity factor analysis has been explored. However, it is highly needed to research deeper the thickness and high tensile materials effects and the influence of flaws like lack of fusion in welded joints, among others. According to the model adopted, crack geometries, configuration and loading type, fracture mechanics stress intensity factor parameter can vary accordingly to the basic equation:

$$K = Y \cdot \sigma \sqrt{\pi \cdot a} = f\left(\frac{a}{W}\right) \cdot \sigma \sqrt{\pi \cdot a} = \alpha \cdot \sigma \sqrt{\pi \cdot a} \quad (5)$$

where W is the width dimension.

Several references have already provided some equations for different type of initial crack shape. In APPENDIX A, one can verify the formulation for semi-elliptical, corner quarter-elliptical surface model and elliptical embedded crack model, among others adopted herein (Fraunhofer 2008a, 2008b).

3. FRACTURE ASSESSMENT SIMULATION

In work performed by DNV GL (2015), several specimens were tested in order to verify the influence of a given lack of fusion on fatigue life in butt welded joints. Specimen numbers were already applied by hard stamping on the side of each specimen by HHI and delivered to Hamburg University of Technology (TUHH) to be tested. Fatigue tests were performed in TUHH with ten specimens fabricated of YP47 steel material with dimensions according to Figure 12. No information about composition of specimen was provided.

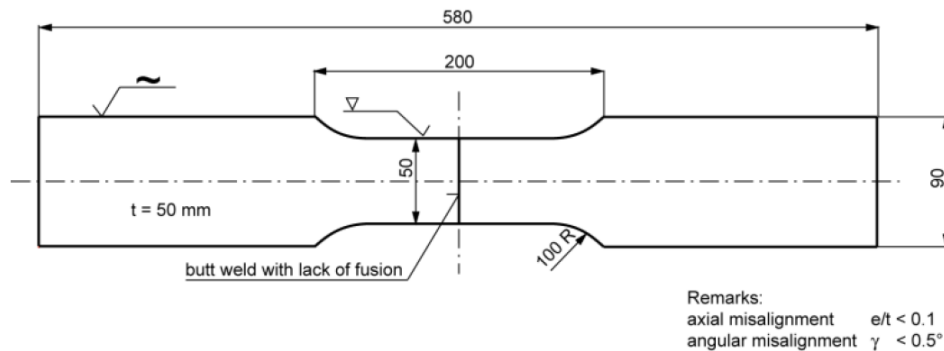


Figure 12 – Dimensions of Specimen (DNV GL 2015)

Initially, a visual inspection revealed that the top of the specimens was completely milled over all its breadth, even though the bottom was only ground locally, near 50% of the length. The bottom showed angular misalignment.

In addition to what was verified above, the specimens were completely measured to observe the weld shape and more precisely check any geometric imperfections, such as angular distortion and misalignment. All specimens showed notorious angular distortion, as seen in Figure 13, where the value range is between 0.4° and 1.2° .

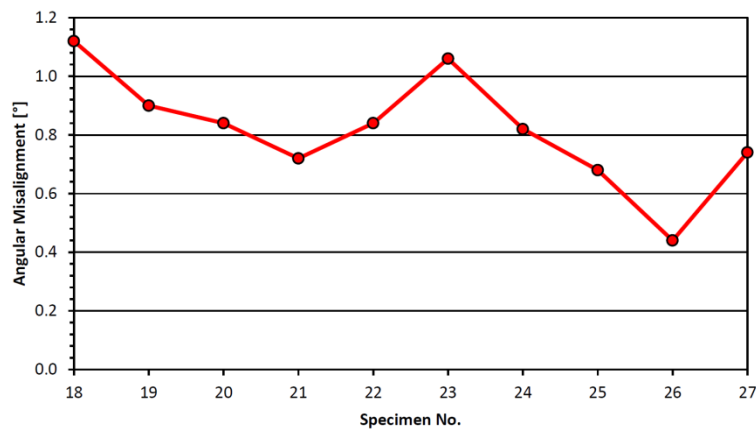


Figure 13 – Angular Distortion of Specimen (DNV GL 2015)

To reduce any extra stresses due to clamping on that configuration, the specimens were milled plane-parallel on the clamping region, according to Figure 14. Moreover, the ultrasonic test (UT) was carried out for localizing the internal defects on each specimen. Previously mentioned procedures were achieved in Germanischer Lloyd Prüflabor.

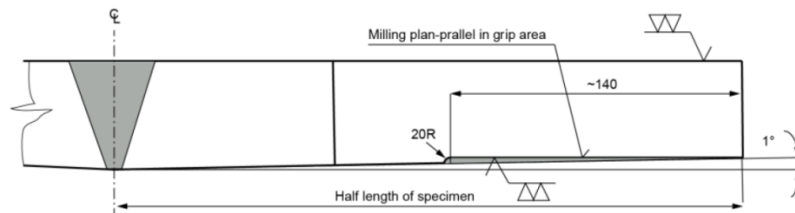


Figure 14 – Milling of the Clamping Area (DNV GL 2015)

Herein, to study the influence of a predetermined internal defect, it was taken into consideration the result obtained for Specimen 18 included in (DNV GL 2015). UT result with the location of the internal defect is seen in Figure 15, where the lines showed in red color represent the defect (1mm height size, approximately) for planes provided by thickness and width ($Y-Z$), as well as thickness and length ($X-Z$) near the region of weld. The adopted coordinates are as observed in Figure 16.

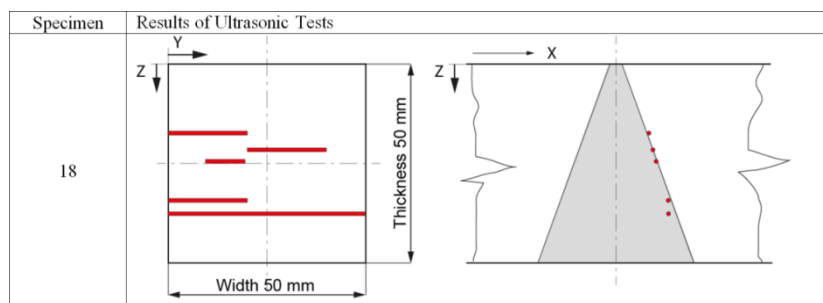


Figure 15 – Location of Internal Defect for Specimen 18 by UT (DNV GL 2015)

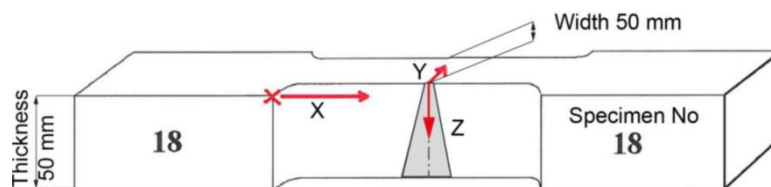


Figure 16 – Coordinate System for UT Indications of Specimens (DNV GL 2015)

Strain gauges were applied in all specimens, on top and bottom, including also at the middle of welded nugget to follow the results of the axial cyclic test. One should be able to verify cracks by monitoring strain gauges signals.

After testing, comparison between results from crack surface of specimen 18 and UT is established. As shown in Figure 17, the actual dimensions of the internal defect could be estimated. It has around 30mm high (width) and 25mm wide (thickness). As observed, it was not possible to do a perfect not welded region, since it is quite difficult to accomplish this task. Thus, most of the time, the defects will appear as line shape to UT measurement.

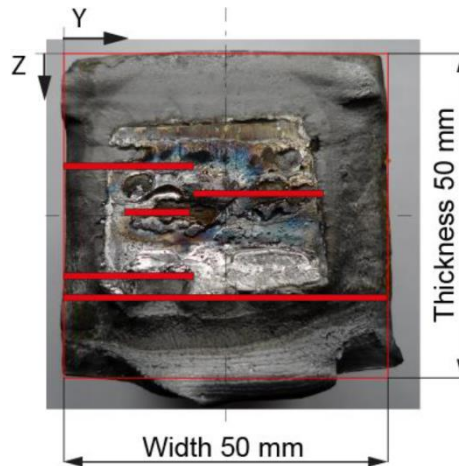


Figure 17 – Crack Surface Result for Specimen 18 after Testing (DNV GL 2015)

Correlated to fracture mechanics, it is possible to state that the crack grew upwards (towards weld root) and on the bottom side (final pass) the crack growth was slightly slower. The final rupture region shows large deformations with single beach marks in the final phase. Some welded connections that were supposed to be not welded are verified on this region.

From Figure 18, one can verify that, in between 25000 and 30000 numbers of cycles, the initial crack as part of the lack of fusion inside the specimen reached the surface, measured by Strain Gauge 1. On the other hand, the final fracture reached around 45000 numbers of cycles.

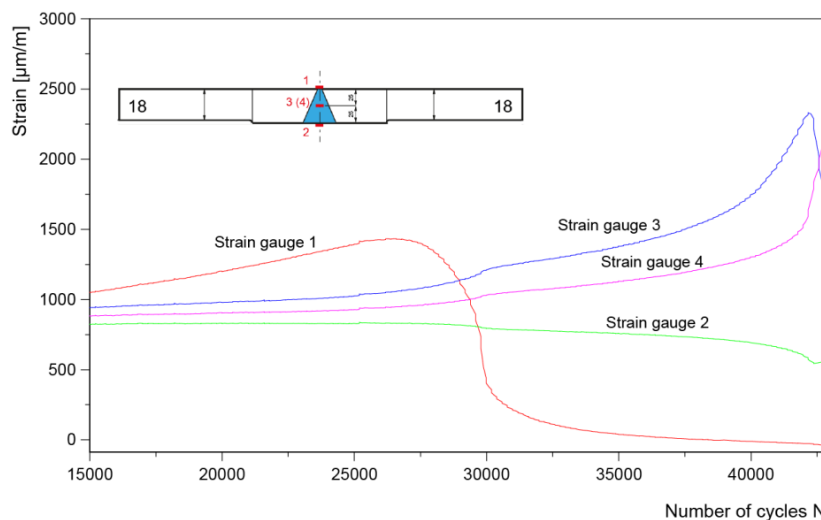


Figure 18 – Strain Gauges Position and Measurement for Spec. 18 (DNV GL 2015)

Concerning the implemented tests, Table 2 and Table 3 provide the results for all specimens taken from the S-N curves provided by Figure 19. The evaluation was done adopting a fixed slope $m = 3.0$ of the S-N curves. Apparently by virtue of the notable difference on the lack of fusion within each specimen, a large scatter was verified.

An outstanding lifetime was reached by Specimen No. 23. Test load was increased three times until the specimen finally failed at a stress range of $\Delta\sigma = 170 \text{ N/mm}^2$, nevertheless the result lies still on the right side of the scatter band.

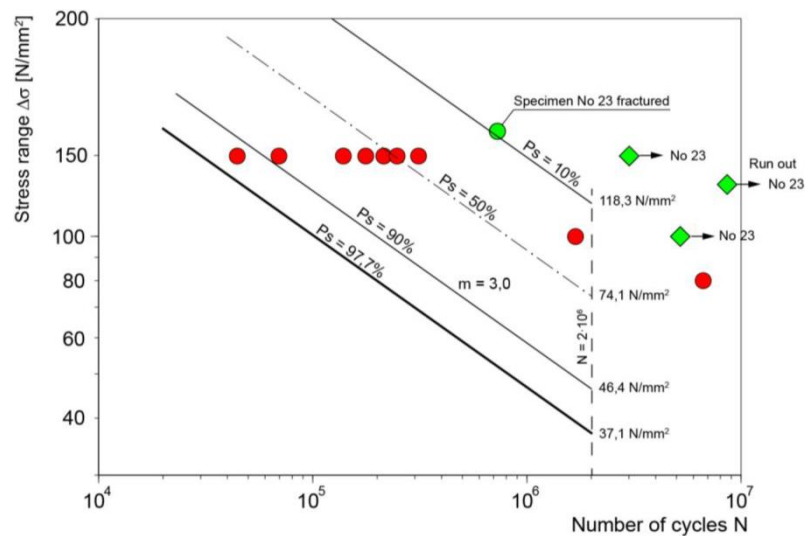


Figure 19 – Test Results S-N Curves (DNV GL 2015)

Table 2 – Test Results for All Specimens (Except Specimen 23)

Result	Stress Range, $\Delta\sigma$ (MPa)	Number of Cycles, N
1	150	$4.39 \cdot 10^4$
2	150	$6.94 \cdot 10^4$
3	150	$1.40 \cdot 10^5$
4	150	$1.78 \cdot 10^5$
5	150	$2.13 \cdot 10^5$
6	150	$2.48 \cdot 10^5$
7	150	$3.16 \cdot 10^5$
8	100	$1.70 \cdot 10^6$
9	80	$6.44 \cdot 10^6$

Table 3 – Test Results for Specimen (Run Out)

Result	Stress Range, $\Delta\sigma$ (MPa)	Number of Cycles, N
10	100	$5.21 \cdot 10^6$
11	130	$8.59 \cdot 10^6$
12	150	$3.16 \cdot 10^6$
13	170	$7.17 \cdot 10^5$

3.1 Simulation for Specimen 18

3.1.1 Simulation Input Data for Fraunhofer IWM VERB

Plate model was chosen under cyclic loading based on axial load of Stress Ratio (R) obtained from Fricke, W. and Paetzold, H. (2012), since there is no information in DNV GL (2015):

$$R = \frac{\sigma_{\min}}{\sigma_{\max}} = 0 \quad (6)$$

Thus, the loading values were defined by membrane stresses and kept constant during crack propagation, such as maximum and minimum stresses, respectively as:

$$\sigma_{a_{\max}} = 150 \text{ MPa} \quad (7)$$

$$\sigma_{a_{\min}} = 0 \quad (8)$$

The input data for the software *Fraunhofer IWM VERB*⁶ (Fraunhofer 2008b, 2008a) were according to Table 4 and Table 5, where Table 4 presents the common values of the specimen geometry (thickness, t and width, $2W$); internal defect dimensions (height, y_{def} and width, x_{def}); and crack centre position (sum of crack depth, a and ligament, d).

Table 4 – Common Parameters of Specimen 18

Tests	Model	t (mm)	$2W$ (mm)	y_{def} (mm)	x_{def} (mm)	$a+d$ (mm)	m (-)
I, II and III	Ellipse Embedded	50.00	50.00	30.00	25.00	25.00	3.00

Table 5 – Parameters for Simulation of Specimen 18 on *Fraunhofer IWM VERB*

Tests	Reference	C (-)	ΔK_{th} (MPa)	K_c (mm)	$2c$ (mm)	$2a$ (mm)	R_A (-)
I	IIW 2008 (Hobbacher 2008)	$1.65 \cdot 10^{-8}$	5.40	1000	30.00	25.00	0.79
I	Series A (Doerk, Shin, S.-B.)	$4.78 \cdot 10^{-9}$	8.22	1000	30.00	25.00	0.79
II	IIW 2008 (Hobbacher 2008)	$1.65 \cdot 10^{-8}$	5.40	1000	39.05	39.05	1.60
II	Series A (Doerk, Shin, S.-B.)	$4.78 \cdot 10^{-9}$	8.22	1000	39.05	39.05	1.60
III	IIW 2008 (Hobbacher 2008)	$1.65 \cdot 10^{-8}$	5.40	1000	31.83	30.00	1.00
III	Series A (Doerk, Shin, S.-B.)	$4.78 \cdot 10^{-9}$	8.22	1000	31.38	30.00	1.00

All modeling was established according to British Standard Institute (1999) and with aid of Bezensek et al. (2011). Table 5 provides the assumption for modeling the internal defect and parameters from references that were used for the *Paris-Erdogan* Law, represented by Eq. (9) and working on the domain of Eq. (10), defining constant C , threshold ΔK_{th} and

⁶ <http://www.en.iwm.fraunhofer.de/core-competencies/technical-equipment/iwm-verb/>

upper bound value of critical stress intensity factor at cyclic loading K_c , including area ratio R_A provided by Eq. (11) and initial crack depth a_0 and initial crack length c_0 (or $2c_0$). Series A parameters were obtained experimentally from as welded specimens.

$$\frac{da}{dN} = C \cdot \Delta K^m \quad (9)$$

$$\Delta K_{th} \leq \Delta K \leq (1-R)\Delta K_c \quad (10)$$

$$R_A = A_{model} / A_{defect} \quad (11)$$

Critical value of stress intensity factor at cyclic loading K_c is taken as $1000 \text{ MPa}\cdot\sqrt{\text{m}}$, considering a high value in order to avoid the simulation to reach the region where there is an abrupt increase on the crack propagation rate, *i.e.* unstable crack propagation.

A rectangular shape internal defect is assumed to be in the centre of the cross section of the specimen. Test I is performed considering that the internal defect is modeled by an ellipse embedded with main dimensions equal to the defect dimensions, located in centre of both the specimen and the defect. Test II is similar to Test I, however with main dimensions equal to a circle which circumscribes the defect. Finally, Test III is also similar to Test I, nevertheless it is implemented considering that the area ratio (R_A) is one, *i.e.* the crack model has area equal to the area of the internal defect. A summary including all dimensions is verified in Table 5 and sketch is provided by Figure 20.

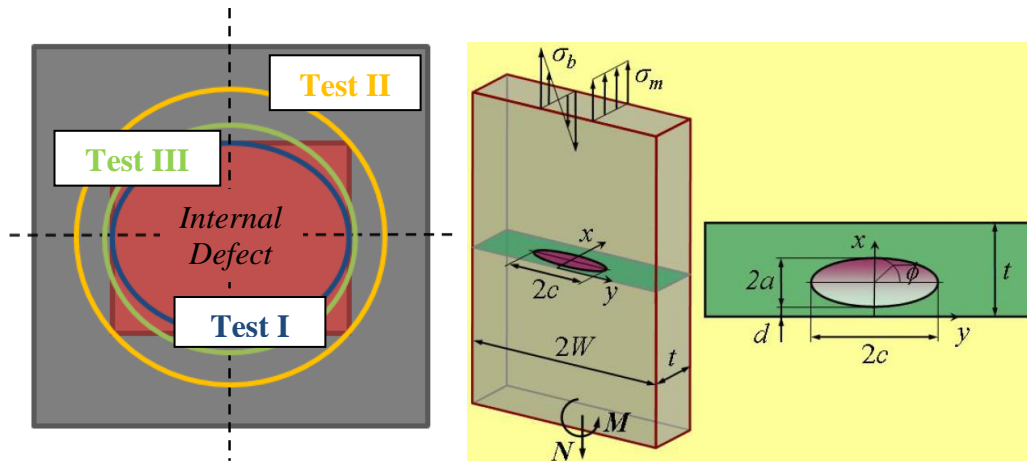


Figure 20 – Sketch of Geometries for Each Test and Crack Model from *Fraunhofer IWM Verb* (Fraunhofer 2008a, 2008b)

3.1.2 Results for Pure Axial Load with Constant Stress

As observed in Figure 21, the crack propagation for an elliptical model is provided for half of specimen geometry of each test. Rectangular shape in red color denotes the internal defect.

Blue, orange or green colors represent the initial crack model and the solid black lines are the crack propagation paths.

It is noted that the crack length did not reach the surface for all cases, thus an additional number of cycles until final failure can be achieved. However, that amount is too small compared to the number of cycles to reach the surface, therefore it is neglected.

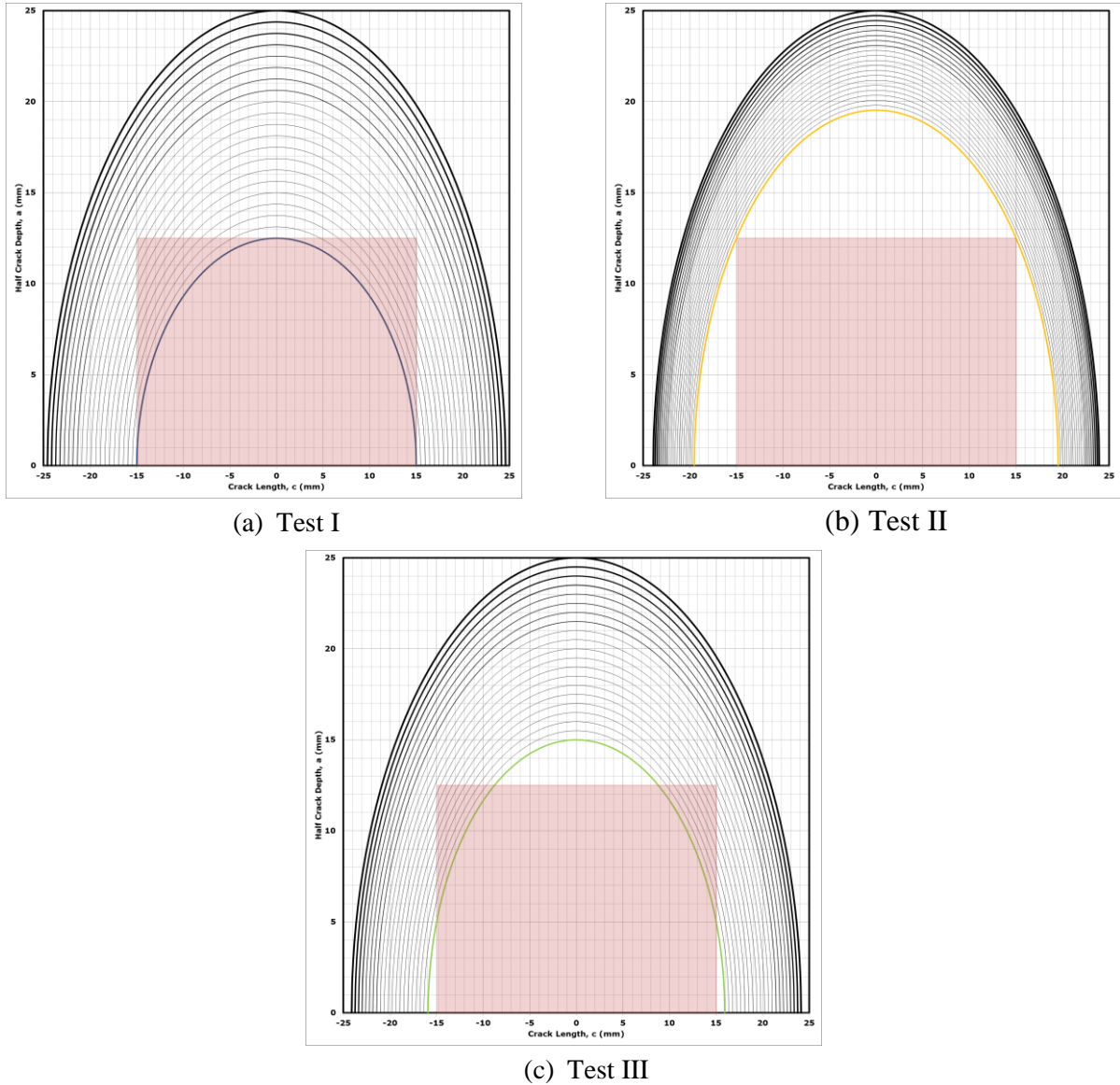


Figure 21 – Specimen 18 Crack Propagation for Each Model in Axial Load

Results for the simulations can be verified in

Figure 22, where the approach considering IIW-2008 is strongly more conservative than the Series A for all models. The model of an ellipse with main dimensions equal to the ones of the lack of fusion provided by the Test I Series A has the biggest number of cycles until the

crack reaches the surface, around 60873, and a relative error of around -39% when compared to the experimental result. Relative error is calculated as following:

$$\varepsilon_{relative} = \frac{Experimental - Simulation}{Experimental} \quad (12)$$

Another poor model would be the circle surrounding the lack of fusion defect represented by Test II - IIW 2008 and Test II - Series A, with relative error respectively of around 96% and 84%. Also, the model with same area of the lack of fusion as in Test III - IIW 2008 presents a relative error of 76%.

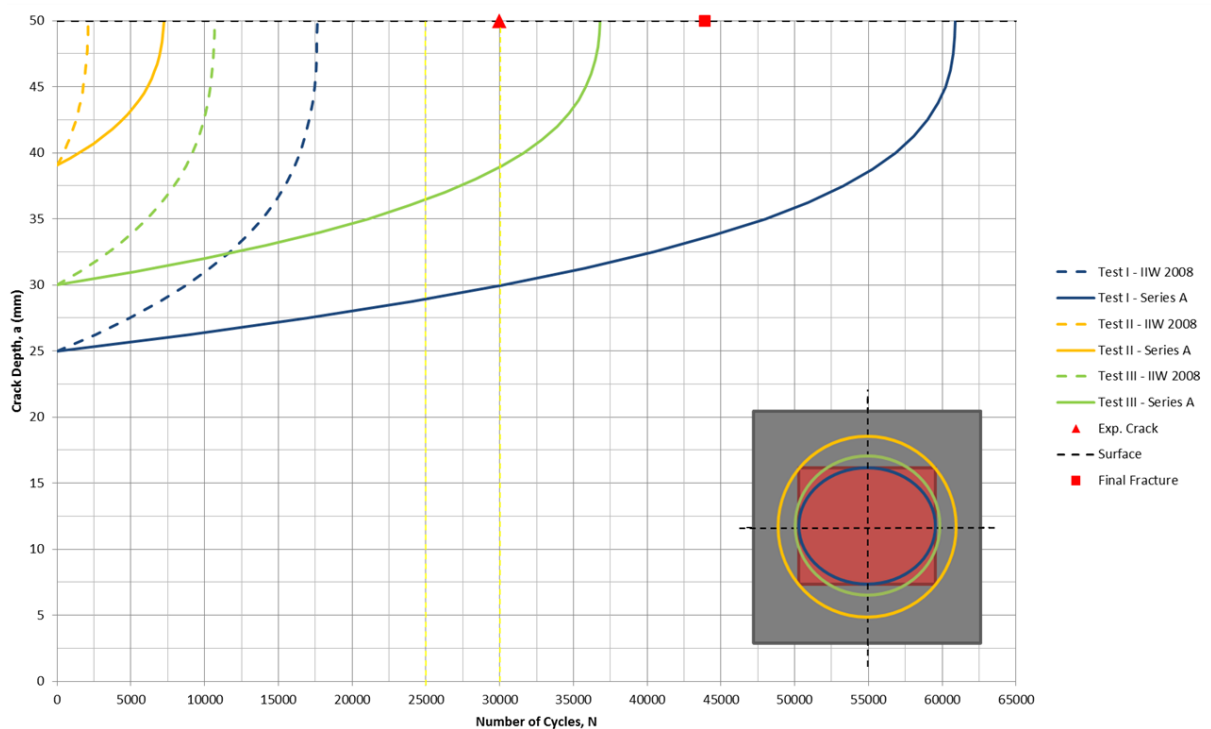


Figure 22 – Simulation Results for Crack Propagation of Specimen 18 for Pure Axial Load

The model represented by Test III - Series A (same area) provides closer result and presents itself with a relative error of near 17%. Test I - IIW 2008 would be considered the other side of the range with a number of cycles smaller than the experimental result, with a relative error of 60%.

Therefore, a good representation of Specimen 18 would be a combination between those two models, one with same area with Series A parameters and other with an centered ellipse with main dimensions of the rectangular shaped lack of fusion with approach of IIW 2008. All results and comparison are summarized in Table 6.

It has to be taken into account that fracture mechanics does not comply the crack initiation phase, thus the Test III – Series A can practically represent the crack propagation phase of the experimental test.

Table 6 – Comparison between Experimental and Simulation Results for Specimen 18

Test	Reference	No. Cycles Experimental	No. Cycles Simulation	Absolute Error	Relative Error
I	IIW 2008	43900	17635	26265	60%
I	Series A	43900	60873	-16973	-39%
II	IIW 2008	43900	2101	41799	96%
II	Series A	43900	7253	36647	84%
III	IIW 2008	43900	10665	33235	76%
III	Series A	43900	36815	7085	17%

3.1.3 Results for Pure Bending Load with Constant Stress

For further analysis, one will take into consideration only the Series A properties for the material. In order to simulate the case of pure bending load, the bending stresses are considered with same magnitude of the ones applied for pure axial load observed in Eq. (3), for instance:

$$\sigma_{b_{\max}} = \sigma_{a_{\max}} = 150MPa \quad (13)$$

$$\sigma_{b_{\max}} = -\sigma_{a_{\max}} = -150MPa \quad (14)$$

which has been kept constant, during first crack propagation analysis for bending.

Adopting the same models established in Subsection 3.1.1 and considering the same stress range as stated above, the results for pure bending compared to pure axial load can be verified in Figure 23.

As noticed, pure bending presents a less effect on fatigue life than pure axial load. Depending on the model, the difference between the numbers of cycles to the crack reach the surface can be expressive as summarized on Table 7, where the highest difference is for Test I of approximately $2 \cdot 10^5$ number of cycles. The parameter namely Degree of Bending (DoB, Ω) is established according to the Eq. (15) below (Maddox 2015):

$$\Omega = \frac{\sigma_b}{\sigma_t} = \frac{\sigma_b}{(\sigma_b + \sigma_a)} \quad (15)$$

relating bending stress over total stress (bending and axial stresses).

Table 7 – Results for Pure Axial and Bending Loads with Same Stress Range

Load	Number of Cycles, N			DoB, Ω
	Test I	Test II	Test III	
Pure Axial	60873	7253	36815	0
Pure Bending	254645	13522	116248	1
Absolute Difference	193772	6269	79433	
N_b/N_a	4.18	1.86	3.16	

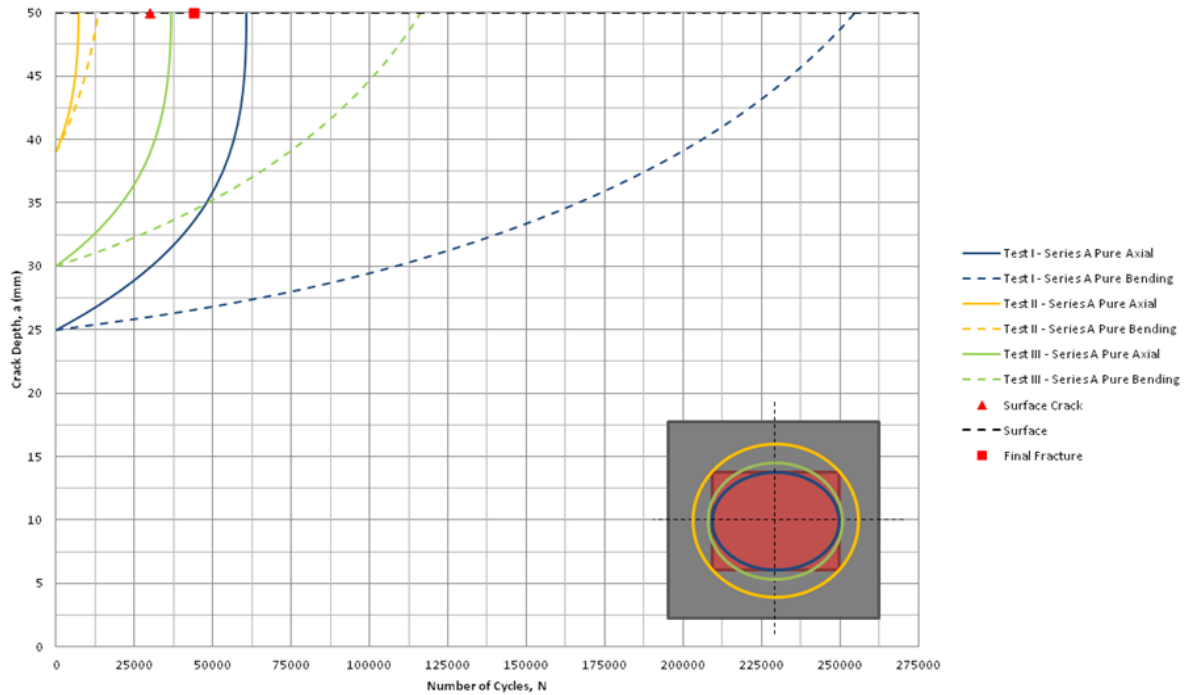


Figure 23 – Crack Propagation for Pure Axial and Bending Loads with Same Stress Range

3.1.4 Results for Pure Bending Load for Constant Number of Cycles

Other comparison that can be made is related to a constant number of cycles, in which it is taken into account the number of cycles for pure axial load of each model, keeping this value constant and determining the stress that should be applied for pure bending in order to the crack reach the surface in the same number of cycles over the adopted models.

As verified in Figure 24, the crack propagation for an elliptical model under bending load is provided for half of specimen geometry of each test, in which the crack only propagates over half crack depth (a) direction, since the stress is acting only on that direction.

For each model, the number of cycles for pure axial load simulation was already been provided by Table 5. The result for the comparison between pure axial and bending loads is

verified in Figure 25, where the stresses in pure bending necessary to obtain the same number of cycles of pure axial are described in Table 8.

Table 8 – Results for Pure Axial and Bending Loads with Same Number of Cycles for Each Model

Load	Stress (MPa)		
	Test I	Test II	Test III
Pure Axial	150.00	150.00	150.00
Pure Bending	241.68	184.65	220.06
$k_b = \sigma_b/\sigma_a$	1.61	1.23	1.47

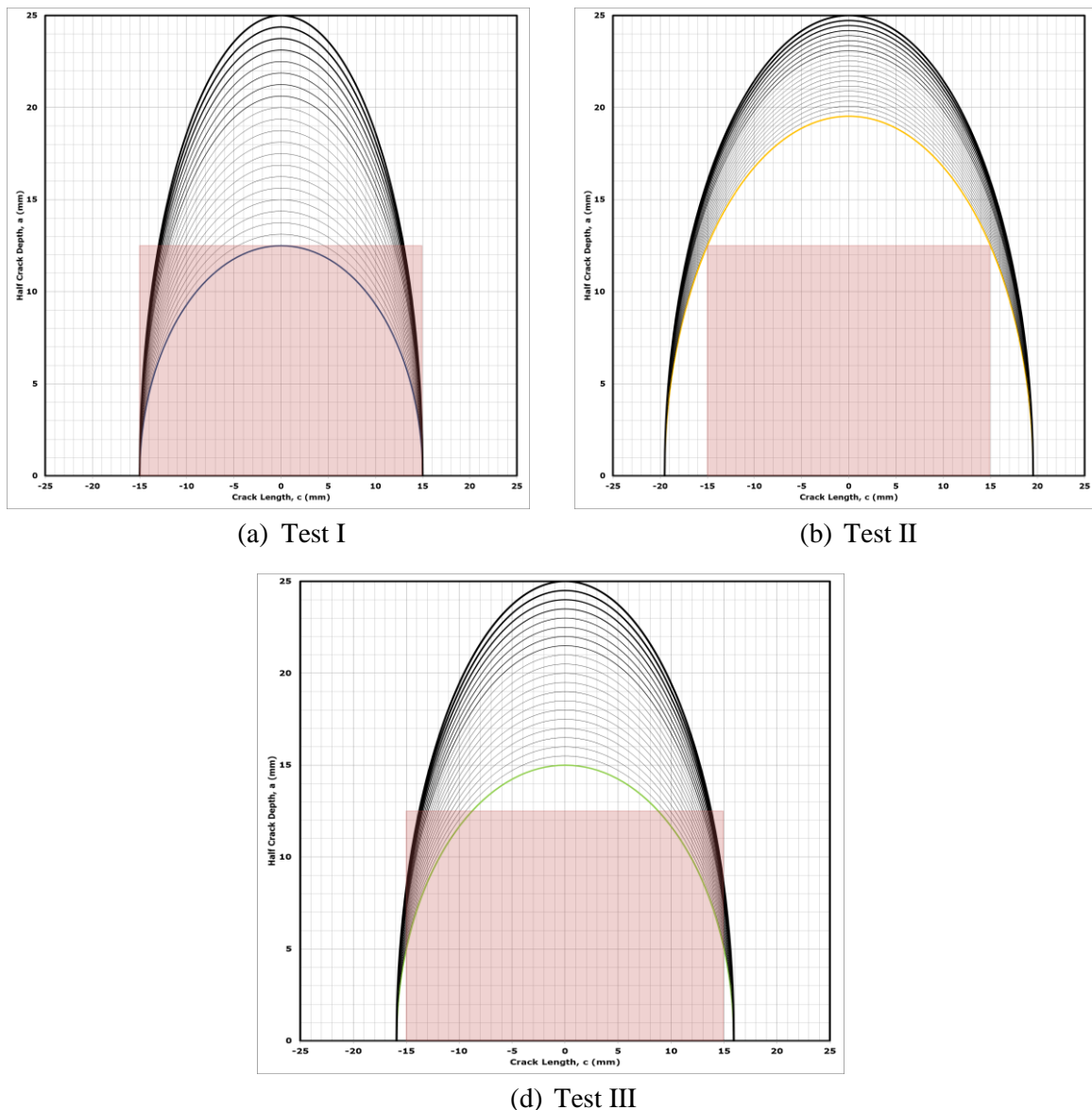


Figure 24 – Crack Propagation in Specimen 18 for each Model under Bending Load

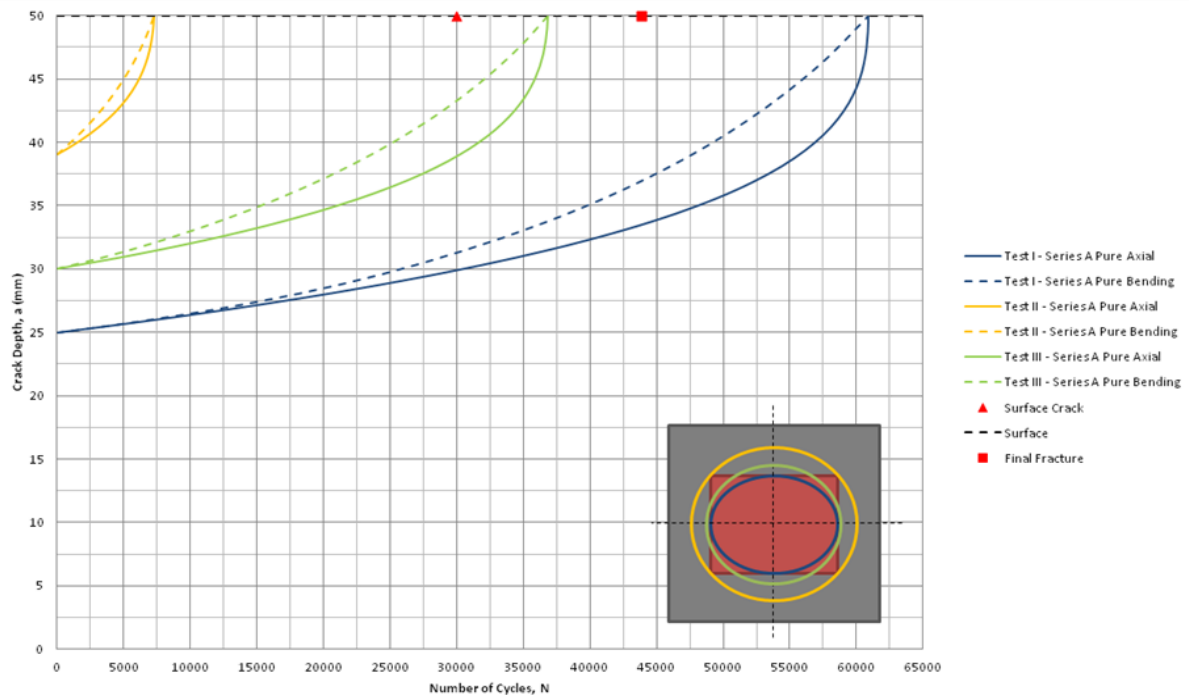


Figure 25 – Crack Propagation for Bending with Same Number of Cycles of Axial

3.1.4.1 Comparison to Maddox

In few words, the idea behind the work performed by Maddox (2015) is to provide an expression for the fatigue strength enhancement with introduction of correction factor due to bending load, improving what was described in British Standard Institute (1995) by introducing the results in published document British Standard Institute (2014).

According to work done by Maddox (2015), the equation for fatigue strength enhancement factor from BS7608:1993 (British Standard Institute 1995) is given as follows:

$$k_b = \frac{\sigma_b}{\sigma_t} = \left[1 + \left\{ \frac{0.7}{t^{0.2}} + 0.5 \cdot \log \frac{L}{t} \right\} \cdot \Omega^{1.4} \right]^x \quad (16)$$

for cruciform joints, considering $x = 1$ for a decreasing stress range gradient through the thickness or $x = -1$ for an increasing stress range gradient and L is attachment size, with a value of weld detail L/t equals to 2.

For different thickness values, one can establish the results of Eq. (16) as shown in Figure 26 for $x = 1$, including values calculated by fracture mechanics (Maddox 2015). Since just a limited database is provided in British Standard Institute (1999), Maddox considers a more convincing basis for validation.

As conclusion for a butt welded joint included in his document, fatigue strength enhancement factor k_b is equal to 1.34 provided by Eq. (17) and 1.20 by experimental result for $\Omega = 1$.

$$k_b = 1 + \left\{ \frac{0.7}{t^{0.2}} + 0.5 \cdot \log \frac{L}{t} \right\} \quad (17)$$

Finally, as a general formulation determined at the end of his research, Eq. (18) applied to Specimen 18 gives k_b equals to 1.18 also for Degree of Bending $\Omega = 1$ and thickness t equals to 50mm. For Specimen 18 geometries, Eq. (16) is also calculated.

$$k_{tb} = \left(\frac{25}{t_{eff}} \right)^n \cdot [1 + 0.18\Omega^{1.4}] \quad (18)$$

From the following consideration from Maddox (2015):

- n can assume the values of 0.25 or 0.20;
- t_{eff} is maximum value of $L/2$ or 25mm if $L/t \leq 2$; or
- t_{eff} is equal to t if $L/t > 2$ or if it is not known or relevant.

observing the weld characteristic in Figure 27, one can calculate:

$$L = 38.9mm \quad (19)$$

$$\frac{L}{t} = 0.78 \leq 2 \quad (20)$$

$$\frac{L}{2} = 19.45mm \quad (21)$$

$$t_{eff} = 25mm \quad (22)$$

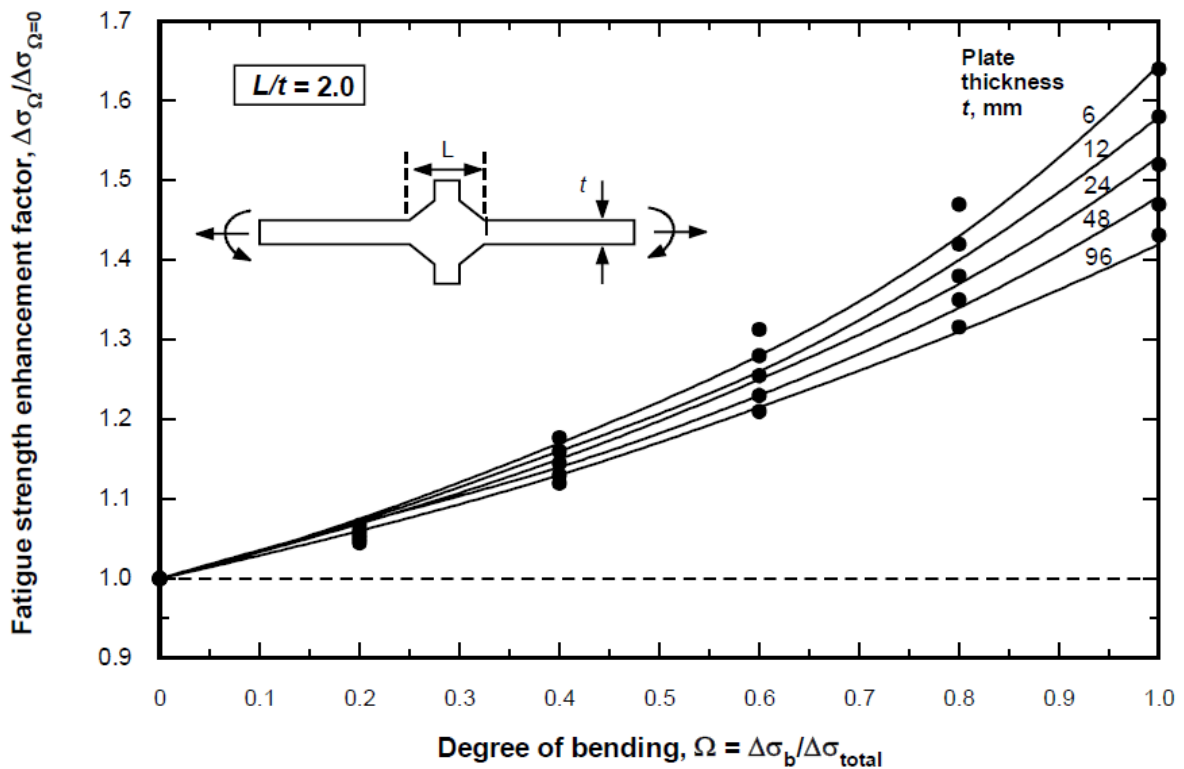


Figure 26 – Effect of Degree of Bending on Relative Fatigue Strength of Joints Failing from Weld Toe as Determined Using Fracture Mechanics (Maddox 2015)

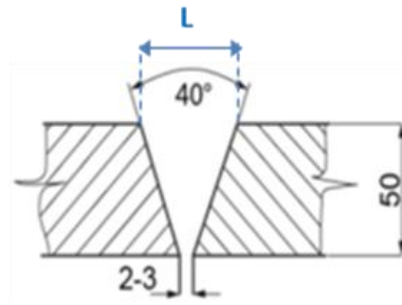


Figure 27 – Weld Geometry taken from Fricke, W. and Paetold, H. (2012)

All above mentioned results are established in Figure 28, including the result for Test III Series A with k_b equals to 1.47 calculated and already provided in Table 8 from Subsection 3.1.4.

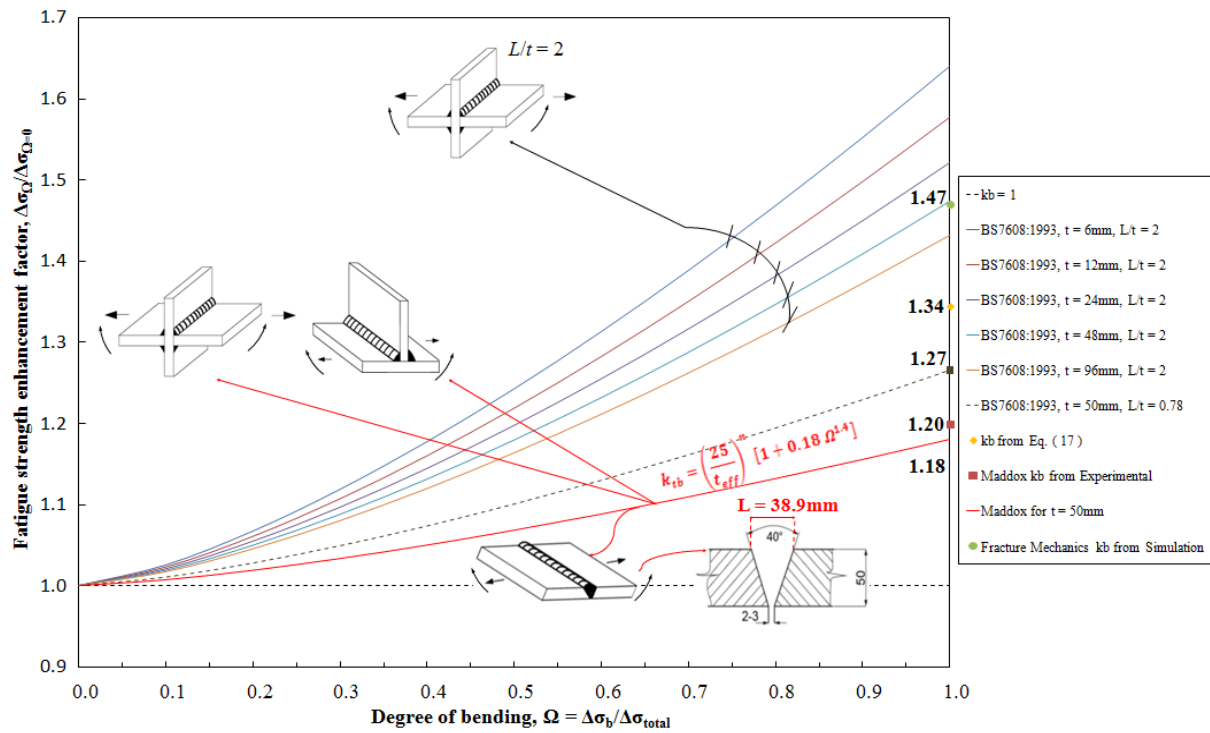


Figure 28 – Comparison Result from Fracture Mechanics Simulation with Available Literature

In Figure 28, different results are verified and future works are necessary to better understand the fatigue enhancement due to bending load for internal flaws, since the work made by Maddox and the available literature included in his work are slightly conservative and mainly based on fails usually occurring by fatigue crack growth from weld toe.

4. THERMAL CUT EDGES ANALYSIS

For thermal cut edges (TCE) evaluation, the main proposal is to verify the thickness effect and the consequences of different types of edge treatment for a certain thermal cutting procedure under axial and bending loads. Three different thickness dimensions are considered and six varied edge treatments are adopted, as revealed by Figure 29, where C denotes the depth of chamfering, R the radius of grinding and the value on the right side means the size of the edge treatment in millimeters.

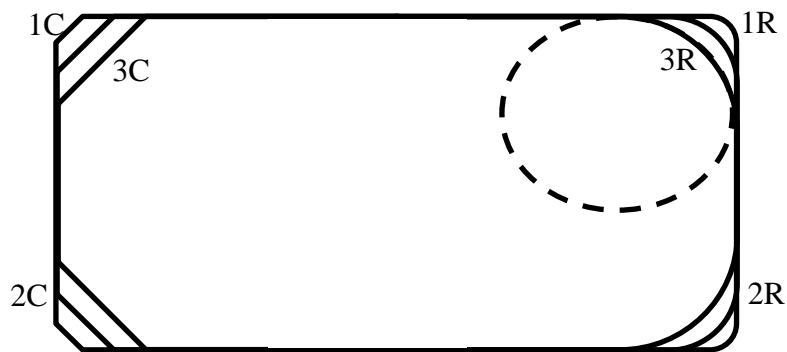


Figure 29 – Edge Treatment Identification

Geometry of the specimen that was used in experimental tests before (Selle et al. 2011) and for the simulation herein performed is observed in Figure 30.

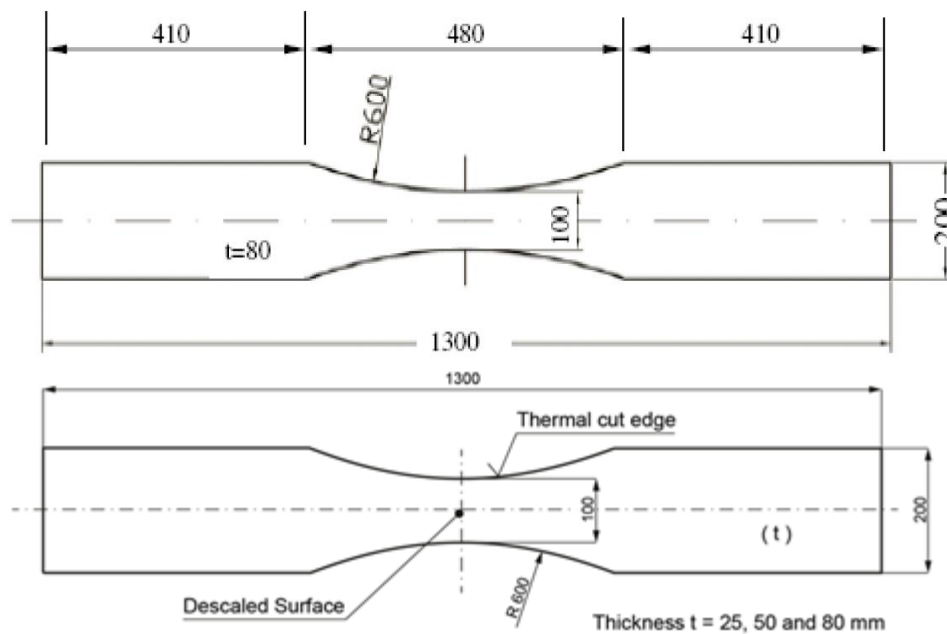


Figure 30 – Thermal Cut Edge Specimen Geometry

Different techniques are well suitable to improve fatigue strength of welded joints (Haagensen, P. J. and Maddox, S. J. 2013). For improvements of thermal cut edge, among condition adopted in the industry one can cite chamfered and grinding in order to reduce the notch effect and improve the fatigue life, where both are often chosen for hatch corner utilization in containerships (BV Korea Marine 2014).

Parameters of Table 9 are adopted for the simulation, which were taken from high tensile steel GL-E40 properties obtained from Selle et al. (2011). The simulation complied are performed for both axial and bending loads.

Table 9 – Material Properties for FEM Investigation of Thermal Cut Edge Specimen

Parameter	Value
Yield Point	408 MPa
Tensile Strength	512 MPa
Poisson Coefficient	0.30
Young Modulus	204 GPa

4.1 Analytical Result

Simple nominal formulations have already been established (Beer, Johnston Jr., E. R., DeWolf, J. T. and Mazurek, D. F. 2014), such as:

$$\sigma_t = F/A \quad (23)$$

$$A = W \cdot t \quad (24)$$

for pure tensile load, where F is force, A is area, W is width and t is the thickness of specimen.

For pure bending, the following equations can be applied:

$$\sigma_b = M \cdot y / I \quad (25)$$

$$I = t \cdot W^3 / 12 \quad (26)$$

where M is the bending moment, y is the distance from the neutral line and I is the second moment of inertia. It will be considered $\sigma_t = 50$ MPa as nominal stress for the boundary on tensile test (in *Ansys* pressure of 50 MPa) and the bending moment M will be as stated in Table 10 for bending test, in this way it is possible to obtain nominal stress values of 100 MPa in the center region of the specimen.

Table 10 – Nominal Stress for Tensile and Bending

Thickness (mm)	σ_{t1} (MPa)	σ_{t2} (MPa)	M_3 (N.mm)	M_4 (N.mm)	σ_{b3} (MPa)	σ_{b4} (MPa)
80	50	100	$6.7 \cdot 10^6$	$6.7 \cdot 10^6$	25	100
50	50	100	$4.2 \cdot 10^6$	$4.2 \cdot 10^6$	25	100
25	50	100	$2.1 \cdot 10^6$	$2.1 \cdot 10^6$	25	100

It is easy then to determine the nominal values for the specimen over tensile and bending loads, according to Table 10, where lines 1 and 2 including points 3 and 4, are identified in Figure 31.

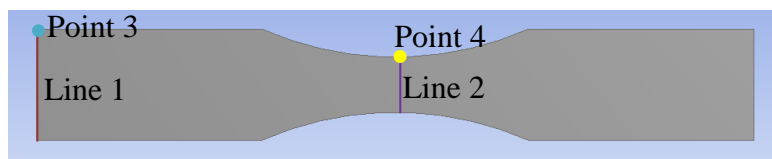


Figure 31 – Identification of Lines 1-2 and Points 3-4 for Stress Values

Analytical results can be achieved using charts provided by Pilkey (1997). From Figure 32, it is obtained the value of the Stress Concentration Factor (SCF) around:

$$K_t = \frac{\sigma_{\max}}{\sigma_n} \approx 1.05 \quad (27)$$

for axial load of a piece with a smooth radius. Thus, the maximum stress under axial load due to the notch verified on the piece is:

$$\sigma_{a_{\max}} = K_t \cdot \sigma_n = 1.05 \cdot 100 = 105MPa \quad (28)$$

Figure 33 provides the value of the stress concentration factor around:

$$K_t = \frac{\sigma_{\max}}{\sigma_n} \approx 1.03 \quad (29)$$

for bending load of a piece with opposite shallow U-shaped notches. Hence, the maximum stress under bending load is:

$$\sigma_{a_{\max}} = K_t \cdot \sigma_n = 1.03 \cdot 100 = 103MPa \quad (30)$$

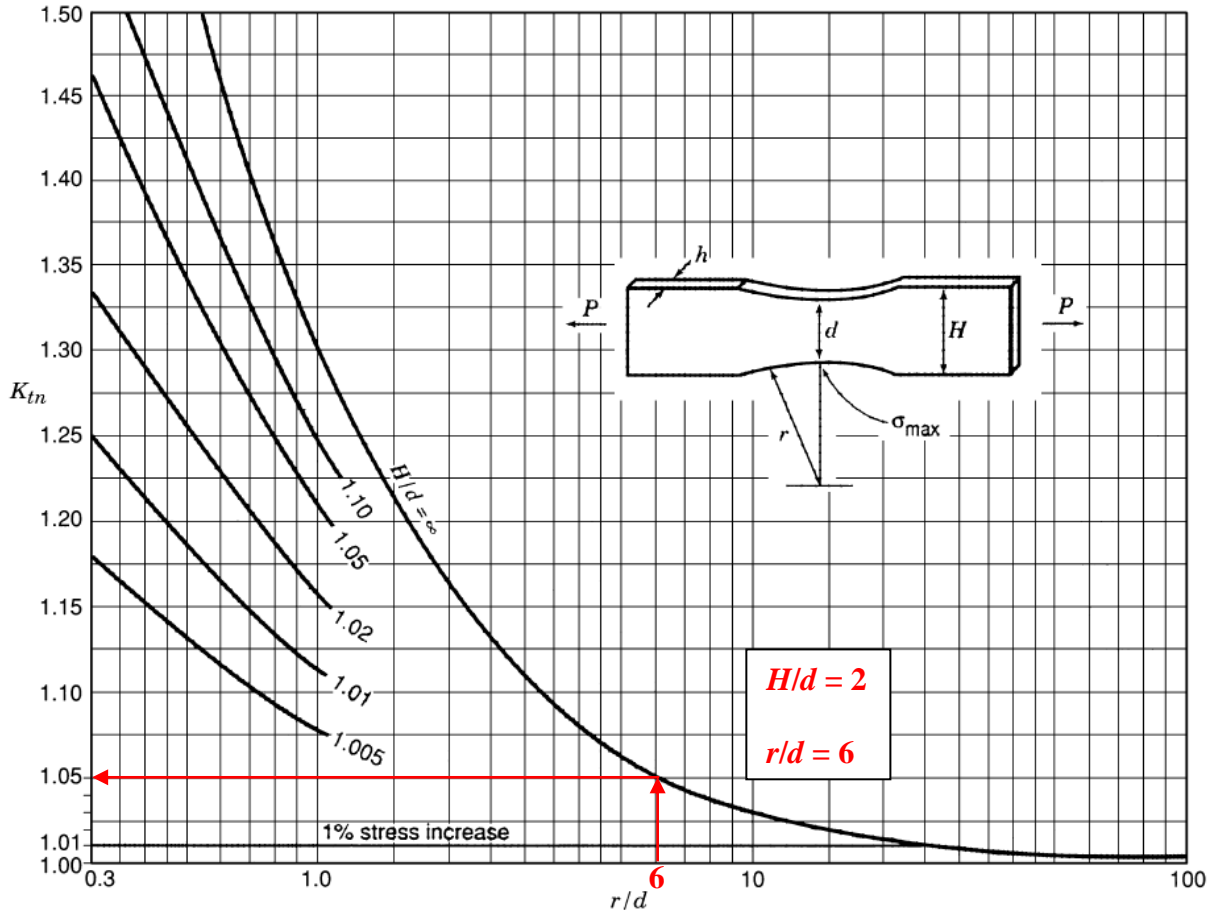


Figure 32 – SCFs K_m for a Flat Test Specimen with Opposite Shallow U-Shaped Notches in Tension

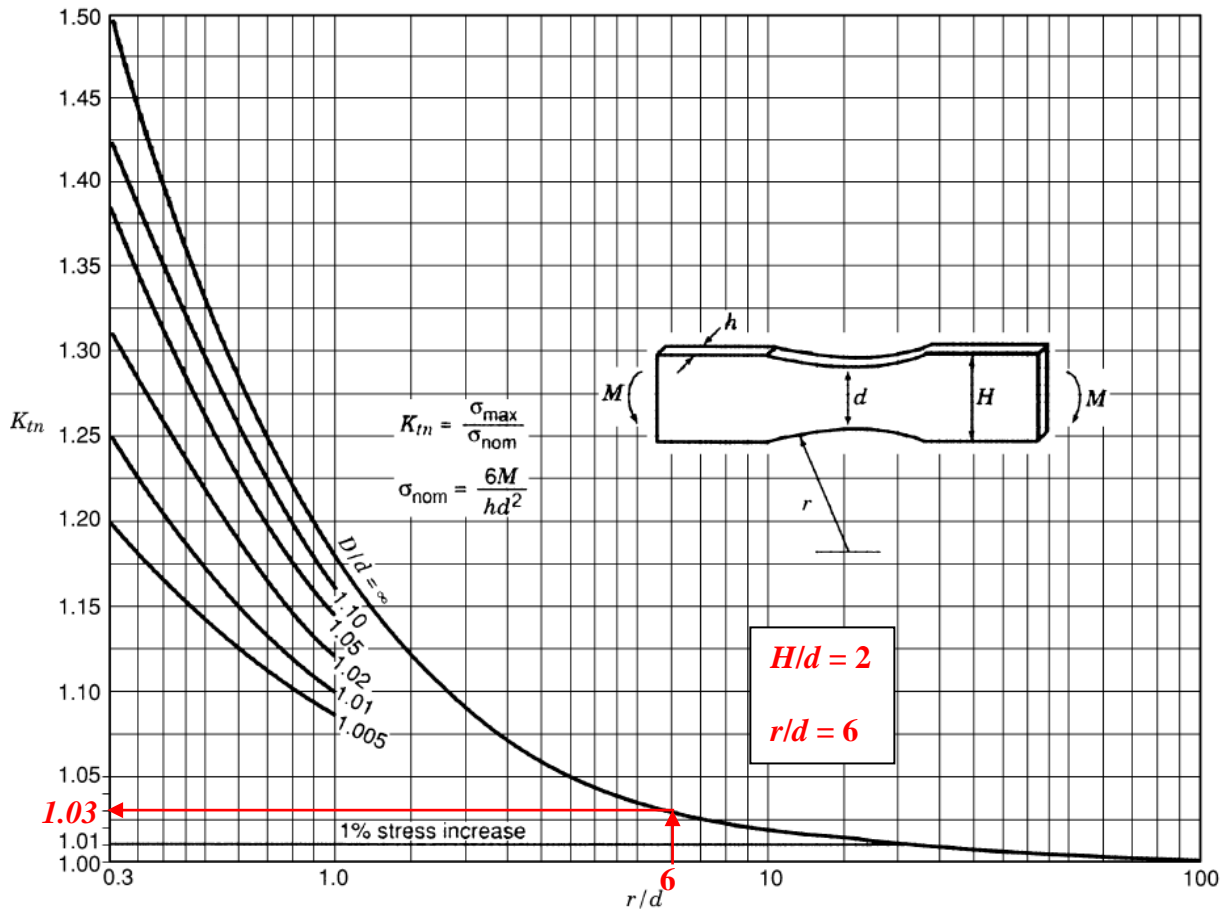


Figure 33 – SCFs K_m for Bending of a Flat beam with Opposite Shallow U Notches

4.2 Loads and Boundary Conditions for 2D and 3D Analyses

4.2.1 Symmetry Evaluation of Specimen

A complete model with an extremely fine mesh simulation is performed to confirm that adopting the boundary symmetry will result in reliable values and it is totally allowed to be considered, as observed in Figure 34 and Figure 35 (a) and (c) for 2D axial and bending loads, as well as in Figure 34 and Figure 35 (b) and (d) for 3D axial and bending loads, respectively. For the 2D complete model, 170261 nodes and 55312 elements were used, including a refinement level 3 on the edges and mid-section. For the 3D complete model, 8060770 nodes and 5837581 elements were used, also including a refinement level 3 on the edges and mid-section.

As verified in Figure 34 and Figure 35, boundary symmetry is acceptable and will improve computational effort.

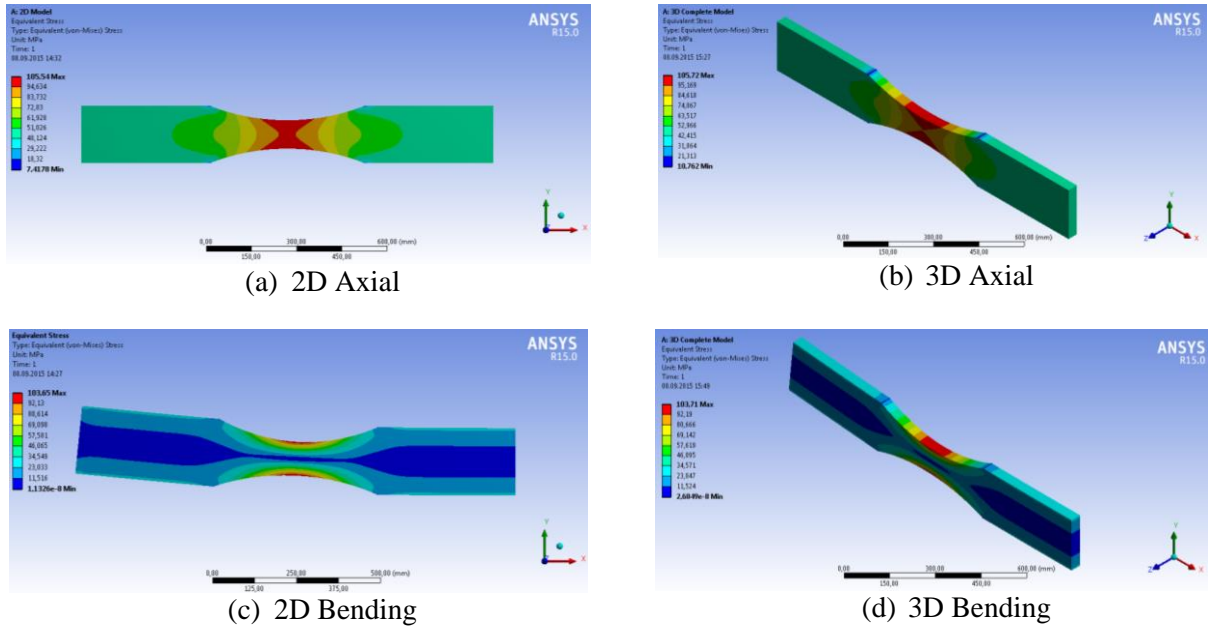


Figure 34 – Complete 2D and 3D Model Stress Result for Axial and Bending

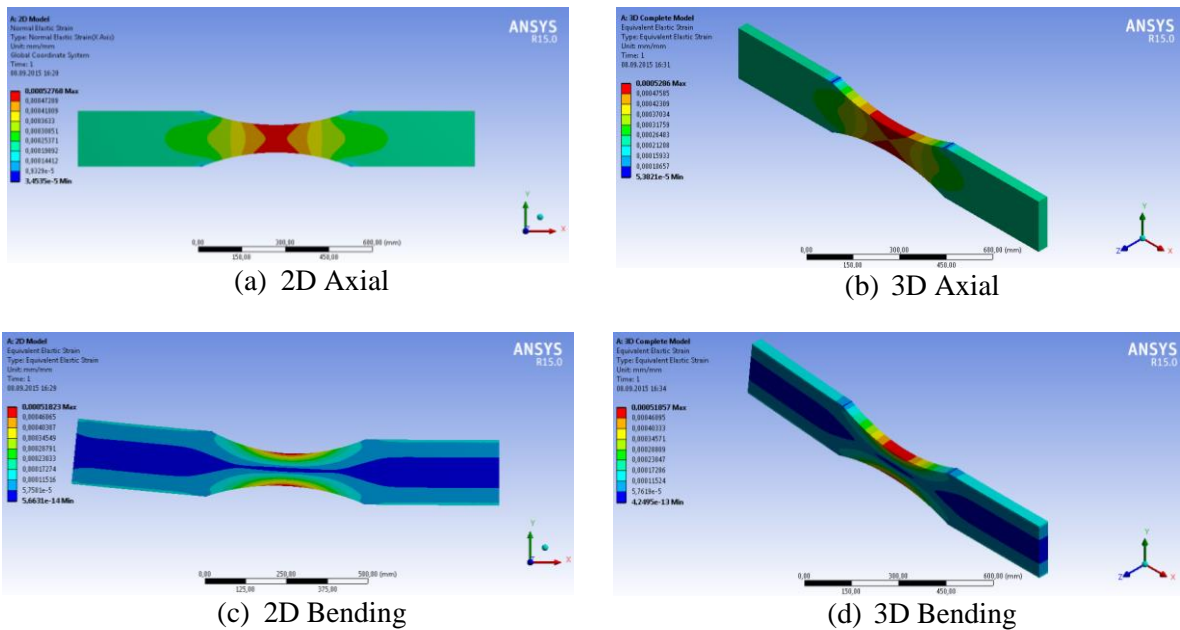


Figure 35 – Complete 2D and 3D Model Strain Result for Axial and Bending

Pure axial and 4-point pure bending loads will be considered on the simulations. Additional information about the reason why it is adopted 4-point bending case is that the volume under stress is greater when compared to the one under 3-point bending, exposing a larger volume of the material to the peak stress (Nordson DAGE 2011). Basically, *Weibull* statistics provides an understanding that the bigger the volume, higher probability to find a longer crack or flaw. Hence, it is expected that the mechanical strength measured by 4-point bending

test will be lower than if one measures by 3-point bending, in that way keeping a conservative analysis.

4.2.2 Boundary and Load for 2D and 3D Axial Analysis

According to Figure 34, one can easily consider the symmetry for axial and bending load cases. For the former, one quarter of the piece is enough to determine the stress on the specimen for 2D and 3D analyses. For the latter, the half piece can fulfill the requirements to achieve the stresses both in 2D and 3D environment. In addition for 3D models, the thickness also presents symmetry, thus only half size is considered.

Adopting the symmetry methodology, it will result in less computational time and effort (Lee 2014). However, one must pay good attention to the boundary conditions for each case.

As cited previously, the symmetry approach plays an important role in FEM analysis. After choosing the adequate symmetry for 2D and 3D problems, the boundary conditions and the applied loads are as follows for axial test:

- Displacement (Δu) in the symmetry related to y direction edge of the specimen is equal to zero in x direction, referred as “Displacement” in Figure 36;
- Likewise, the displacement in the symmetry related to x direction edge of the specimen is equal to zero in y direction, referred as “Displacement 2” in Figure 36;
- The load is established perpendicular to the outer edge of the specimen, in same direction of x axis, referred as “Pressure: -50, MPa” in Figure 36; and
- Due the symmetry of 3D analysis related to the thickness of the specimen, it is also consider no displacement on that surface for the z direction, as visualized in Figure 37.

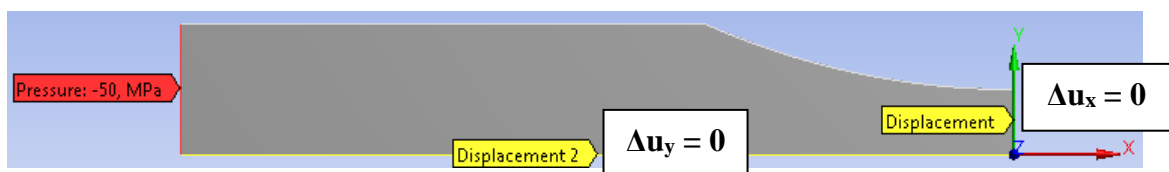


Figure 36 – Load and Boundary Conditions Configuration for 2D and 3D Axial

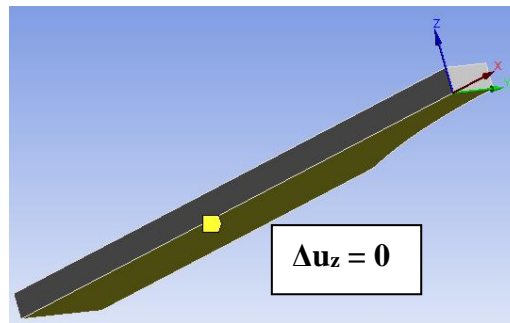


Figure 37 – Additional Boundary Condition for 3D

4.2.3 Boundary and Load for 2D and 3D Bending Analysis

Boundary conditions and the applied bending are as follows for 2D and 3D models:

- Displacement over x direction is constrained on the middle section of the specimen (edge for 2D and surface for 3D, respectively), as verified in Figure 38, also with no displacement on the edge for y direction, referred as “A Displacement” and “B Displacement 2”;
- Constant bending moment will depend on the thickness, as described in Table 10. As example for thickness of 80mm, bending moment of 6666666.67 N.m is applied on the end of the specimen (edge for 2D and surface for 3D), referred as “C Moment: -6,6667,e+006 N.mm” in Figure 38; and
- Once more, due the symmetry of 3D analysis related to the thickness of the specimen, it is also consider no displacement on that surface for the z direction exemplified in Figure 37, however for the whole surface.

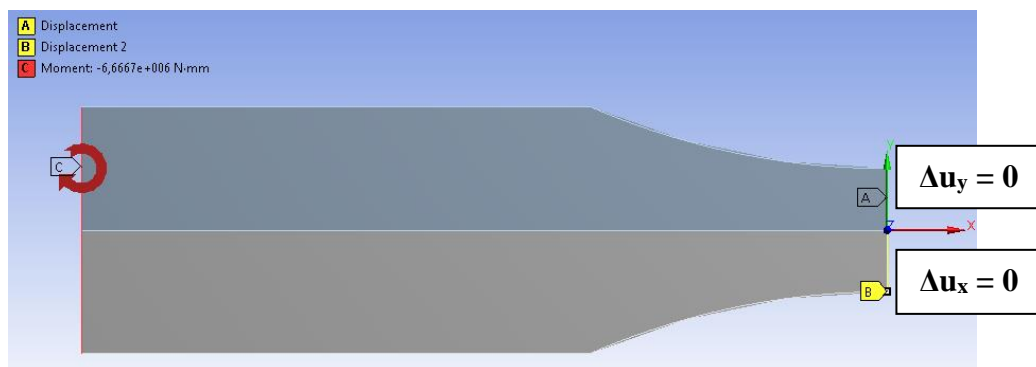


Figure 38 – Load and Boundary Conditions Configuration for 2D and 3D Bending

4.3 2D Model Plain Stress Analysis

4.3.1 2D Mesh Convergence

In order to certify that the results obtained from the simulation are accurate, one performs initially a convergence analysis varying the mesh. For that objective, nodes and elements are increased resulting in Figure 39. However, it is observed that only a simple mesh is enough for both axial and bending. More details can be seen in APPENDIX B.

Since the geometry of the specimen is slightly simple, a structured mesh is chosen as quadrilateral cell shape for case number 5. Some advantages can be exemplified for this consideration: better convergence, less computational time and higher resolution when compared to unstructured grids (Hebhardt 2011; Castillo 1991).

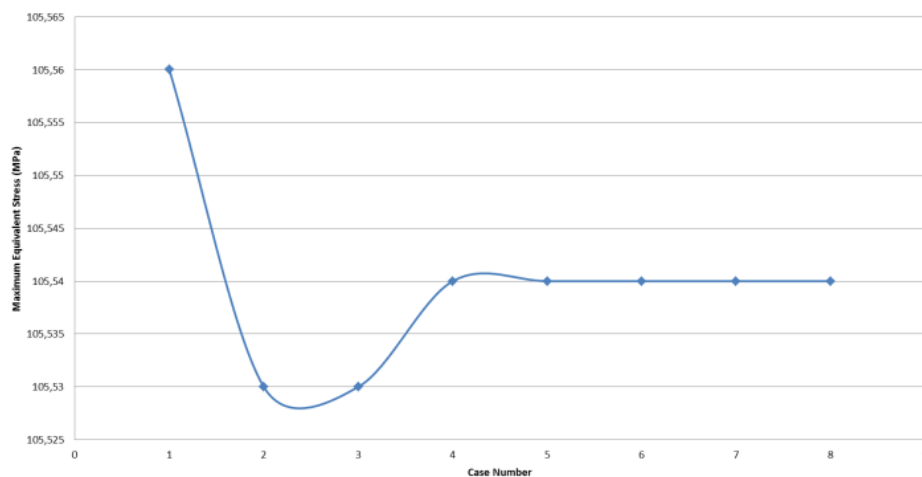


Figure 39 – Convergence Analysis Result for 2D Axial

4.3.2 2D Model – Tensile Simulation

Adopting the mesh established in Section 4.3.1, it is observed in Figure 40 that high values of stress are concentrated in the middle region of the specimen where the width is reduced. The highest calculated value is 105.54 MPa both considering Normal or *von-Mises* stresses respectively.

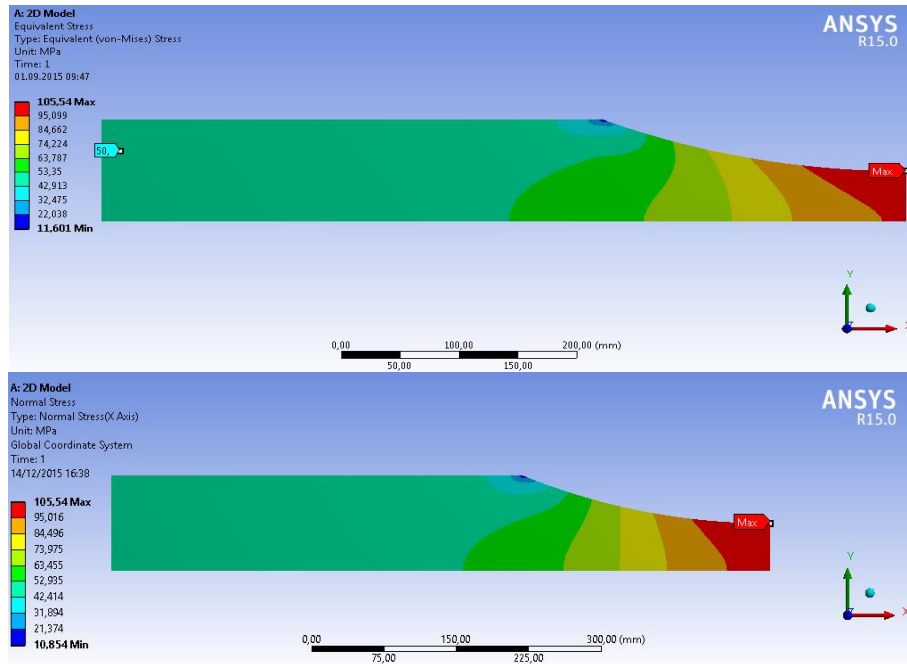


Figure 40 – Convergence Stress Result for 2D Axial

4.3.3 2D Model – Bending Simulation

Considering the same mesh established in Section 4.3.1 for axial symmetry, it is verified in Figure 41 that high values of stress are concentrated in the middle region of the specimen where the width is reduced and more distant from the neutral line. The highest *von-Mises* and Normal stresses calculated value are 103.65 MPa.

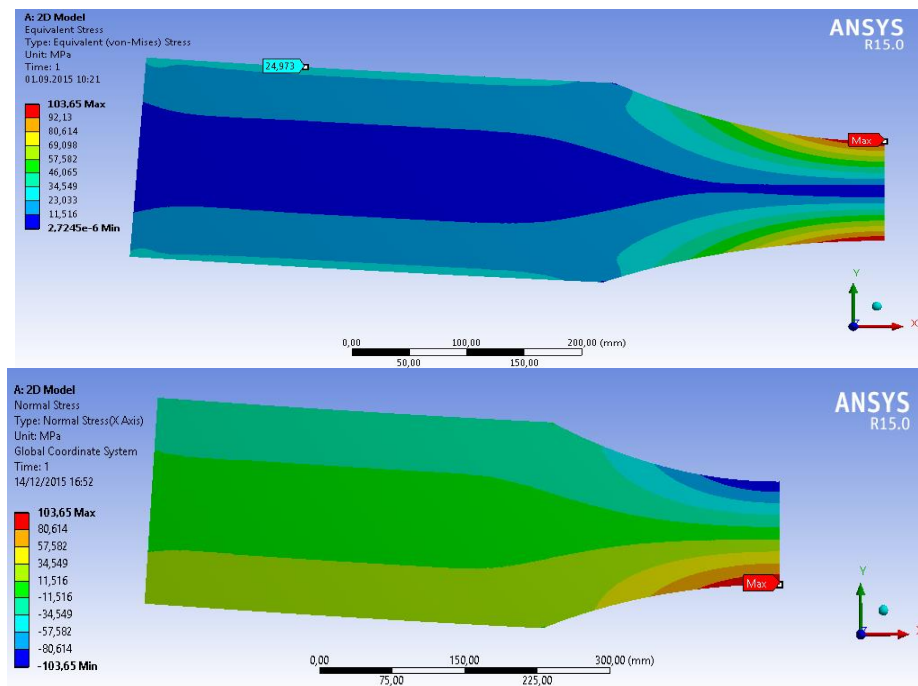


Figure 41 – Convergence Stress Result for 2D Bending

4.4 3D Model Solid Analysis

4.4.1 3D Mesh Convergence Analysis

For 3D convergence analysis, one performs a convergence analysis similar to 2D varying the mesh resulting in Figure 42, where there is no need for fine mesh in order to obtain a converged value and a relative error of magnitude very small, 0.00% for axial and 0.02% for bending. More details can be found in APPENDIX B.

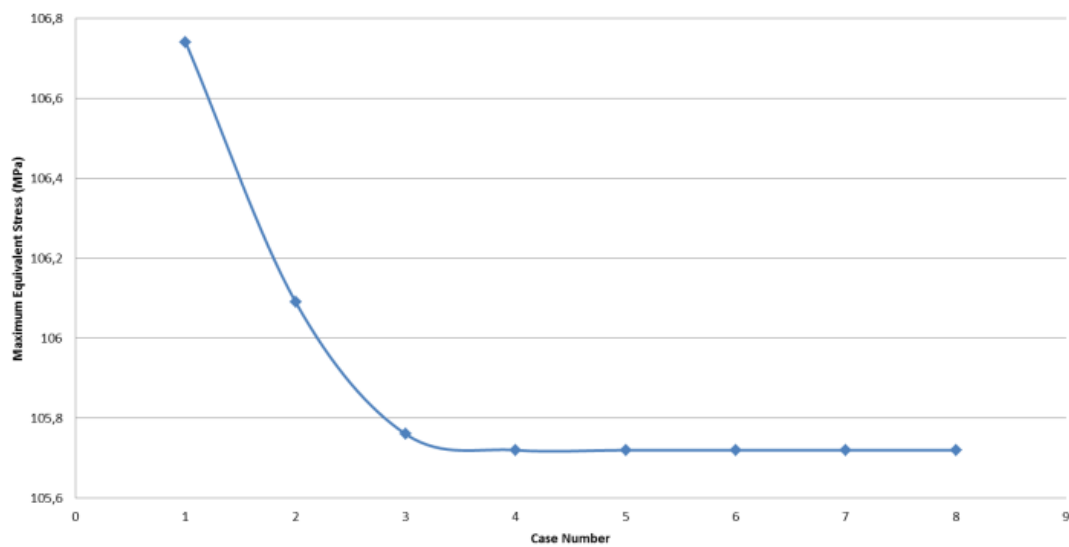


Figure 42 – Convergence Analysis Result for 3D Axial

It was considered at least 5 subdivision for the edge treatment surface, keeping aspect ratios $\Delta x/\Delta y$ and $\Delta x/\Delta z$ less than 3 (or 1/3) as well-known good practice (Hebhardt 2011) in order to better verify the stress distribution on the edge surface.

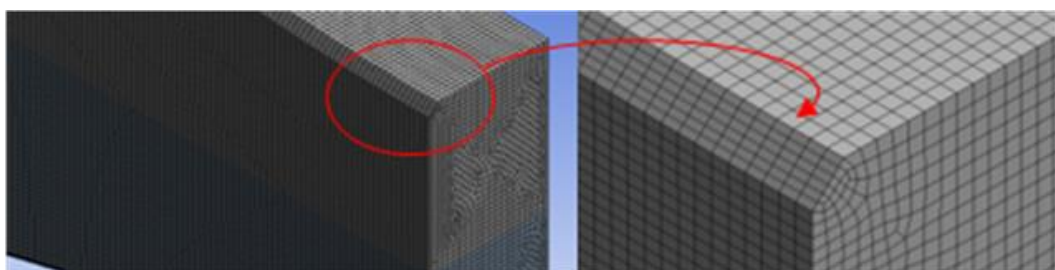


Figure 43 – Subdivision of Mesh for 3C Edge Treatment Surface

4.4.2 3D Model – Tensile Simulation

4.4.2.1 3D Model Thickness 80mm 3C – Tensile Simulation

Providing a 3C edge treatment as example, it is observed in Figure 44 that the high values of stress are concentrated in the middle region of the specimen where the width is reduced and the value is 105.84 MPa.

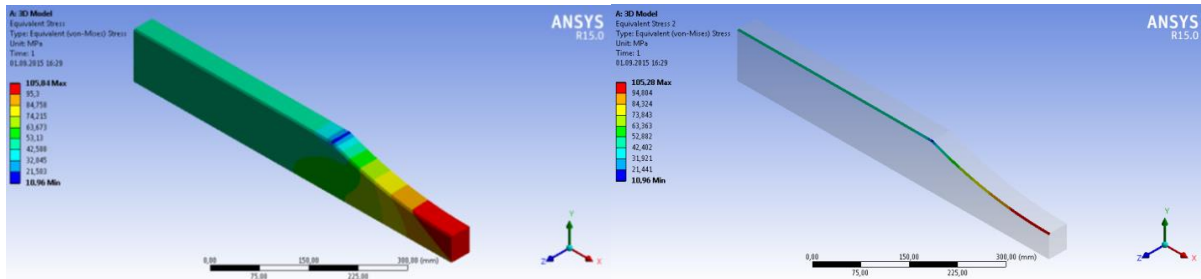


Figure 44 – Result for 3D Axial 3C with Thickness 80mm

4.4.2.2 3D Model Thickness 50mm 3C – Tensile Simulation

For thickness comparison, result for 3C edge treatment with 50mm of thickness is observed in Figure 45 that the high values of stress are concentrated in the middle region of the specimen where the width is reduced and the value is 105.82 MPa.

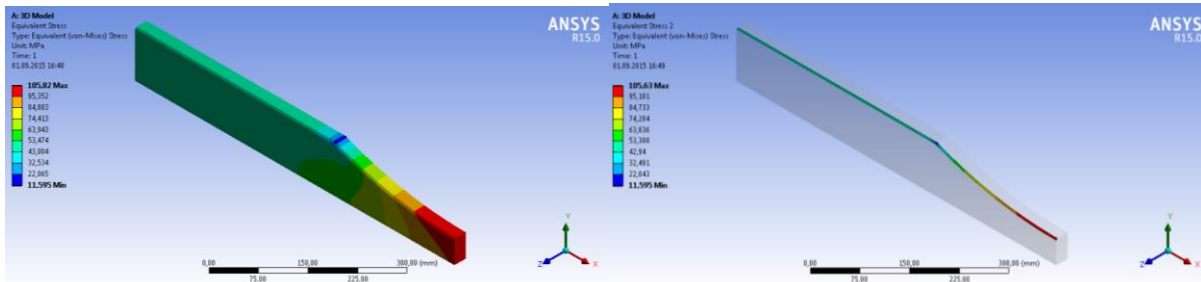


Figure 45 – Result for 3D Axial 3C with Thickness 50mm

4.4.2.3 3D Model Thickness 25mm 3C – Tensile Simulation

Result for the last thickness dimension of 25mm for a 3C edge treatment is observed in Figure 46. High value of stress is located in the middle region of the specimen, same as found for 80mm and 50mm, where the width is reduced and the value is 106.00 MPa.

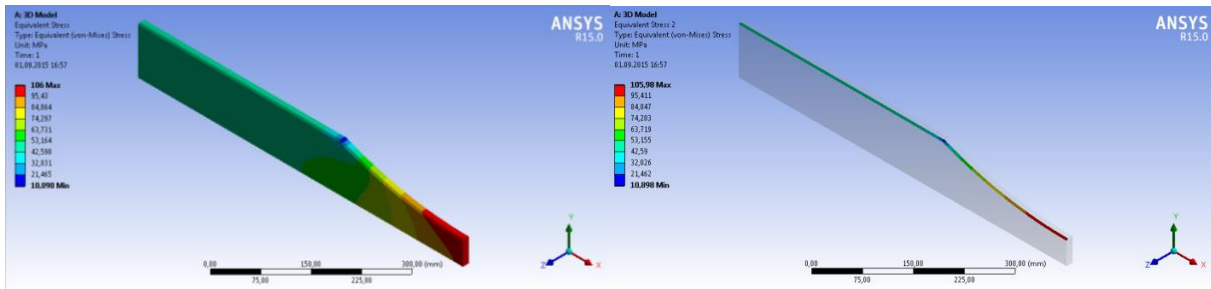


Figure 46 – Result for 3D Axial 3C with Thickness 25mm

4.4.2.4 Summary of 3D Model Results for Tensile Simulation

Complete summary for tensile simulation is observed in Figure 47 and stress concentration factor for axial load is verified in Table 11.

It is noted that there is a small difference between values for different edge treatment. Hence, the influence of edge treatment can be neglected.

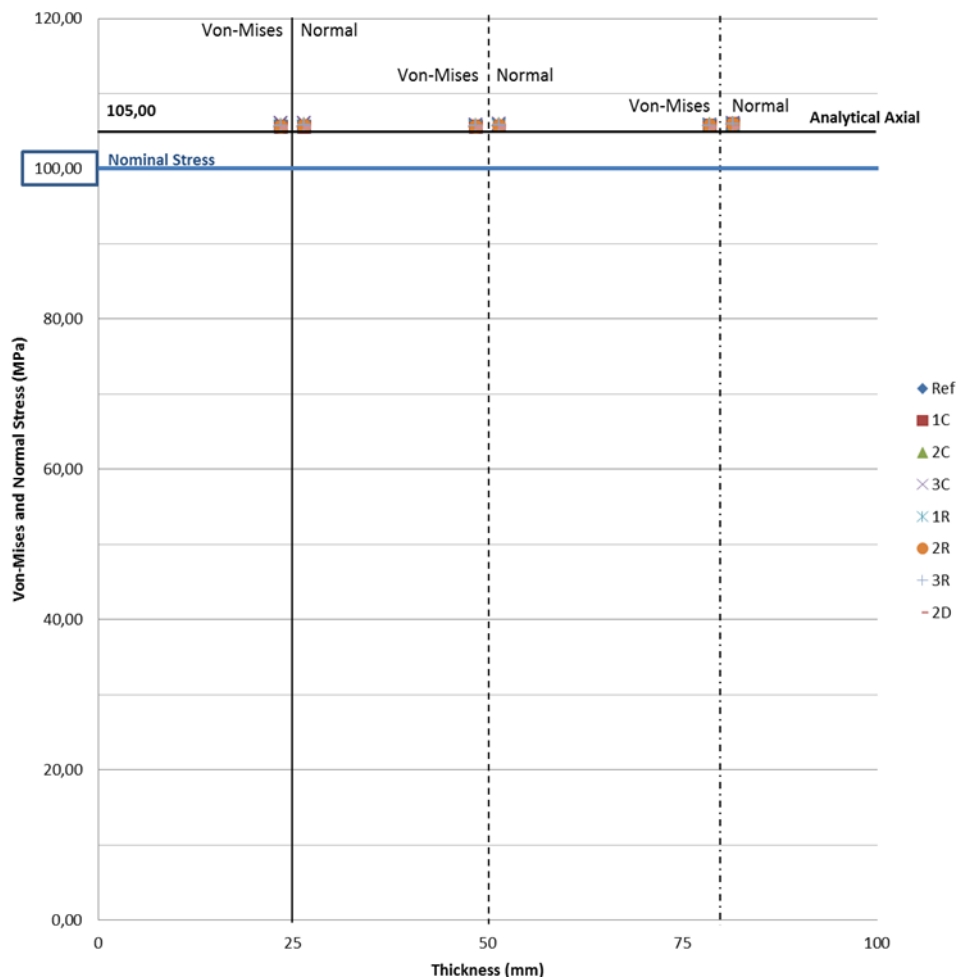


Figure 47 – Summary of Stress Result adopting FE for 3D Axial

Table 11 – Stress Concentration Factor Result for 3D under Axial Load

Stress	t (mm)	Analytical	K_t							
			2D	Ref	1C	2C	3C	1R	2R	3R
Normal	25	1.05	1.06	1.06	1.06	1.06	1.06	1.06	1.06	1.06
Equivalent	25	1.05	1.06	1.06	1.06	1.06	1.06	1.06	1.06	1.06
Normal	50	1.05	1.06	1.06	1.06	1.06	1.06	1.06	1.06	1.06
Equivalent	50	1.05	1.06	1.06	1.06	1.06	1.06	1.06	1.06	1.06
Normal	80	1.05	1.06	1.06	1.06	1.06	1.06	1.06	1.06	1.06
Equivalent	80	1.05	1.06	1.06	1.06	1.06	1.06	1.06	1.06	1.06

Considering only the stress verified on the edge of the specimen APPENDIX B, there is once more no high influence of edge treatment on the stress result.

Stress distribution is verified in Figure 48 for 3C edge treatment for tensile simulation and values can be observed in Figure 49. Maximum stress of 105.84 MPa is verified on the middle of specimen's thickness, reducing when reaching the middle of specimen's width to stress of 95.22 MPa. This behavior is similar for all specimens.

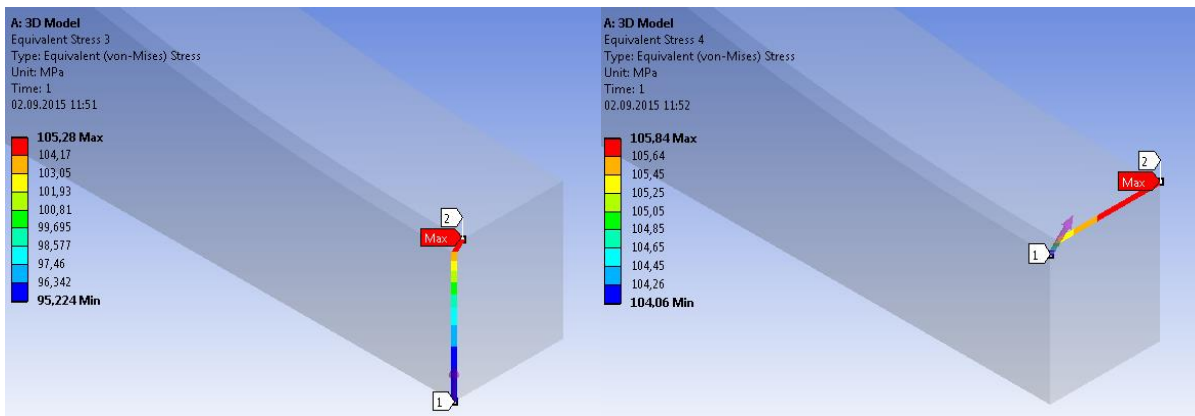


Figure 48 – Stress Distribution for 3C Thickness 80mm under Axial Load

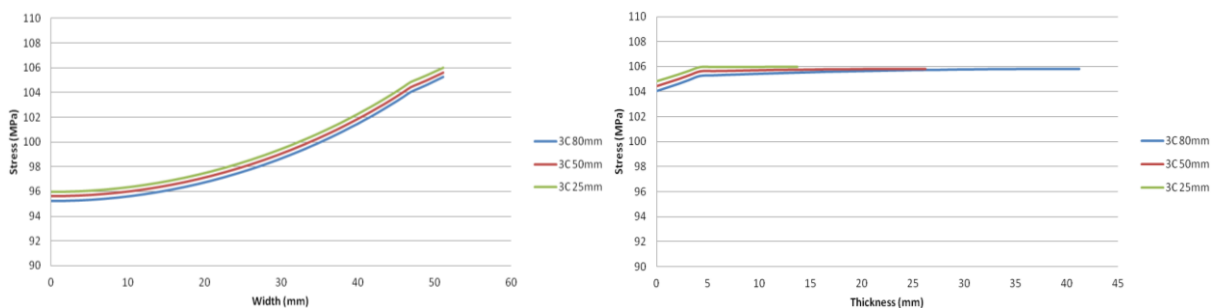


Figure 49 – Stress Distribution Values for 3C under Axial Load

4.4.3 3D Model – Bending Simulation

4.4.3.1 3D Model Thickness 80mm 3C – Bending Simulation

Providing a 3C edge treatment, it is observed in Figure 50 that the high values of stress are concentrated in the middle region of the specimen where the width is reduced and the value is 104.37 MPa.

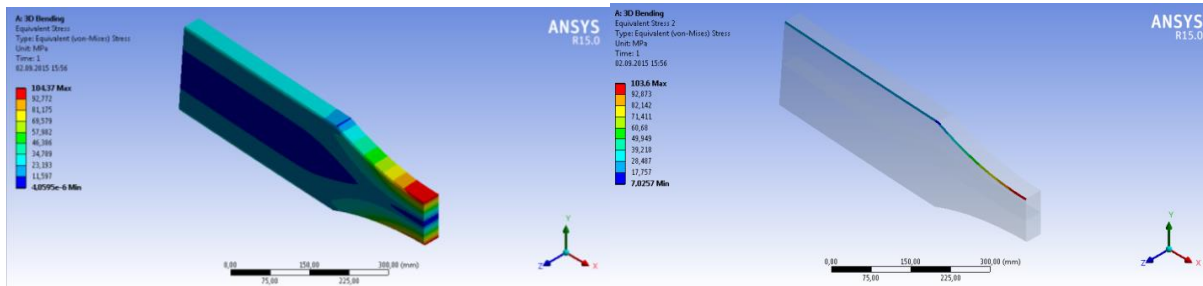


Figure 50 – Result for 3D Bending 3C with Thickness 80mm

4.4.3.2 3D Model Thickness 50mm 3C – Bending Simulation

Providing a 3C edge treatment, it is observed in Figure 51 that the high values of stress are concentrated in the middle region of the specimen where the width is reduced and the value is 104.84 MPa.

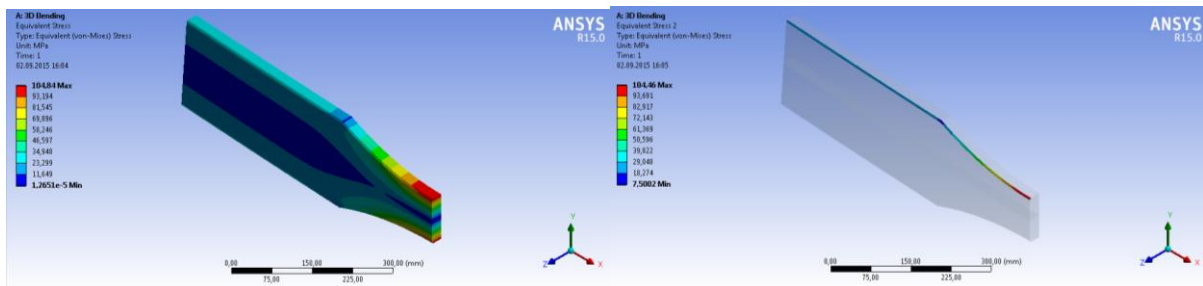


Figure 51 – Result for 3D Bending 3C with Thickness 50mm

4.4.3.3 3D Model Thickness 25mm 3C – Bending Simulation

Providing a 3C edge treatment, it is observed in Figure 52 that the high values of stress are concentrated in the middle region of the specimen where the width is reduced and the value is 105.94 MPa.

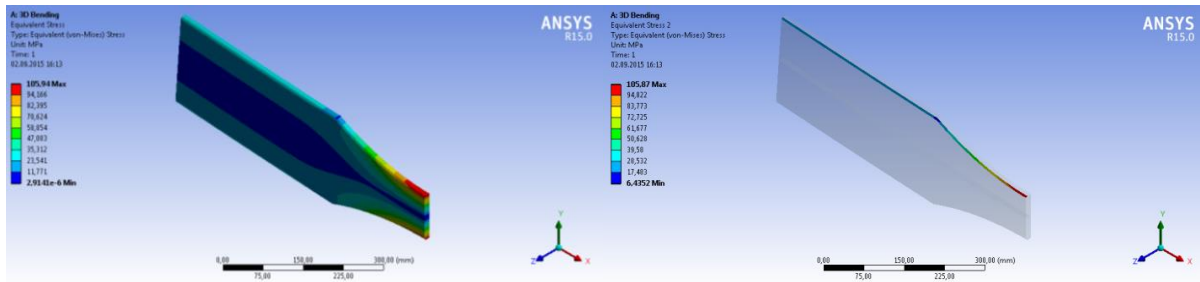


Figure 52 – Result for 3D Bending 3C with Thickness 25mm

4.4.3.4 Summary of 3D Model Results for Bending Simulation

A complete summary for bending simulation is provided in Figure 53. As it was also verified in Figure 47 for axial load, no significant influence of edge treatments is found for the stresses under bending, either *von-Mises* or Normal. Table 12 presents stress concentration factors for each edge treatment.

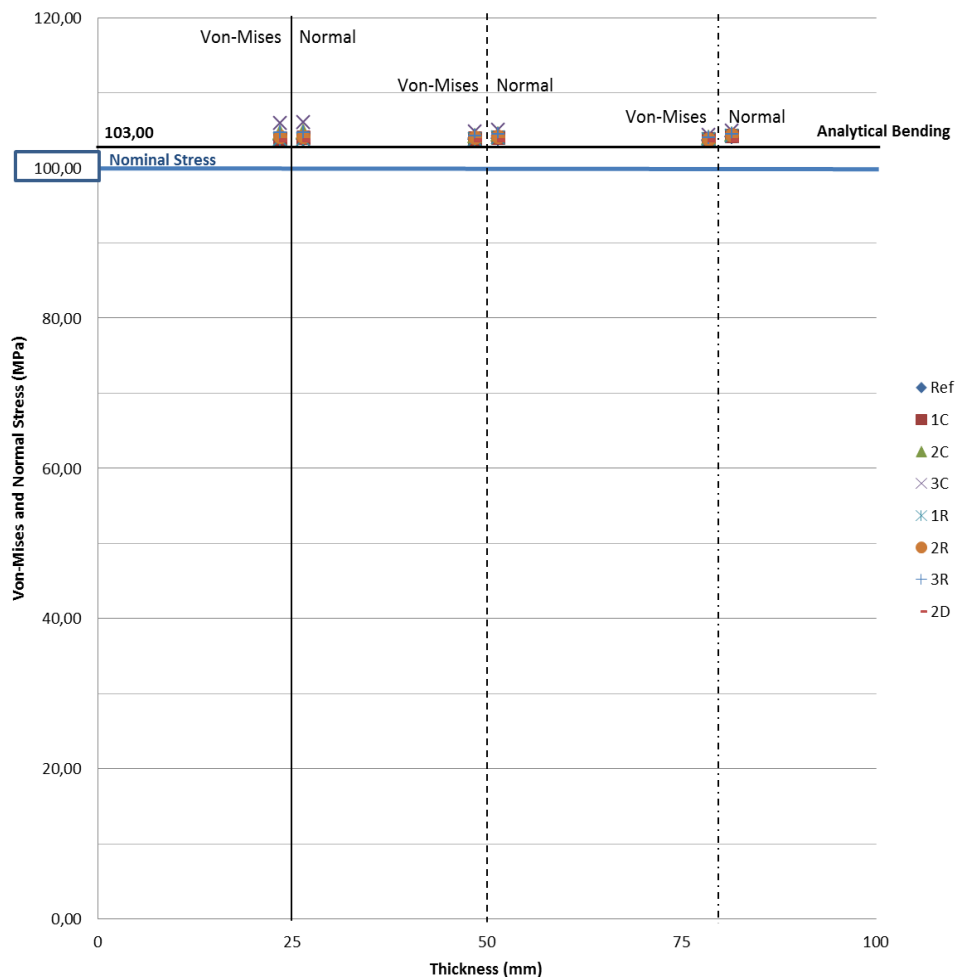


Figure 53 – Summary of Stress Result adopting FE for 3D Bending

Table 12 – Stress Concentration Factor Result for 3D under Bending Load

Stress	t (mm)	Analytical	K_t							
			2D	Ref	1C	2C	3C	1R	2R	3R
Normal	25	1.03	1.04	1.04	1.04	1.05	1.06	1.04	1.04	1.05
Equivalent	25	1.03	1.04	1.04	1.04	1.05	1.06	1.04	1.04	1.05
Normal	50	1.03	1.04	1.04	1.04	1.04	1.05	1.04	1.04	1.04
Equivalent	50	1.03	1.04	1.04	1.04	1.04	1.05	1.04	1.04	1.04
Normal	80	1.03	1.04	1.04	1.04	1.04	1.05	1.04	1.04	1.04
Equivalent	80	1.03	1.04	1.04	1.04	1.04	1.04	1.04	1.04	1.04

Considering only the stress verified on the edge of the specimen APPENDIX B, there is once more no high influence of edge treatment on the stress result.

Stress distribution is verified in Figure 54 for 3C edge treatment for tensile simulation and values can be observed in Figure 55. Maximum stress of 105.84 MPa is verified on the middle of specimen’s thickness, reducing when reaching the middle of specimen’s width to stress of 95.22 MPa. This behavior is similar for all specimens.

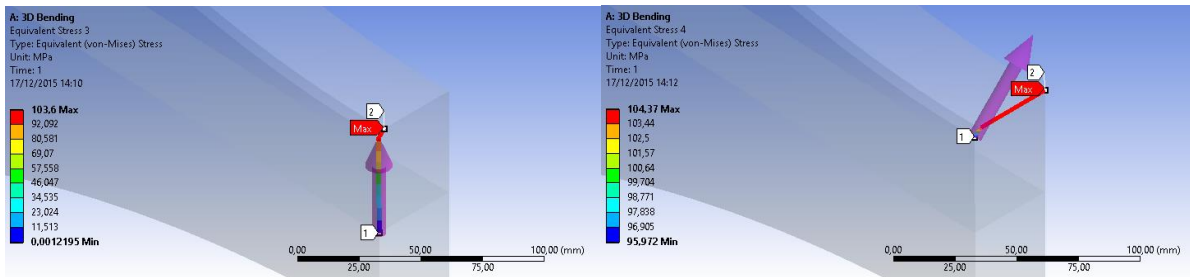


Figure 54 – Stress Distribution for 3C Thickness 80mm under Bending Load

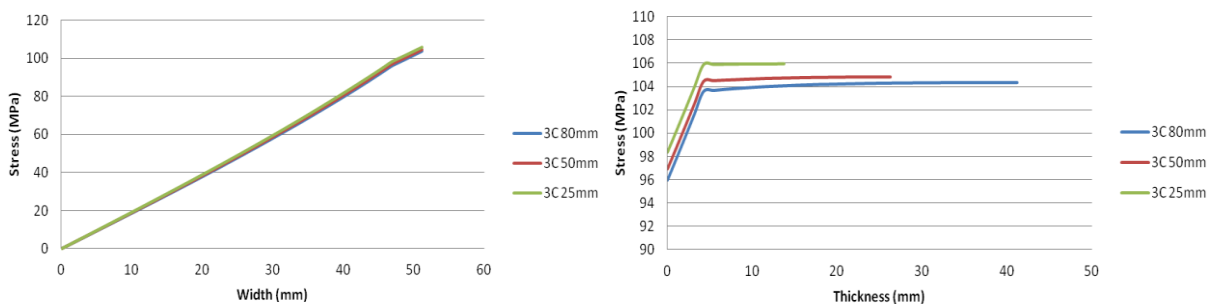


Figure 55 – Stress Distribution Values for 3C under Bending Load

4.5 Crack Propagation Analysis of Thermal Cut Edge Specimen

After finding the influence on the stress applied on the specimen due to distinct edge treatments in Sections 4.1-4.4, fracture mechanics analysis is carried out herein considering the same geometries of the specimen observed in Figure 30 (hourglass shape) for the middle section for three different thicknesses according to Figure 56.

Results obtained from this simulation analysis will help DNV GL to better understand the experimental results from specimens over axial and bending loads, including different response for distinct crack model and stress ranges.

Parameters adopted for the simulation were according to FKM Guideline (Berger et al. 2009) and they are described in Table 13.

Table 13 – *Paris-Erdogan* Parameters for Thermal Cut Edges Simulation (Berger et al. 2009)

Material	C (-)	ΔK_{th} (MPa·mm^{1/2})	K_c (mm)	m (-)
YP36	$5.96 \cdot 10^{-9}$	8.20	1000	2.88
YP40	$3.15 \cdot 10^{-9}$	10.40	1000	3.07
YP47	$5.67 \cdot 10^{-8}$	8.30	1000	2.26

Different stress ranges values observed in Table 14 are considered similar to what was done in Selle et al. (2011) and stress ratio $R = 0.1$ in order to keep the specimen in tension at one side along the tests.

Table 14 – Stress Values Adopted for Crack Propagation of Thermal Cut Edges

$\Delta\sigma$ (MPa)	σ_{max} (MPa)	R (-)	σ_{min} (MPa)	σ_{mean} (MPa)
252.00	280.00	0.10	28.00	154.0
270.00	300.00	0.10	30.00	165.0
306.00	340.00	0.10	34.00	187.0
360.00	400.00	0.10	40.00	220.0
423.00	470.00	0.10	47.00	258.5

According to Remes et al. (2013), Berglund (2006) and limitation on *Fraunhofer IWM Verb* software, the smallest initial crack size that have worked for all material properties for quarter-elliptical and semi-elliptical was a_0 equals to 1.1mm and c_0 or $2c_0$ equals to 1.1mm, corresponding to slightly more than 1% of the thickness (a_0/t) and the biggest value of around 9% from width (c_0/W or $2c_0/2W$).

Also, it was necessary to change thickness (t) with width (W or $2W$) in *IWM Verb* mainly due to 4-point bending simulation to locate the bending stress distribution on top specimen surface, which is inside the software related to thickness.

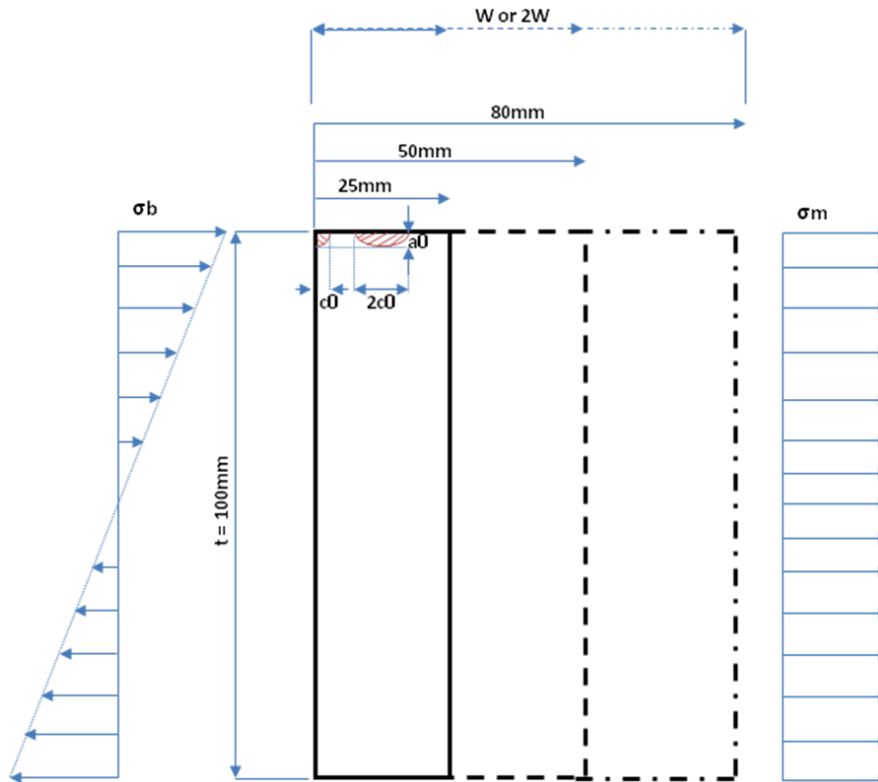


Figure 56 – Sketch for Specimen Geometries and Stress Distribution

4.5.1 Thermal Cut Edge Crack Propagation Analysis for Axial Load

4.5.1.1 Thermal Cut Edge Quarter Corner Crack Results for Axial

As mentioned before and observed in Remes et al. (2013), cracks after fatigue test regarding thermal cut pieces are mostly described by elliptical shapes or extended surface cracks. Due to that reason, semi elliptical and quarter corner elliptical crack models are considered with the smallest possible size for simulating cracks mainly observed in thermal cut surfaces (Jonsson 2015).

In Figure 57 to Figure 62, it is established the simulation for quarter corner crack for YP36, YP40 and YP47 materials respectively for distinct stress ranges. At certain point after crack propagation, more precisely when the width W is totally lost as seen in Figure 58 (grey lines), it is necessary to modify the model for the other dimension (red lines), *i.e.* crack depth, from

quarter corner to extended surface crack model and continue the simulation as verified in Figure 57. Similar cases can be seen in Figure 59 to Figure 62.

In all cases, smaller lifetime is achieved when increasing the stress range. For higher stress range, there is almost no difference between different widths. However, for most of the cases, the bigger the thickness higher is the lifetime of the specimen. After the crack propagates on full width dimension, only a few numbers of cycles is added for the thickness dimension. This effect is reversed for smaller stress range.

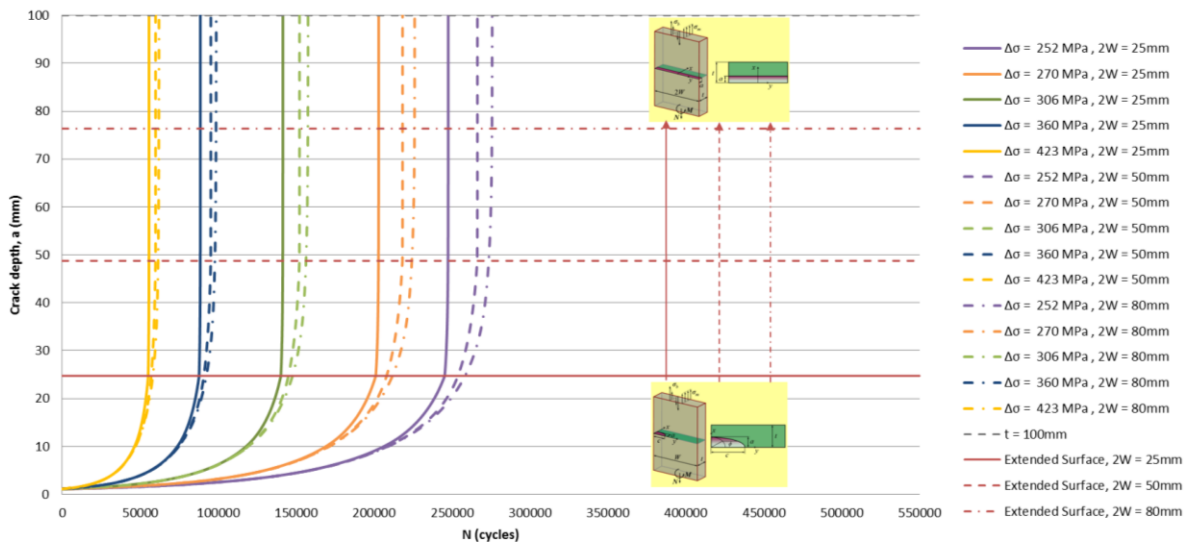


Figure 57 – Quarter Corner Crack Depth Propagation for YP36 for Different Stress Ranges under Axial Load

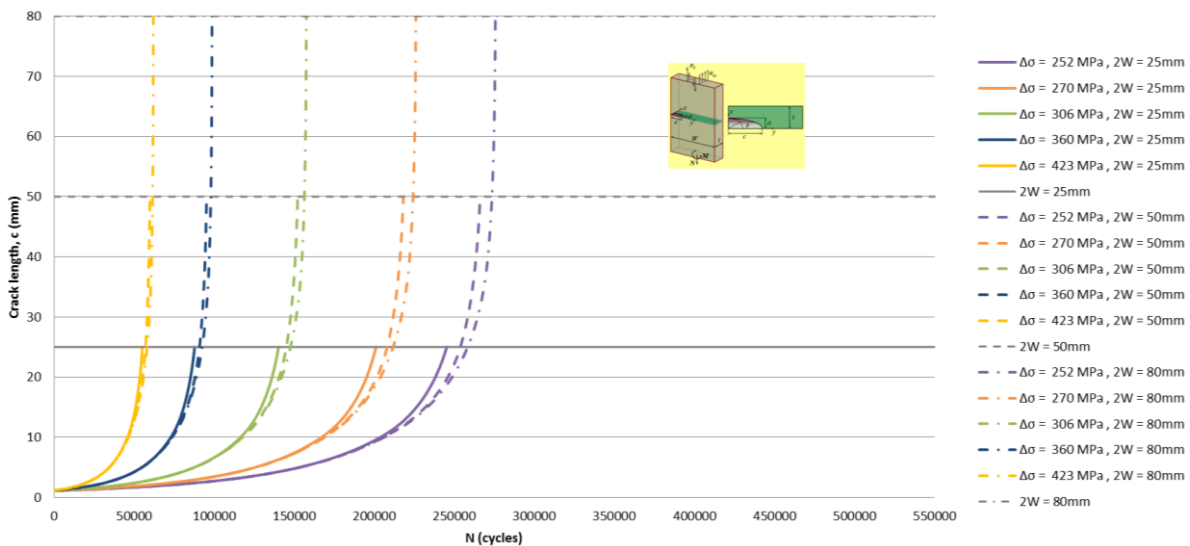


Figure 58 – Quarter Corner Crack Length Propagation for YP36 for Different Stress Ranges under Axial Load

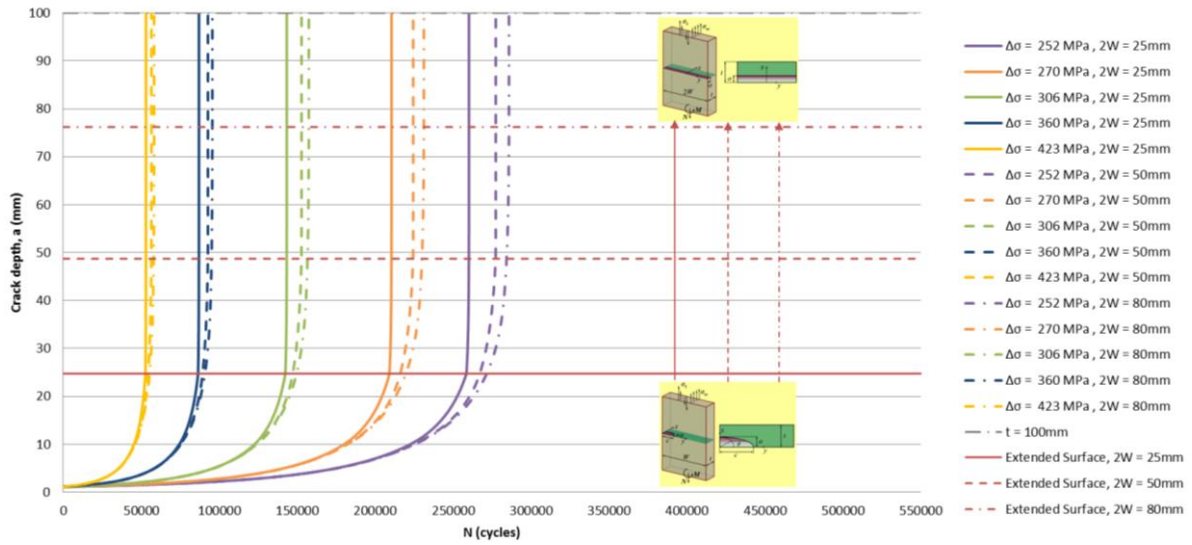


Figure 59 – Quarter Corner Crack Depth Propagation for YP40 for Different Stress Ranges under Axial Load

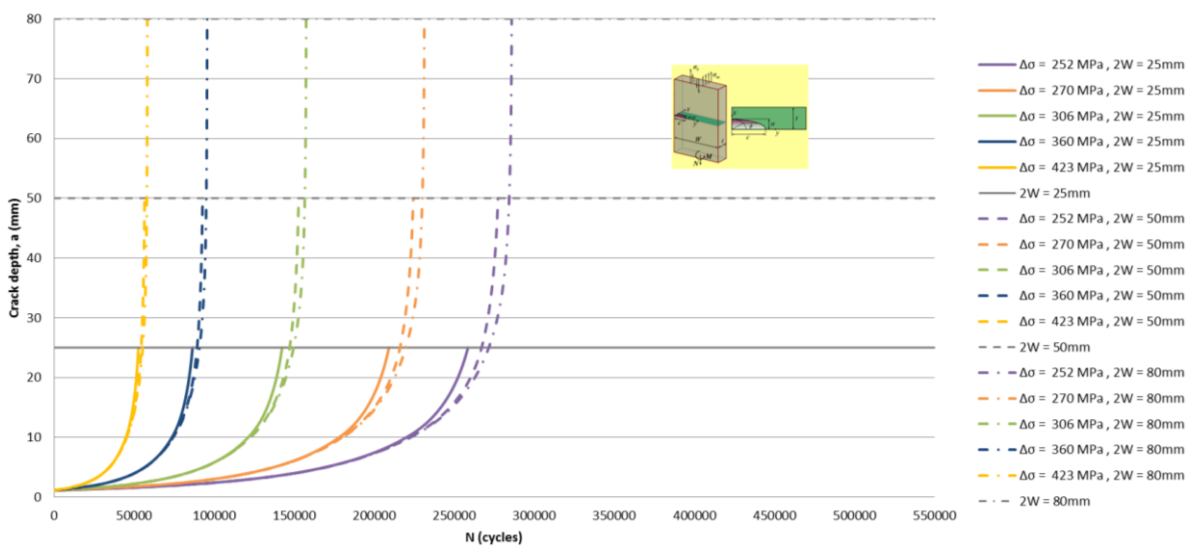


Figure 60 – Quarter Corner Crack Length Propagation for YP40 for Different Stress Ranges under Axial Load

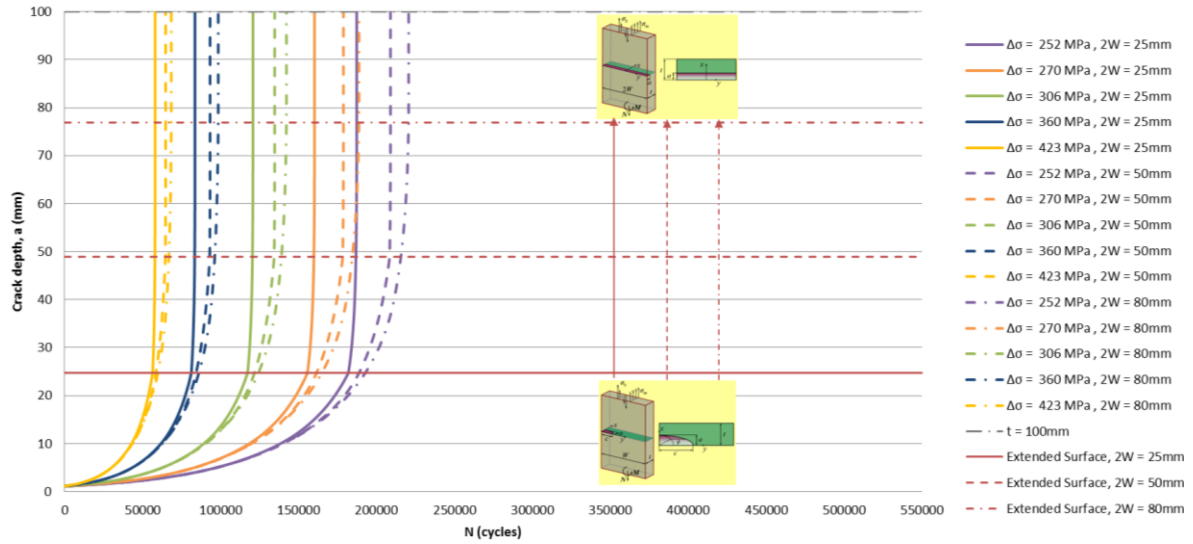


Figure 61 – Quarter Corner Crack Depth Propagation for YP47 for Different Stress Ranges under Axial Load

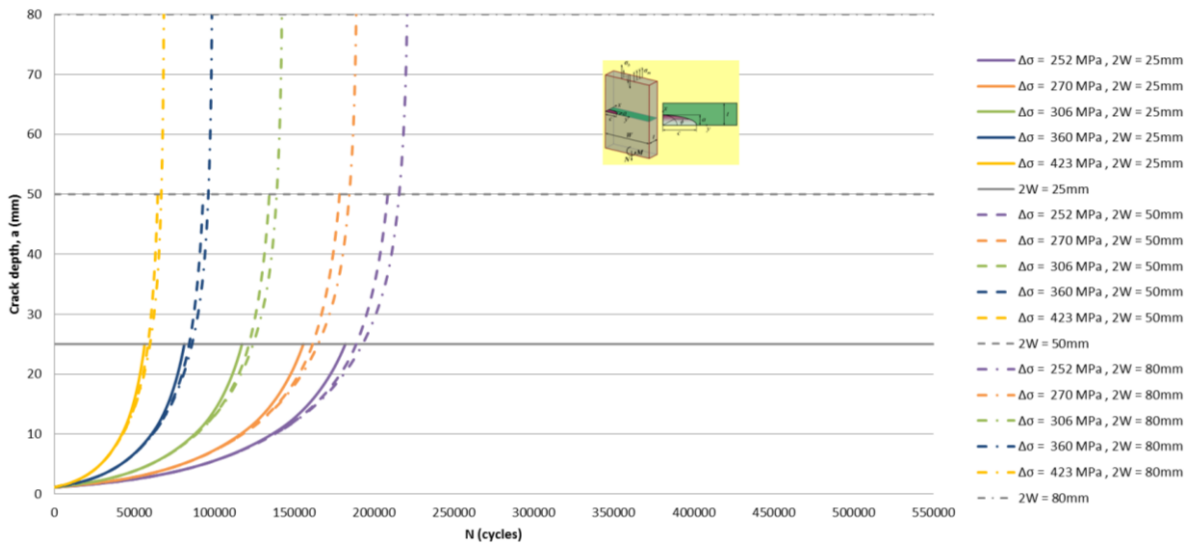


Figure 62 – Quarter Corner Crack Length Propagation for YP47 for Different Stress Ranges under Axial Load

A summary of all results for corner crack is presented in Figure 63. Results for number of cycles are concentrated in the range between $5 \cdot 10^4$ and $3 \cdot 10^5$. Despite of what was already enunciated, one can observe an improvement on lifetime when increasing the strength of material keeping thickness constant, for instance going from YP36 to YP40, which is according to Germanischer Lloyd (2015) for material effect on free edges steel plate as seen below:

$$f_m = 1 + \frac{R_{eH} - 235}{1200} \quad (31)$$

On the other hand, YP47 material does not present such effect. It can be highlighted from Table 14 the value of *Paris-Erdogan* constant *C* which is 10 times greater than the values from YP36 and YP40. Therefore, further investigation should certainly be conducted.

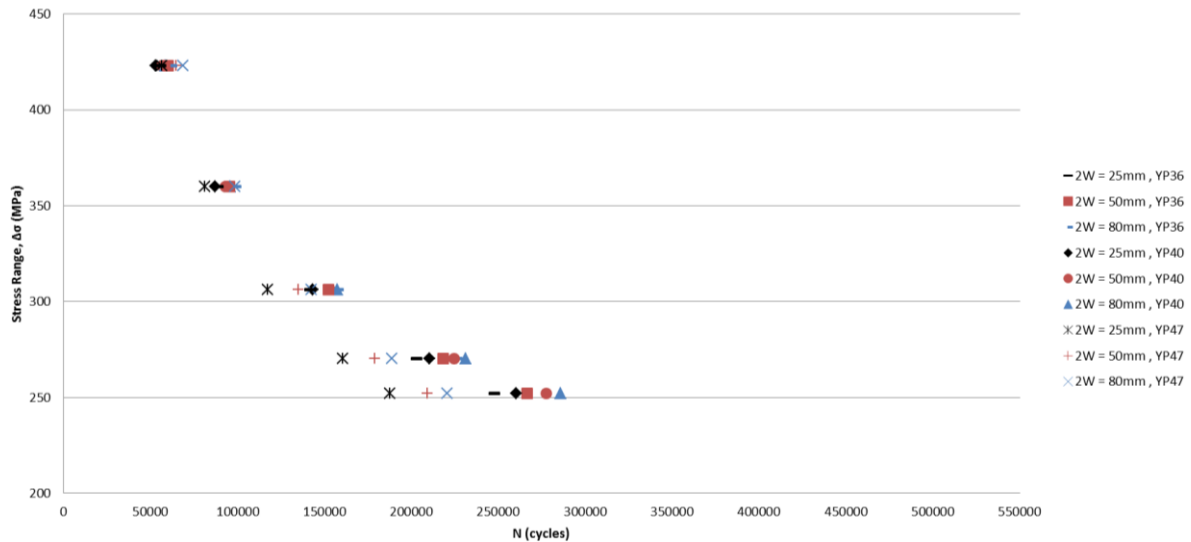


Figure 63 – Summary of Quarter Corner Crack Propagation for TCE under Axial

4.5.1.2 Thermal Cut Edge Semi-Elliptical Crack Results for Axial

Similar results for crack propagation on both dimensions can be verified for semi-elliptical crack models. For this reason, results graphs are included in APPENDIX B.

A summary of all results for semi-elliptical crack is presented in Figure 64. Results for number of cycles are concentrated in the range between $5 \cdot 10^4$ and $4.5 \cdot 10^5$.

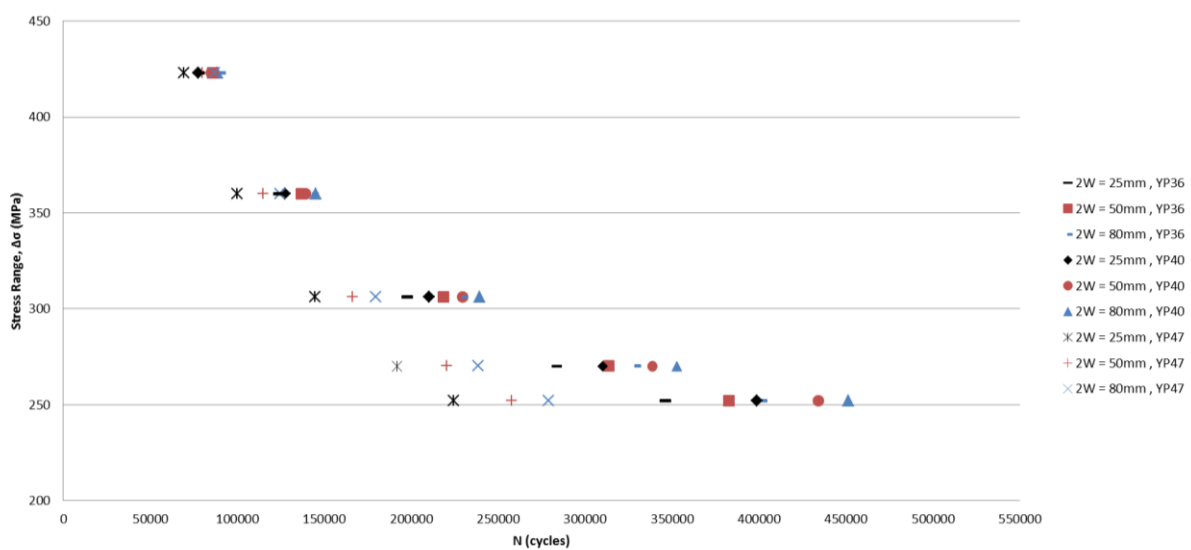


Figure 64 – Summary of Semi-Elliptical Crack Propagation for TCE under Axial Load

4.5.2 Thermal Cut Edge Crack Propagation Analysis for Bending Load

4.5.2.1 Thermal Cut Edge Quarter Corner Crack Results for Bending

Similar results for crack propagation on both dimensions can be verified for semi-elliptical crack models. For this reason, results graphs are included in APPENDIX B.

A summary of all results for semi-elliptical crack is presented in Figure 65. Results for number of cycles are concentrated in the range between $5 \cdot 10^4$ and $3.8 \cdot 10^5$. When compared with axial results, there is an enhancement in lifetime due to bending which will be described later.

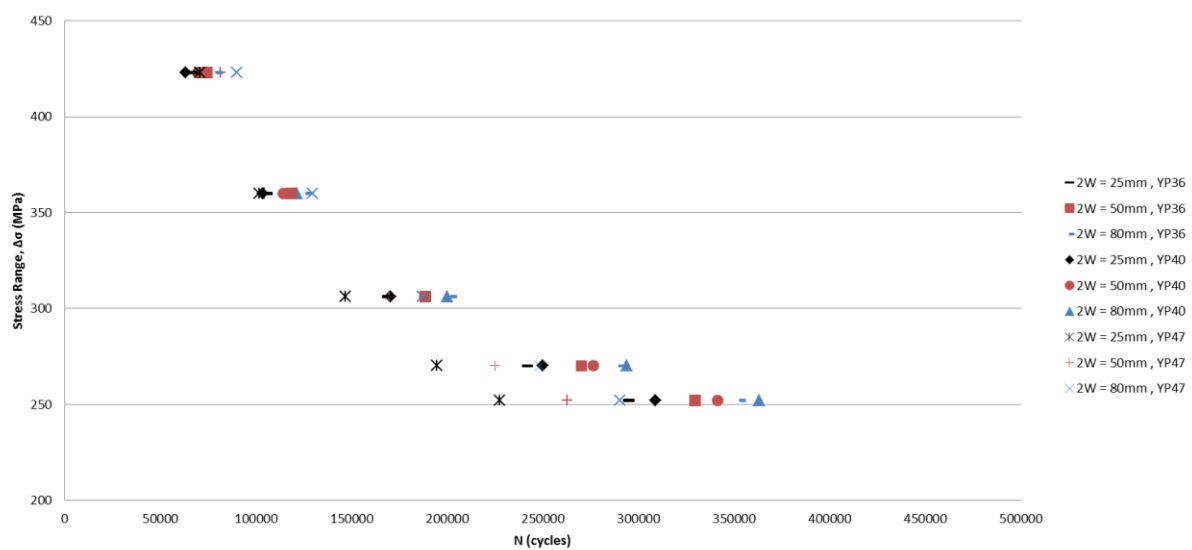


Figure 65 – Summary of Quarter Corner Crack Propagation for TCE under Bending Load

4.5.2.2 Thermal Cut Edge Semi-Elliptical Crack Results for Bending

Once more, similar results for crack propagation on both dimensions can be verified for semi-elliptical crack models when compared to axial. For this reason, results graphs are included in APPENDIX B.

A summary of all results for semi-elliptical crack is presented in Figure 66. Results for number of cycles are concentrated in the range between $6 \cdot 10^4$ and $5.3 \cdot 10^5$. Largest scatter can be verified for semi-elliptical crack under axial load, which led to conclusion that quarter corner crack are more severe than semi-elliptical ones.

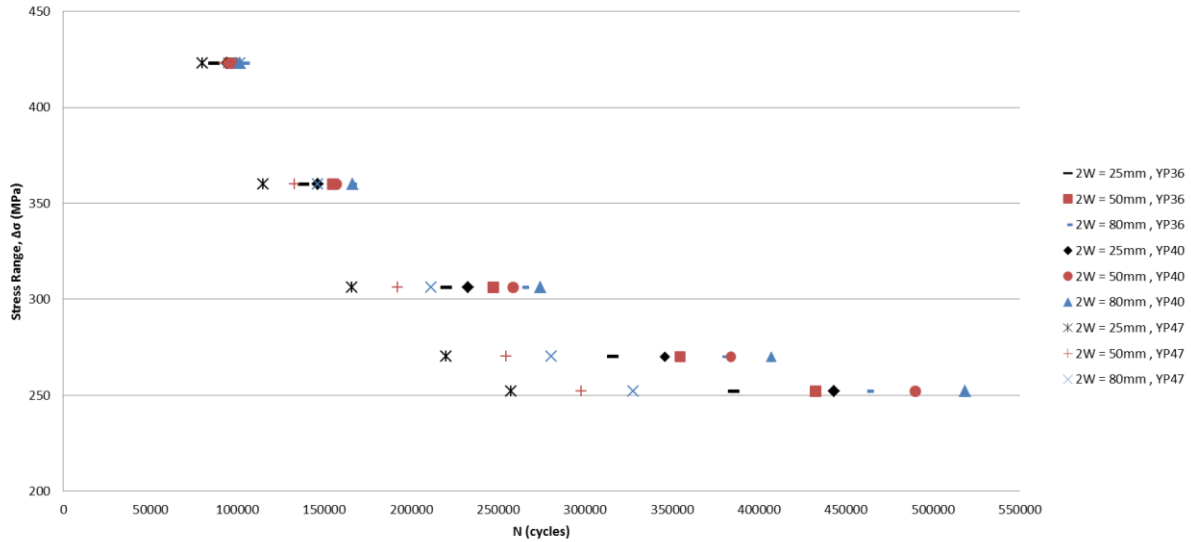


Figure 66 – Summary of Semi-Elliptical Crack Propagation for TCE under Bending Load

4.6 Comparison between Axial and Bending Loads for Thermal Cut Edges

As carried out for butt welded joints with internal lack of fusion in Chapter 3.1.4, it also investigated the enhancement on fatigue strength due to bending for thermal cut edges. For this propose, one takes into account the number of cycles from axial results obtained in Chapter 4.5 and varies the stress under pure bending until reach the same lifetime. Later on, this stress is recorded and compared to axial by simple formulation:

$$k_b = \frac{\sigma_b}{\sigma_a} = \frac{\Delta\sigma_{\Omega=1}}{\Delta\sigma_{\Omega=0}} \quad (32)$$

with degree of bending already described by Eq. (15), which the values analyzed were:

$$\Omega = \frac{\sigma_b}{\sigma_t} = \frac{\sigma_b}{(\sigma_b + \sigma_a)} = \begin{cases} 1, & \text{for pure bending} \\ 0, & \text{for pure axial} \end{cases} \quad (33)$$

4.6.1 Crack Propagation Comparison for Quarter-Elliptical Crack

As observed in Figure 67 for quarter corner crack, fatigue strength enhancement (kb) range is in between values of 1.13 and 1.05. The bigger the thickness higher value of kb is achieved. In addition, YP47 presents higher kb values. Nevertheless, YP47 material parameters are still doubtful. For the other two materials YP36 and YP40, higher strength material presents less fatigue strength enhancement, indeed with small difference between them when analyzing for the same thickness.

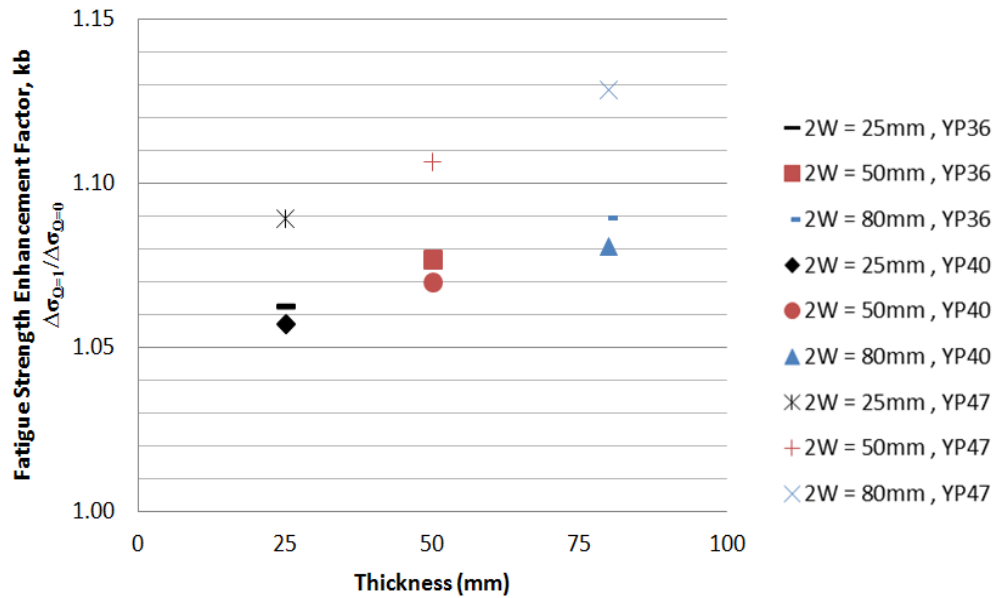


Figure 67 – Crack Propagation Comparison for Quarter Corner TCE under Axial Load

4.6.2 Crack Propagation Comparison for Semi-Elliptical Crack

No huge discrepancies are verified for semi-elliptical crack model, as seen in Figure 68 about the behavior of fatigue strength enhancement (kb). In fact, its values are in between slightly smaller range, 1.03 and 1.08. There is almost no difference between YP36 and YP40 results and the parameters for YP47 requires more investigation. Slope for the same material analysis is just a few smaller than the one for quarter corner crack.

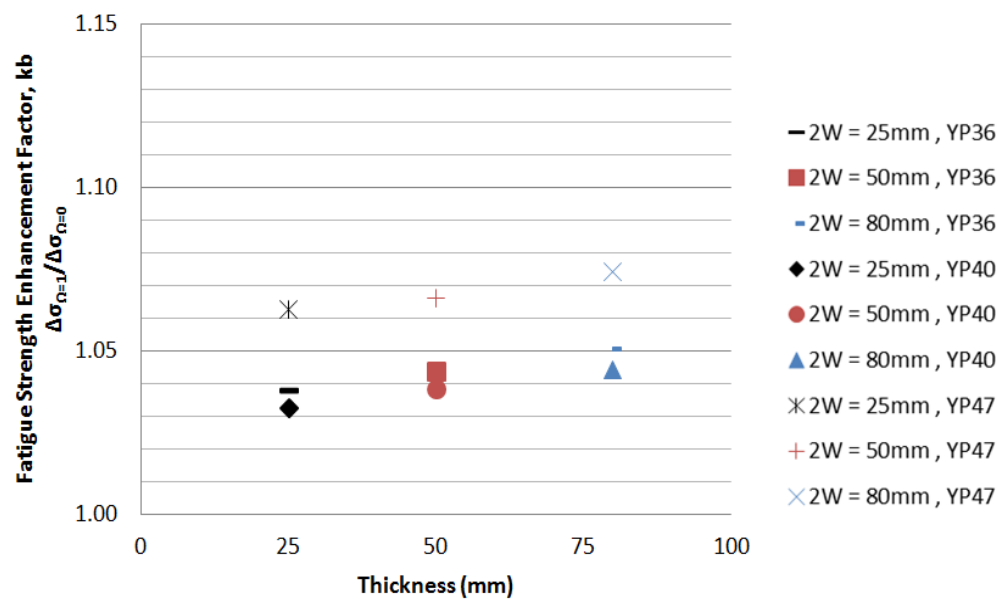


Figure 68 – Crack Propagation Comparison for Semi Elliptical TCE under Axial Load

4.7 Fracture Assessment under Variable Load

Normally, fatigue and fracture mechanics are calculated considering constant stress, such as what was carried out in Chapters 3 and 4 (in Subsections 4.5 and 4.6).

In actual situation, randomness of the loads is verified and, assuming that the crack initiation has already started due to some reason, one can calculate the lifetime of a plate with initial crack on its surface located on coaming area of a containership by fracture mechanics approach. This calculation can provide an idea of the lifetime of a plate which was originally thermally cut and, furthermore, it can give an inspection perspective for maintenance.

Long-term distribution of stress range, also known as stress range spectrum, can easily describe the stress ranges which may be encountered during the service life of the ship or specific structural component. Standard stress range spectra A (straight line) in Figure 69 is used in scenarios of seaway-induced stresses, comprising a design lifetime of around 20 years with a number of cycles $n_{\max} 5.0 \cdot 10^7$.

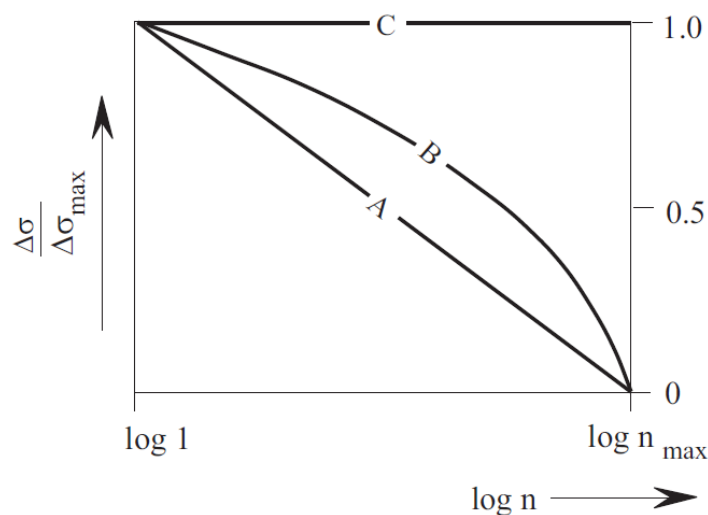


Figure 69 – Standard Stress Range Spectra A, B and C (Germanischer Lloyd 2015)

Provided by previous GL, an internal complete report (Germanischer Lloyd 2005) for strength investigations of a 9000 TEU containership is the basis for the following calculation. All calculation was carried out using GL classification standard (Germanischer Lloyd 2015).

It was consider a plate located at amidships made of YP40 material (yield stress, $R_{eH} = 390$ N/mm²) with thickness of 80mm, FAT class 125 (it was considered for the sake of the simulation) and usage factor⁷ of 0.93. Two different maximum stress amplitudes are

⁷ Ratio of evaluated to allowable stress amplitude.

established in the report: Allowable Stress of 276 N/mm², which can provide the maximum stress range according to Eq. (34); and the FE-Calculated Stress of 257 N/mm².

$$\Delta\sigma_{max} = 2 \cdot \sigma_a = 2 \cdot 276 = 552 \text{ N/mm}^2 \quad (34)$$

Permissible stress range for standard stress range spectra ($\Delta\sigma_p$) is calculated from the formulation (Germanischer Lloyd 2015):

$$\Delta\sigma_p = f_n \cdot \Delta\sigma_{Rc} \quad (35)$$

where the peak stress range of the spectrum is not exceed the permissible $\Delta\sigma_{max} \leq \Delta\sigma_p$

$$\Delta\sigma_p = \Delta\sigma_{max} = 552 \text{ N/mm}^2 \quad (36)$$

and f_n factor for the determination of the permissible stress range for standard stress for Type E3 ($m_0 = 3.5$) is 3.65 according to detail category from Figure 70 and $n_{max} = 5 \cdot 10^7$ for stress range spectrum A from Table 20.2 (Germanischer Lloyd 2015) from Figure 71.

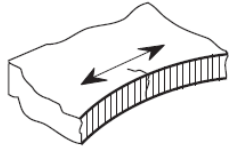
E3		Plate edge not meeting the requirements of type E2, but free from cracks and severe notches.	
		Machine cut or sheared edge:	125 ($m_0 = 3.5$)
		Manually thermally cut:	100 ($m_0 = 3.5$)
		Stress increase due to geometry of cut-outs to be considered. ¹	

Figure 70 – Part of Catalogue of Details for Unwelded Base Materials and f_n Factor (Germanischer Lloyd 2015)

Stress range spectrum	Welded Joints					Plates Edges																											
	$(m_0 = 3)$					Type E1 ($m_0 = 5$)					Type E2, E2a ($m_0 = 4$)					Type E3 ($m_0 = 3.5$)																	
	$n_{max} =$					$n_{max} =$					$n_{max} =$					$n_{max} =$																	
	10^3	10^5	$5 \cdot 10^7$	10^8	$3 \cdot 10^8$	10^3	10^5	$5 \cdot 10^7$	10^8	$3 \cdot 10^8$	10^3	10^5	$5 \cdot 10^7$	10^8	$3 \cdot 10^8$	10^3	10^5	$5 \cdot 10^7$	10^8	$3 \cdot 10^8$													
A		(17.2)	3.53	3.02	2.39		(8.1)	3.63	3.32	2.89		(8.63)										(10.3)					(12.2) ²	3.65 ¹	3.19	2.62			
B		(9.2)	1.67	1.43	1.15		(9.5)	5.0	1.95	1.78	1.55		(10.30)	5.50										6.6				7.5 ²		1.78	1.55	1.28	
C	(12.6)	2.71	0.424	0.369	0.296		(4.57)	1.82	0.606	0.561	0.500		(4.57)	1.82	0.532	0.482	0.411		(4.57)	1.82	0.587 ¹	0.569 ¹	0.541 ¹		0.621 ¹	0.602 ¹	0.573 ¹						

Figure 71 – Part of Factor f_n Table (Germanischer Lloyd 2015)

From the FE calculated stress and based on GL Rules (Germanischer Lloyd 2015), the main idea is to do a reserve calculation in order to obtain the parameters to simulate crack propagation under variable loads in the software *Fraunhofer IWM Verb*, such as stress range and mean stress or maximum and minimum stresses.

Following formulation is also provided in order to calculate the corrected fatigue strength reference value of S-N curve at $2 \cdot 10^6$ cycles of stress range in N/mm^2 ($\Delta\sigma_{Rc}$):

$$\Delta\sigma_{Rc} = f_m \cdot f_R \cdot f_W \cdot f_i \cdot f_t \cdot \Delta\sigma_R \quad (37)$$

or for permissible stress range:

$$\Delta\sigma_p = f_n \cdot \Delta\sigma_{Rc} = f_n \cdot f_m \cdot f_R \cdot f_W \cdot f_i \cdot f_t \cdot \Delta\sigma_R \quad (38)$$

with factor f_n as 3.65 and material effect (f_m) as stated in Eq. (31) and calculated as:

$$f_m = 1 + \frac{R_{eH} - 235}{1200} = 1 + \frac{390 - 235}{1200} \approx 1.13 \quad (39)$$

continuing with effect of weld shape (f_W) taken as 1; influence of importance of structural element (f_i) is according to the below formulation:

$$f_i = 0.9 + 5/r \leq 1.0 \quad \therefore f_i = 0.9 + 5/400 \approx 0.91 \quad (40)$$

taken the value of notch radius 400mm from Germanischer Lloyd (2005); plate thickness effect (f_t) for free edges is 1; and detail stress range (DSR) - $\Delta\sigma_R$ equals to 125 N/mm^2 .

Effect of mean stress (f_R) considering range of alternating stress can be calculated by manipulating Eq. (38), such as:

$$f_R = \frac{\Delta\sigma_p}{f_n \cdot f_m \cdot f_W \cdot f_i \cdot f_t \cdot \Delta\sigma_R} = \frac{552}{3.65 \cdot 1.13 \cdot 1 \cdot 0.91 \cdot 1 \cdot 125} \approx 1.17 \quad (41)$$

$$f_R = 1 + c \cdot \left(1 - \frac{2 \cdot \sigma_m}{\Delta\sigma_{max}} \right) = 1.17 \quad (42)$$

with coefficient c as 0.30 for unwelded base materials, one can achieve the mean stress (σ_m):

$$\sigma_m = 115.73 N/mm^2 \quad (43)$$

From mean stress ($\Delta\sigma_m$) and permissible stress range ($\Delta\sigma_p$), one can calculate the values of minimum ($\Delta\sigma_{min}$) and maximum ($\Delta\sigma_{max}$) stress and stress ratio (R):

$$\sigma_{min} = \left(\frac{2 \cdot \sigma_m - \Delta\sigma_p}{2} \right) = -160 N/mm^2 \quad (44)$$

$$\sigma_{max} = \Delta\sigma_p + \sigma_{min} = 392 N/mm^2 \quad (45)$$

$$R = -0.4 \quad (46)$$

A summary with all needed stress data is provided in Figure 72.

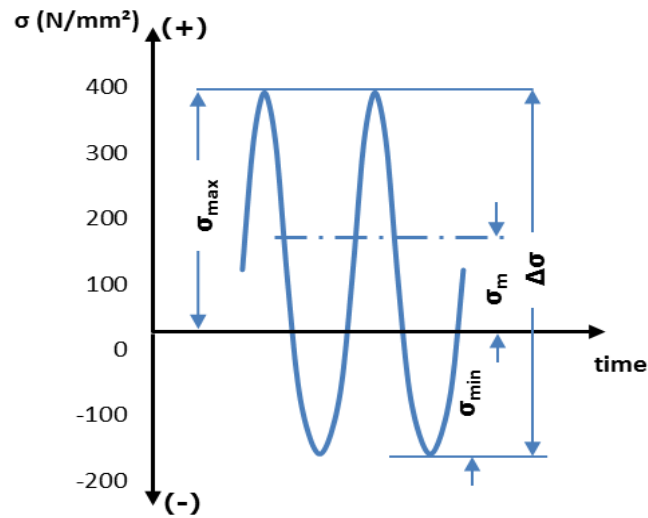


Figure 72 – Graphical Summary of Variable Stress Values

Three different crack models are adopted to perform only axial load simulation: extended surface crack, semi-elliptical crack and quarter corner elliptical crack, which are the main shapes of cracks occurring in thermal cut surfaces.

When the crack propagates over all thickness dimensions for any of the surface elliptical crack model, through thickness crack is used to continue the crack propagation on the other considered dimension, width of the plate with 500mm size.

4.7.1 Crack Propagation for Quarter Corner Crack under Variable Load

Figure 73 shows the results for quarter corner crack under variable loads for distinct initial crack sizes with crack aspect ratio of 2 (a_0/c_0). It is verified that under small values of crack depth and crack length e.g. 4mm and 8mm, respectively, small crack growth can be observed and design lifetime is still valid.

When initial crack sizes are increased, influence on lifetime can be verified accordingly. For $a_0 = 6\text{mm}$ and $c_0 = 12\text{mm}$, lifetime of around 17 years is achieved in a conservative view and slightly more number of cycles are added when considering that through-thickness crack model can still represent the remaining life.

Special attention has to be given when further initial crack is increased, since smaller lifetime is established. Maintenance is needed in any case, however when initial cracks are bigger than certain values, such as $a_0 = 10\text{mm}$ and $c_0 = 20\text{mm}$, less than 5 year of lifetime is achieved which is time for drydock or overall inspection. With such small lifetime, it is costly and dangerous to the vessel if a structural damage occurs.

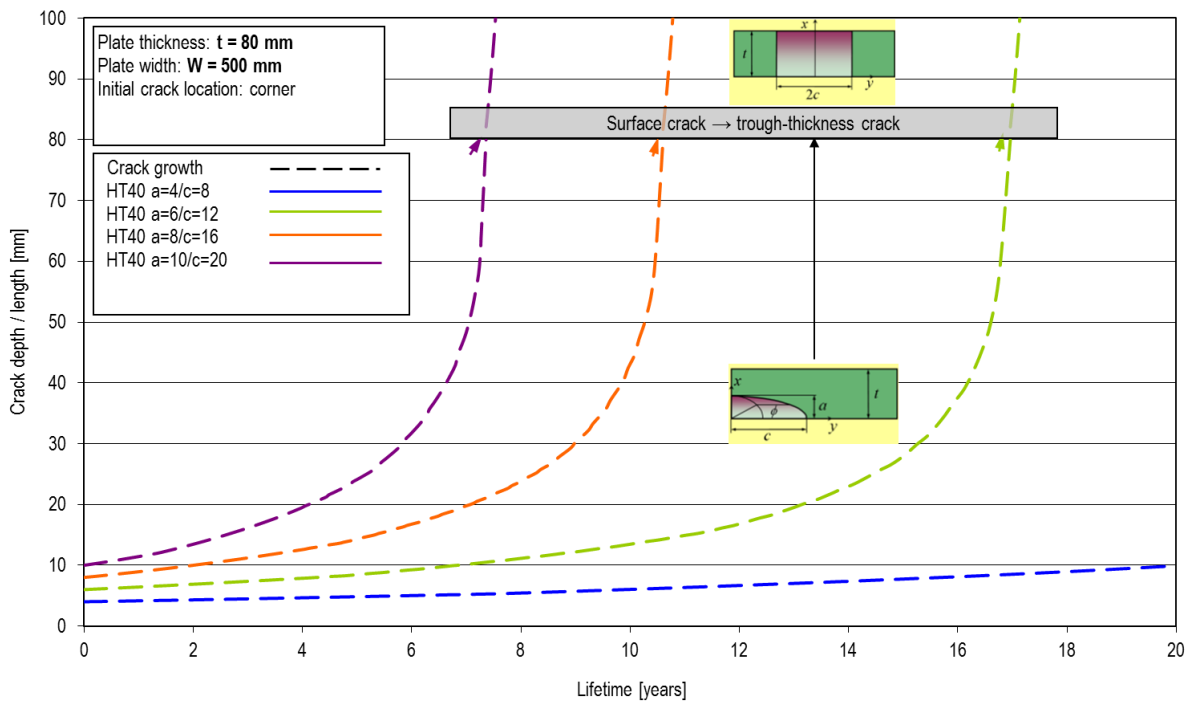


Figure 73 – Crack Propagation for Quarter Corner Crack under Variable Load

4.7.2 Crack Propagation for Semi-Elliptical Crack under Variable Load

For semi-elliptical crack model considering the same initial crack sizes as quarter corner crack model, Figure 74 provides less severe results when compared with Figure 73. Nevertheless, same considerations are made for semi-elliptical.

Under crack sizes of $a_0 = 6\text{mm}$ and $c_0 = 12\text{mm}$, cracks does not represent an extreme dangerous issue, however for higher initial crack sizes, one should pay attention, especially when crack depth is finished and abrupt crack growth can be seen when changing the model to through-thickness.

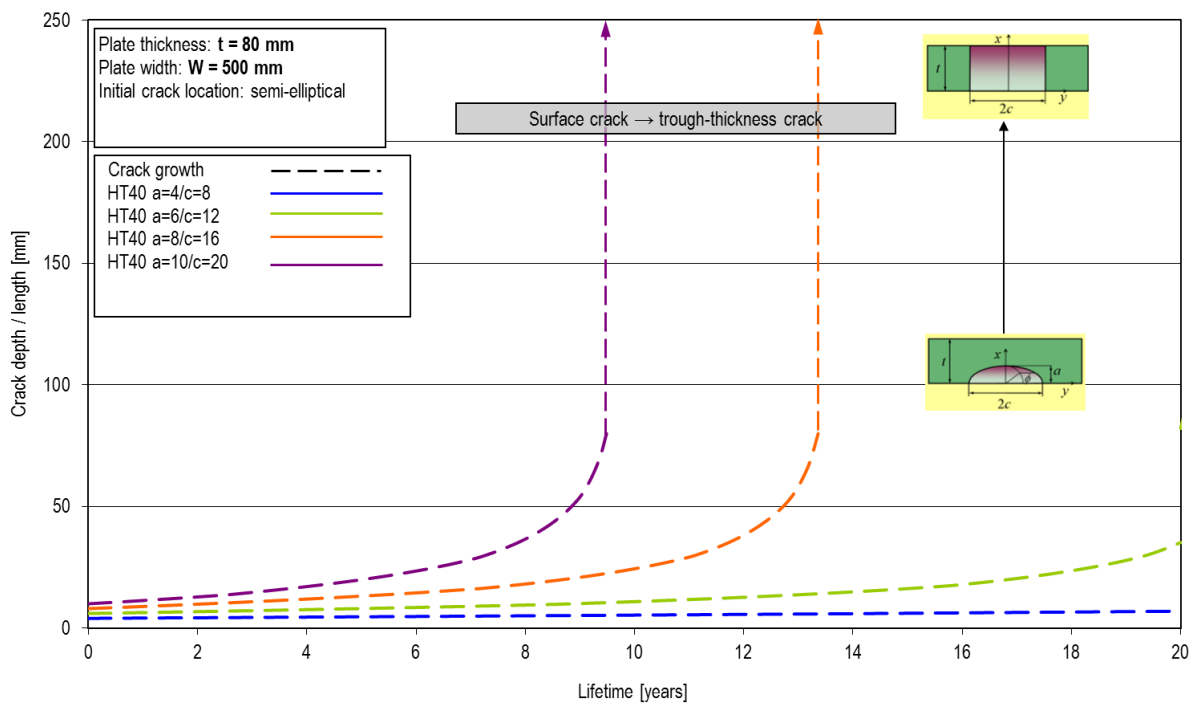


Figure 74 – Crack Propagation for Semi-Elliptical Crack under Variable Load

4.7.3 Crack Propagation for Extended Surface Crack under Variable Load

In some cases, small extended surface can be verified on real case scenarios. When compared to quarter corner crack (Figure 73) and semi-elliptical cracks (Figure 74), smaller crack depth (a) can result in very short lifetime. Values bigger than $a_0 = 1.5\text{mm}$ can provide crack propagation with less lifetime than 20 years where vessels are usually designed. When increasing the crack depth, much smaller lifetime is achieved and dangerous situation may occur. Short period for inspection should be considered and followed by maintenance.

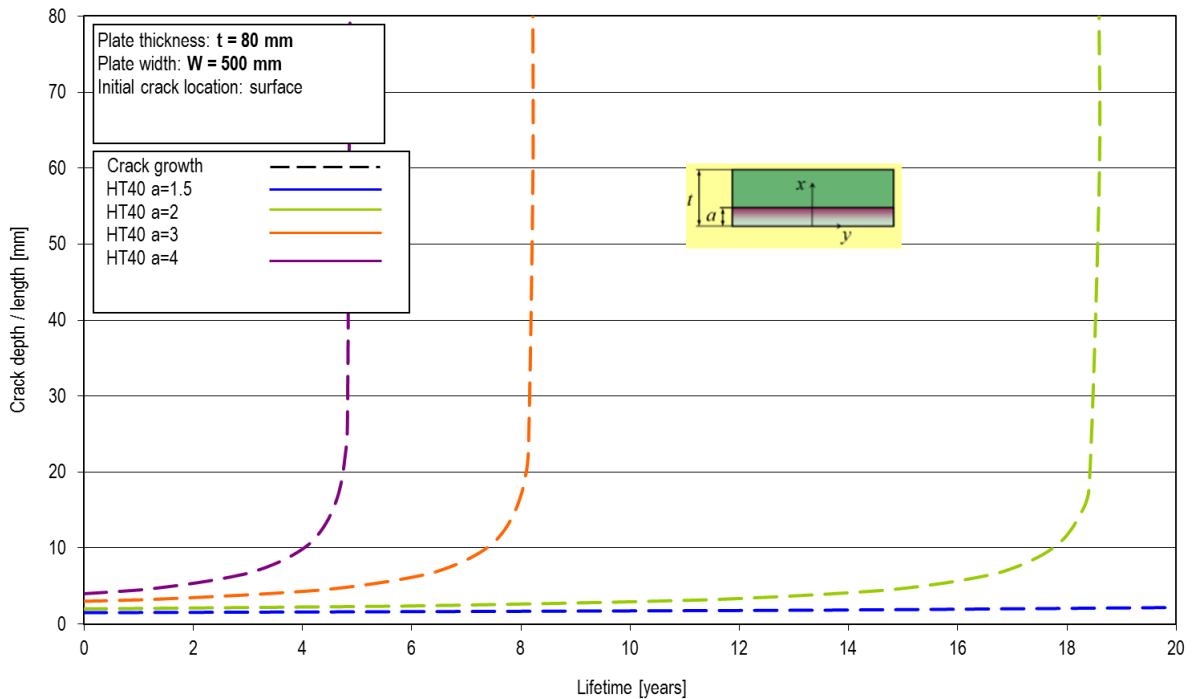


Figure 75 – Crack Propagation for Extended Surface Crack under Variable Load

5. CONCLUSION

In this work, fatigue and fracture assessment for butt welded joints with internal defects and thermal cut edges under axial and bending loads are performed, including for the latter the influence of edge treatments, crack models, initial crack sizes and investigation of variable loads on a real case scenario.

Regarding butt welded joint with lack of fusion, embedded elliptical crack model with same area of actual internal lack of fusion can represent the expected life of the specimen. Parameters from IIW2008 are more conservative than DNV GL lab tests parameters. Higher fatigue life is verified under pure bending load compared to pure axial load. However, deeper research on fatigue enhancement due to bending needs to be carried out for different types of defects, in this case internal lack of fusion.

For thermal cut edges, influence on stress concentration factors due to edge treatments can be neglected. In service fatigue improvement can be explained by the fact that with edge treatment any impact on the plate cut surface will be less severe than compared with sharp edge, leading more easily to surface cracks. Quarter elliptical corner crack presents less lifetime when compared to semi elliptical crack model, thus a crack with corner crack shape is more severe than semi elliptical surface crack shape. Higher thickness provides higher fatigue life when considering same material and crack model. Regarding higher tensile material fatigue strength improvement, it is necessary to investigate base materials parameters in more details, for instance YP47. Fatigue strength enhancements due to pure bending are in the range between 5% to 15%, depending on the thickness, crack shape and material properties.

Lastly for thermal cut edges, evaluation of variable loads with respect to design lifetime is highly dependent on the adopted crack model, initial crack size and the inspection/maintenance are thus influenced by initial crack investigation and stresses applied.

Extended surface cracks are dangerous even for small crack sizes and in case of such cracks attention should be paid in early stage. Quarter corner crack follows with also a need to inspection for crack sizes which can lead to small lifetime. Semi-elliptical crack are less severe than quarter corner cracks. For both last cases, just a few additional lifetime is provided after finishing the thickness dimension and changing the model to through thickness, therefore this additional number of cycles are neglected keeping a conservative analysis.

More future recommendation can be established, such as investigation on surface roughness influence on fatigue life for different thermal cutting techniques, thickness and materials.

6. ACKNOWLEDGEMENTS

This thesis was developed in the frame of the European Master Course in “Integrated Advanced Ship Design” named “EMSHIP” for “European Education in Advanced Ship Design”, Ref.: 159652-1-2009-1-BE-ERA MUNDUS-EMMC.

I would like to express my gratitude to all DNV GL staff from Hamburg Research and Development Department in Germany, where I did my internship and most of my research. Every needed support was provided during the time I have spent in DNV GL.

Many thanks especially to my internship supervisor, Dr. Hubertus von Selle, a great professional who has turned this challenge into something pleasant with his guidance, remarks, useful comments and engagement through the learning process of this work.

Special thanks to my supervisor Prof. Kaeding from University of Rostock and all my friends from EMShip 5th Cohort.

From the bottom of my heart, this work goes to my beloved ones for their encouragement during this entire journey. To my family, I really appreciate your support and good vibrations. To my lovely wife, infinite thanks for her unconditional support and for being the angel always by my side. God bless you all. Best Regards.

7. REFERENCES

- AcelorMittal (2015): Guidelines for Fabricating and Processing Plate Steel. AcelorMittal USA, Plate Production Facilities. Available online at <http://usa.arcelormittal.com/What-we-do/Steel-products/Plate/>.
- Altena, E. (2013): Optimization of modal shift and container (re-)positioning at Maersk Line. Master Thesis. Delft University of Technology.
- American Institute of Welding (2010): AWS A3.0M/A3.0:2010 - Standard Welding Terms and Definitions. American Institute of Welding - IIW.
- Ashar, A. and Rodrigue, J.-P. (2012): The Geography of Transport Systems. Chapter 3 - Transportation Modes. Hofstra University, New York, USA. Available online at <http://people.hofstra.edu/geotrans/eng/ch3en/conc3en/containerships.html>.
- Battelle Columbus Laboratories (1983): Improved prevention techniques could save \$60 billion of US fracture costs says report to Congress. In *NDT International* 16 (3), pp. 159–160.
- Beer, F. P.; Johnston Jr., E. R., DeWolf, J. T. and Mazurek, D. F. (2014): Mechanics of Materials. 7th ed.: McGraw-Hill Education.
- Berger, C.; Blauel, J. G.; Hodulak, L.; Pyttel, B. and Varfolomeyev, I. (2009): FKM - Guideline Fracture Mechanics Proof of Strength.
- Berglund, J. (2006): Cut Cost Calculation. Master Thesis. Lulea University of Technology.
- Bezensek, B.; Sharples, J.; Hadley, I. and Pisarski, H. (2011): The History of BS 6910 Flaw Interaction Criteria. Paper No. PVP2011-57857. In *ASME 2011 Pressure Vessels and Piping Conference Volume 1: Codes and Standards*, pp. 837–843.
- British Standard Institute (1995): BS 7608:1993 Code of Practice for Fatigue Design and Assessment of Steel Structures. Incorporating Amendment No. 1. In *BSI, London*.
- British Standard Institute (1999): BS 7910:1999 Guide on Methods for Assessing the Acceptability of Flaws in Metallic Structures. In *BSI, London*.
- British Standard Institute (2014): BS 7608:2014 Guide for fatigue design and assessment of steel products. In *BSI, London*.
- Brooks, M. R.; Pallis, T. and Perkins, S. (2013): Port Investment and Container Ship Markets - Roundtable Summary and Conclusions. Discussion Paper. In *International Transport Forum* 2014/3.
- BV Korea Marine (2014): Container Ships Evolution. M&O Seminar Chantilly – NC1.a – Challenges due to Size of Container Ships and ULC Ships. Presentation in ppt format. Bureau Veritas.
- Castillo, J. E. (1991): Mathematical aspects of numerical grid generation: Society for Industrial and Applied Mathematics.
- Chakarov, K.; Garbatov, Y. and Soares, C. G. (2008): Fatigue Analysis of Ship Deck Structure Accounting for Imperfections. In *International Journal of Fatigue* 30, pp. 1881–1897.
- Cudahy, B. J. (2006): The Containership Revolution Malcom McLean's 1956 Innovation Goes Global. World Shipping Council.

- DIN (2003): DIN 2310-6 Thermal Cutting – Part 6: Classification, Processes. DIN.
- DNV (2014): Fatigue Assessment of Ship Structures. Classification Notes. No. 30.7. DNV.
- DNV GL (2015): Joint Development Project – Fatigue Characterization of YP47 Welds. Internal Report. Not Published.
- Doerk, O.; Shin, S.-B. and An, G.-B. (2014): Design Impact of Fracture Mechanics Properties of High Toughness YP47 Welds. International Society of Offshore and Polar Engineers (ISOPE), Busan. In *Proceedings of the Twenty-fourth International Ocean and Polar Engineering Conference*.
- Doerk, O. and Rörup, J. (2009): Development of toughness and quality requirements for YP47 steel welds based on fracture mechanics. In *The Nineteenth International Offshore and Polar Engineering Conference, International Society of Offshore and Polar Engineers (ISOPE), Osaka*.
- Farahmand, B. (2001): Fracture Mechanics of Metals, Composites, Welds, and Bolted Joints: Application of LEFM, EPFM, and FMDM Theory: Kluwer Academic Publishers.
- Fraunhofer (2008a): VERB: Failure Assessment Software Version 8.0 - Compendium of Stress Intensity Factor and Limit Load Solutions. In *Fraunhofer IWM Version 8.0*.
- Fraunhofer (2008b): VERB: Failure Assessment Software Version 8.0 - User's Guide. In *Fraunhofer IWM Version 8.0*.
- Fricke, W.; Cui, W.; Kierkegaard, H.; Kihl, D.; Koval, M.; Mikkola, T. et al. (2002): Comparative fatigue strength assessment of a structural detail in a containership using various approaches of classification societies. In *Marine Structures* 15, pp. 1–13.
- Fricke, W.; Petershagen, H. and Paetzold, H. (1998a): Fatigue strength of ship structures. Part I. Basic Principles. Hamburg: Germanischer Lloyd Aktiengesellschaft (GL-technology, no. 1/97).
- Fricke, W.; Petershagen, H. and Paetzold, H. (1998b): Fatigue strength of ship structures. Part II. Examples. Hamburg: Germanischer Lloyd Aktiengesellschaft (GL-technology, no. 1/98).
- Fricke, W. and Paetzold, H. (2012): Fatigue Strength of Butt Weld Specimens with Lack of Fusion. DNV GL Internal Only. In *Report from Institute for Ship Structural Design and Analysis (M10)*.
- Germanischer Lloyd (2005): Internal Report for Conversion of a Containership. Department Strength/ESS.
- Germanischer Lloyd (2011): Guidelines for Global Strength Analysis of Container Ships. Rules for Classification and Construction. GL.
- Germanischer Lloyd (2015): Germanischer Lloyd Rules for Classification and Construction I Ship Technology 1 Seagoing Ships 5 Structural Rules for Container Ships. Section 20 Fatigue Strength.
- Goldberg, F. (1973): Influence of Thermal Cutting and Its Quality on the Fatigue Strength of Steel. Welding Research Supplement. In *Welding Journal* 52 (9), pp. 392–404.
- Haagensen, P. J. and Maddox, S. J. (2013): IIW Recommendations on Methods for Improving the Fatigue Strength of Welded Joints. IIW-2142-10. In *International Institute of Welding*.
- Hebhardt, C. (2011): Praxisbuch FEM mit ANSYS Workbench Einführung in die Lineare und Nichtlineare Mechanik: Carl Hanser Verlag München.

- Hertzberg, R. (1996): *Deformation and Fracture Mechanics of Engineering Materials*. New York: John Wiley and Sons.
- Hobbacher, A. (2008): *Recommendations for Fatigue Design of Welded Joints and Components XIII-2151r4-07/XV-1254r4-07*. International Institute of Welding: IIW.
- IACS (2013a): *S33 Requirements for Use of Extremely Thick Steel Plates*. IACS Requirements. International Association of Classification Societies Ltd.
- IACS (2013b): *W31 Application of YP47 Steel Plates*. Requeriments. International Association of Classification Societies Ltd.
- ISF Welding and Joining Institute (2005): *Chapter 12 - Thermal Cutting*. RWTH Aachen University. Available online at <https://www.isf.rwth-aachen.de/>.
- Jonsson, B. (2015): *Cut Sections/Edges: Connection of ISO 9013 to Fatigue*. Not Published. Helsinki, Finland: XIII / WG4 Annual Meeting.
- Laitinen, R.; Valkonen, I. and Kömi, J. (2013): *Influence of the base material strength and edge preparation on the fatigue strength of the structures made by high and ultra-high strength steels*. In *Procedia Engineering* 66, pp. 282–291.
- Lassen, T. and Récho, N. (2006): *Fatigue and Life Analyses of Welded Structures*. 1st ed.: Woodhead Publishing Limited.
- Lee, H.-H. (2014): *Finite Element Simulations with ANSYS Workbench 15 Theory, Applications, Case Studies*: SDC Publications.
- Li, G. and Wu, Y. (2010): *A Study of the Thickness Effect in Fatigue Design Using the Hot Spot Stress Method*. Master Thesis. Chalmers University of Technology.
- Lotsberg, I. (2014): *Assessment of the size effect for use in design standards for fatigue analysis*. In *International Journal of Fatigue* 66, pp. 86–100.
- Maddox, S. J. (2003): *Review of Fatigue Assessment Procedures for Welded Aluminium Structures*. In *International Journal of Fatigue* 25 (12), pp. 1359–1378.
- Maddox, S. J. (2015): *Allowance for bending in fatigue design rules for welded joints*. XIII-2580-15. In *International Institute of Welding*.
- MarineLink.com (2008): *Guidelines - YP47 Steel for Hull Structures*. Available online at <http://www.marinelink.com/news/article/guidelines-yp47-steel-for-hull-structures/328523.aspx>.
- Montes, C. P.; Seoane, M. J. F. and Laxe, F. G. (2012): *General cargo and containership emergent routes: A complex networks description*. In *Transport Policy* 24, pp. 126–140.
- Moore, P.; Booch, G. (2015): *The Welding Engineer's Guide to Fracture and Fatigue*. 1st ed.: Woodhead Publishing Elsevier Ltd. (227).
- Moore, P. and Booth, G. (2015): *The Welding Engineer's Guide to Fracture and Fatigue*. Cambridge, UK, Waltham, MA, USA: Elsevier Woodhead Publishing (Woodhead Publishing series in welding and other joining technologies, number 84).
- Moraitis, G. (2014): *Fatigue and Fracture Assessment of Butt Welds*. Master Thesis. West Pomeranian University of Technology.
- National Corrosion Service (1983): *Fracture costs US industry \$119 000 million every year*. In *International Journal of Fatigue* 5 (3), p. 176.

- Nordson DAGE (2011): 3 and 4 Point Flexural Testing. Application Note. Nordson DAGE. Available online at <http://www.nordson.com/>.
- Pedersen, M. M.; Andersen, J. G. and Ólafsson, Ó. M. (2012): Investigation of the Thickness Effect for Butt Welded Joints. Danish Delegation C-XIII-WG1: IIW.
- Pilkey, W. D. (1997): Peterson's Stress Concentration Factors. 2nd ed.: John Wiley & Sons, Inc. New York.
- Radaj, D.; Sonsino, C. M. and Fricke, W. (2006): Fatigue Assessment of Welded Joints by Local Approaches. 2nd ed. Cambridge, England: Woodhead.
- Remes, H.; Korhonen, E.; Lehto, P.; Romanoff, J.; Niemelä, A.; Hiltunen, P. and Kontkanen, T. (2013): Influence of surface integrity on the fatigue strength of high-strength steels. In *Journal of Constructional Steel Research* Vol. 89, pp. 21–29.
- Rigo, P. and Rizzutto, E. (2003): Ship Design and Construction. Chapter 18. Analysis and Design of Ship Structure. 1 volume: SNAME.
- Rizvi, Z. H. (2011): The containership - how big: What are the prospects for MalaccaMax? Container Handling, Container Handling/Terminal Logistics. Port Technology. Available online at https://www.porttechnology.org/images/uploads/technical_papers/PT40-05.pdf.
- Roylance, D. (2001): Fatigue. Module Yield and Fracture. Lecture Notes - MITOPENCOURSEWARE. Massachusetts Institute of Technology. Available online at <http://ocw.mit.edu/courses/materials-science-and-engineering/3-11-mechanics-of-materials-fall-1999/modules/fatigue.pdf>.
- Ruukki Metals Oy (2011): Hot-Rolled Steel Plates, Sheets and Coils – Thermal Cutting and Flame Straightening. Datasheet. Ruukki Metals Oy. Available online at www.ruukki.com.
- Selle, H. von (2014): Recent Fatigue and Fracture Research Activities. Brochure.
- Selle, H. von; Doerk, O.; Kangand, J. K. and Kim, J. H. (2011): Fatigue tests of butt welds and plates edges of 80 mm thick plates. In *Advances in Marine Structures*, pp. 511–519.
- Selle, H. von; Doerk, O. and Scharrer, M. (2009): Chapter 29. Global strength analysis of ships with special focus on fatigue of hatch corners. Analysis and Design of Marine Structures including CD-ROM. In *CRC Press*, pp. 255–260.
- VDI 3258 Blatt 2 (1964): Cost Accounting with Machine Hour Rates; Explanations and Examples. Verein Deutscher Ingenieure.

APPENDIX A – CHAPTER 3

Fraunhofer IWM Verb Crack Models (Fraunhofer 2008a, 2008b)

3.1 Extended surface crack

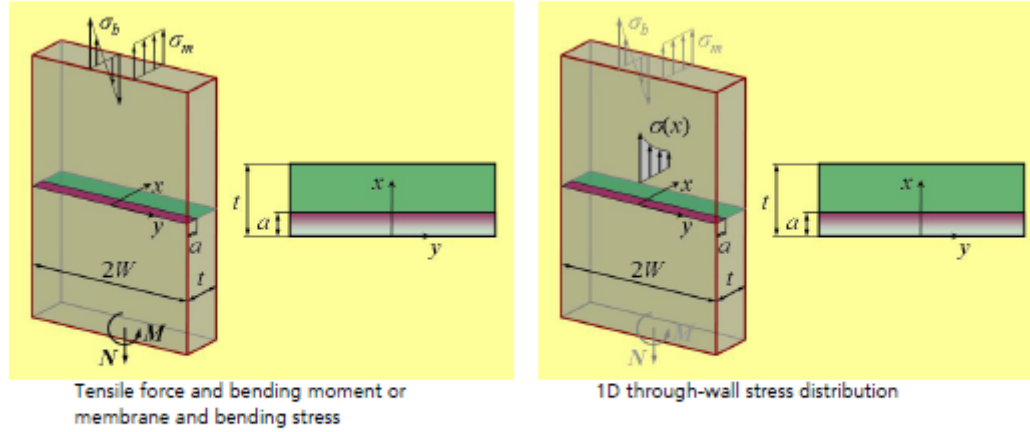


Fig. 3.1 Extended surface crack in a plate

Stress intensity factor, K_I

Solution	Reference	Validity range	Loading	Error	Default	Usage in FAP
1	[10]	$a/t \leq 0.9$	1D stress field	< 1%	•	FKM
2	[23]	$a/t \leq 0.8$	1D stress field	< 3%	-	-
3	[4]	$a/t \leq 0.5$	1D stress field	< 3%	-	-

Limit load parameter, L_r

Solution	Reference	Validity range	Loading	Default	Usage in FAP
1	[32]	$a/t \leq 0.8$	membrane and bending stress; linearization of 1D stress field	•	DNV, FKM, SINTAP

3.1.1 Stress intensity factor

Solution 1

Solution method: weight function [10].

$$K = \int_0^a \sigma(x) h(x, a) dx$$

$$h = \sqrt{\frac{2}{\pi a}} \left(1 - \frac{x}{a}\right)^{\frac{1}{2}} \left[1 + \sum_{n=0}^2 \sum_{m=0}^4 \frac{A_{nm} \xi^m}{(1-\xi)^{3/2}} \left(1 - \frac{x}{a}\right)^{n+1} \right] \quad (3.1)$$

$$\xi = \frac{a}{t}$$

The coefficients A_{mn} are listed in Table 3.2.

Table 3.2 Approximating coefficients A_{mn} in the weight function, Eq. (3.1)

	$m = 0$	$m = 1$	$m = 2$	$m = 3$	$m = 4$
$n = 0$	0.4980	2.4463	0.0700	1.3187	-3.0670
$n = 1$	0.5416	-5.0806	24.3447	-32.7208	18.1214
$n = 2$	-0.19277	2.55863	-12.6415	19.7630	-10.9860

Solution 2

Solution method: weight function for a hollow cylinder with a complete circumferential crack at the outer surface [23], Section 5.1.2, is used. The solution for a plate is deduced by setting

$$\lambda = \frac{t}{R_i} = 0$$

in Eqs (5.1)-(5.5), (5.9).

Solution 3

Solution method: weight function [4].

$$\begin{aligned}
 K &= \int_0^a \sigma(x)h(x, a)dx \\
 h &= \sqrt{\frac{2}{\pi a}} \left(1 - \frac{x}{a}\right)^{\frac{1}{2}} \left[1 + m_1 \left(1 - \frac{x}{a}\right) + m_2 \left(1 - \frac{x}{a}\right)^2 \right] \\
 m_1 &= 0.6147 + 17.1844 \left(\frac{a}{t}\right)^2 + 8.7822 \left(\frac{a}{t}\right)^6 \\
 m_2 &= 0.2502 + 3.2889 \left(\frac{a}{t}\right)^2 + 70.0444 \left(\frac{a}{t}\right)^6
 \end{aligned}
 \tag{3.2}$$

3.1.2 Limit load parameter

Solution 1

Solution is given in [32]:

$$\begin{aligned}
 L_r &= \frac{\xi \sigma_{mL} + \frac{\sigma_{bL}}{3} + \sqrt{\left(\xi \sigma_{mL} + \frac{\sigma_{bL}}{3}\right)^2 + (1 - \xi)^2 \sigma_{mL}^2}}{(1 - \xi)^2 R_e} \\
 \xi &= \frac{a}{t}
 \end{aligned}
 \tag{3.3}$$

3.3 Semi-elliptical surface crack in a plate

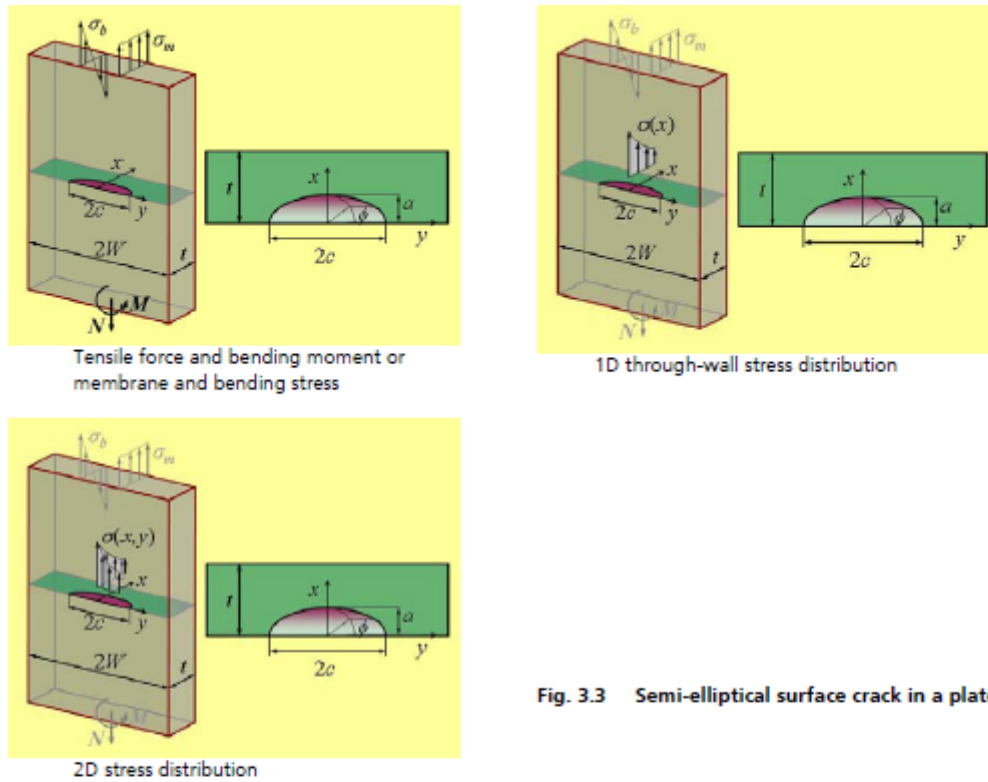


Fig. 3.3 Semi-elliptical surface crack in a plate

Stress intensity factor, K_I

Solution	Reference	Validity range	Loading	Error	Default	Usage in FAP
1	[26]	$a/t \leq 0.9, 0.1 \leq a/c \leq 1.5, c/W \leq 0.5, 0^\circ \leq \phi \leq 180^\circ$	2D stress field	< 5%	-	-
2	[8]	$a/t \leq 0.8, 0 \leq a/c \leq 1, c/W \leq 0.5, \phi = 0^\circ, 90^\circ$	1D stress field	< 5%	-	-
3	[31]	$a/t \leq 0.8, 0 \leq a/c \leq 1, c/W \leq 0.5, \phi = 0^\circ, 90^\circ$	1D stress field	< 5%	•	FKM
4	[18]	$a/t \leq 1, 0 \leq a/c \leq 2, c/W \leq 0.5, 0^\circ \leq \phi \leq 180^\circ$	membrane and bending stress	< 5%		FKM

Limit load parameter, L_r

Solution	Reference	Validity range	Loading	Default	Usage in FAP
1	[19]	$a/t \leq 0.8$	membrane and bending stress; linearization of the stress field	•	DNV, FKM
2	[16]	$a/t \leq 0.8$	membrane and bending stress; linearization of the stress field	-	-
3	[32]	$a/t \leq 0.8$	membrane and bending stress; linearization of the stress field	-	API 579

3.3.1 Stress intensity factor

Solution 1

Solution method: polynomial influence functions based of finite-element analyses [26].

The stress field in the crack plane is considered to be a 2D function of the coordinates x and y , as given by Eq. (2.9), with $m_{\max} = n_{\max} = 4$. Only even functions of the coordinate y , are involved. The influence functions f_{mn} were numerically derived in [26] for polynomial type loading

$$\sigma_{mn} = \left(\frac{x}{a}\right)^m \left|\frac{y}{c}\right|^n, \quad (3.6)$$

assuming a wide plate with

$$2W = \max(12t, 12c).$$

The stress intensity factor at an arbitrary point on the crack front is then calculated by

$$K\left(\frac{a}{c}, \frac{a}{t}, \frac{c}{W}, \phi\right) = \left[\sum_{m=0}^4 \sum_{n=0}^4 D_{mn} f_{mn}\left(\frac{a}{c}, \frac{a}{t}, \phi\right) \left(\frac{a}{t}\right)^{m+n} \left(\frac{a}{c}\right)^{-n} \right] \sqrt{\frac{\pi a}{Q}} f_w\left(\frac{c}{W}, \frac{a}{t}\right). \quad (3.7)$$

Here

$$\begin{aligned} Q &= 1 + 1.464(a/c)^{1.65}, \quad a/c \leq 1 \\ Q &= 1 + 1.464(c/a)^{1.65}, \quad a/c > 1 \end{aligned} \quad (3.8)$$

and the finite width correction is assumed according to [18]:

$$f_w = \left[\sec\left(\frac{\pi c}{2W} \sqrt{\frac{a}{t}}\right) \right]^{\frac{1}{2}}. \quad (3.9)$$

Solution 2

Solution method: polynomial influence functions based of finite-element analyses [8].

The stress field in the crack plane is considered as a 1D function of the coordinate x , Eq. (2.12), with $m_{\max} = 3$. The influence functions f_m are tabulated in [8] for polynomial type loading

$$\sigma_{mn} = \left(\frac{x}{a}\right)^m,$$

assuming a wide plate with

$$2W = \max(20t, 16c).$$

The stress intensity factor at an arbitrary point on the crack front is then calculated by

$$K\left(\frac{a}{c}, \frac{a}{t}, \frac{c}{W}, \phi\right) = \left[\sum_{m=0}^3 D_m f_m\left(\frac{a}{c}, \frac{a}{t}, \phi\right) \left(\frac{a}{t}\right)^m \right] \sqrt{\pi a} f_w\left(\frac{c}{W}, \frac{a}{t}\right). \quad (3.10)$$

The finite width correction [18], Eq. (3.9), is additionally employed.

Solution 3

Solution method: weight function [31].

The stress intensity factor is calculated for an arbitrary 1D stress distribution, Eq. (2.14), at the surface point ($\phi = 0^\circ$, subscript *C*) and the deepest point (crack centre, $\phi = 90^\circ$, subscript *A*) of the crack front:

$$\begin{aligned} K(\phi = 90^\circ) &= \int_0^a \sigma(x) h_A(x, a) dx \\ K(\phi = 0^\circ) &= \int_0^a \sigma(x) h_C(x, a) dx \end{aligned} \quad (3.11)$$

$$h_A(x, a) = \frac{2}{\sqrt{2\pi(a-x)}} \left[1 + M_{1A} \left(1 - \frac{x}{a}\right)^{\frac{1}{2}} + M_{2A} \left(1 - \frac{x}{a}\right) + M_{3A} \left(1 - \frac{x}{a}\right)^{\frac{3}{2}} \right]$$

$$h_C(x, a) = \frac{2}{\sqrt{2\pi x}} \left[1 + M_{1C} \left(\frac{x}{a}\right)^{\frac{1}{2}} + M_{2C} \left(\frac{x}{a}\right) + M_{3C} \left(\frac{x}{a}\right)^{\frac{3}{2}} \right]$$

$$M_{1A} = \frac{\pi}{\sqrt{2Q}} (4Y_0 - 6Y_1) - \frac{24}{5}, \quad M_{2A} = 3, \quad M_{3A} = 2 \left(\frac{\pi}{\sqrt{2Q}} Y_0 - M_{1A} - 4 \right)$$

$$Y_0 = B_0 + B_1 \left(\frac{a}{t}\right)^2 + B_2 \left(\frac{a}{t}\right)^4, \quad Y_1 = A_0 + A_1 \left(\frac{a}{t}\right)^2 + A_2 \left(\frac{a}{t}\right)^4$$

$$B_0 = 1.10190 - 0.019863 \left(\frac{a}{c}\right) - 0.043588 \left(\frac{a}{c}\right)^2$$

$$B_1 = 4.32489 - 14.9372 \left(\frac{a}{c}\right) + 19.4389 \left(\frac{a}{c}\right)^2 - 8.52318 \left(\frac{a}{c}\right)^3$$

$$B_2 = -3.03329 + 9.96083 \left(\frac{a}{c}\right) - 12.582 \left(\frac{a}{c}\right)^2 + 5.3462 \left(\frac{a}{c}\right)^3$$

$$A_0 = 0.456128 - 0.114206 \left(\frac{a}{c}\right)^2 - 0.046523 \left(\frac{a}{c}\right)^3$$

$$A_1 = 3.022 - 10.8679 \left(\frac{a}{c}\right) + 14.94 \left(\frac{a}{c}\right)^2 - 6.8537 \left(\frac{a}{c}\right)^3$$

$$A_2 = -2.28655 + 7.88771 \left(\frac{a}{c}\right) - 11.0675 \left(\frac{a}{c}\right)^2 + 5.16354 \left(\frac{a}{c}\right)^3$$

$$M_{1C} = \frac{\pi}{\sqrt{4Q}} (30F_2 - 18F_1) - 8, \quad M_{2C} = \frac{\pi}{\sqrt{4Q}} (60F_1 - 90F_2) + 15, \quad M_{3C} = -(1 + M_1 + M_2)$$

$$F_1 = \left[1.14326 + 0.0175996 \left(\frac{a}{t}\right) + 0.501001 \left(\frac{a}{t}\right)^2 \right] \left(\frac{a}{c}\right)^\alpha, \quad \alpha = 0.458320 - 0.102985 \left(\frac{a}{t}\right) - 0.398175 \left(\frac{a}{t}\right)^2$$

$$F_2 = \left[0.976770 - 0.131975 \left(\frac{a}{t}\right) + 0.484875 \left(\frac{a}{t}\right)^2 \right] \left(\frac{a}{c}\right)^\beta, \quad \beta = 0.448863 - 0.173295 \left(\frac{a}{t}\right) - 0.267775 \left(\frac{a}{t}\right)^2$$

$$Q = 1 + 1.464 \left(\frac{a}{c}\right)^{1.65}$$

Solution 4

Solution method: empirical formula based on finite-element calculations [18].

$$\begin{aligned}
 K &= (\sigma_m F_m + \sigma_b F_b) \sqrt{\frac{\pi a}{Q}} \\
 F_m &= \left[M_1 + M_2 \left(\frac{a}{t} \right)^2 + M_3 \left(\frac{a}{t} \right)^4 \right] g f_\phi f_w \\
 F_b &= F_m [H_1 + (H_2 - H_1) \sin^p \phi] \\
 f_w &= \left[\sec \left(\frac{\pi c}{2W} \sqrt{\frac{a}{t}} \right) \right]^2
 \end{aligned} \tag{3.12}$$

 At $a/c \leq 1$:

$$\begin{aligned}
 M_1 &= 1.13 - 0.09 \frac{a}{c}, M_2 = -0.54 + \frac{0.89}{0.2 + \frac{a}{c}}, M_3 = 0.5 - \frac{1}{0.65 + \frac{a}{c}} + 14 \left(1 - \frac{a}{c} \right)^{24} \\
 g &= 1 + \left[0.1 + 0.35 \left(\frac{a}{t} \right)^2 \right] (1 - \sin \phi)^2 \\
 Q &= 1 + 1.464 \left(\frac{a}{c} \right)^{1.65}, f_\phi = \left(\sin^2 \phi + \frac{a^2}{c^2} \cos^2 \phi \right)^{\frac{1}{4}} \\
 p &= 0.2 + \frac{a}{c} + 0.6 \frac{a}{t} \\
 H_1 &= 1 - 0.34 \frac{a}{t} - 0.11 \frac{a}{c} \frac{a}{t} \\
 H_2 &= 1 + \left(-1.22 - 0.12 \frac{a}{c} \right) \frac{a}{t} + \left[0.55 - 1.05 \left(\frac{a}{c} \right)^{0.75} + 0.47 \left(\frac{a}{c} \right)^{1.5} \right] \left(\frac{a}{t} \right)^2
 \end{aligned}$$

 At $a/c > 1$:

$$\begin{aligned}
 M_1 &= \sqrt{\frac{c}{a}} \left(1 + 0.04 \frac{c}{a} \right), M_2 = 0.2 \left(\frac{c}{a} \right)^4, M_3 = -0.11 \left(\frac{c}{a} \right)^4 \\
 g &= 1 + \left[0.1 + 0.35 \frac{c}{a} \left(\frac{a}{t} \right)^2 \right] (1 - \sin \phi)^2 \\
 Q &= 1 + 1.464 \left(\frac{c}{a} \right)^{1.65}, f_\phi = \left(\cos^2 \phi + \frac{c^2}{a^2} \sin^2 \phi \right)^{\frac{1}{4}} \\
 p &= 0.2 + \frac{c}{a} + 0.6 \frac{a}{t} \\
 H_1 &= 1 + \left(-0.04 - 0.41 \frac{c}{a} \right) \frac{a}{t} + \left[0.55 - 1.93 \left(\frac{c}{a} \right)^{0.75} + 1.38 \left(\frac{c}{a} \right)^{1.5} \right] \left(\frac{a}{t} \right)^2 \\
 H_2 &= 1 + \left(-2.11 + 0.77 \frac{c}{a} \right) \frac{a}{t} + \left[0.55 - 0.72 \left(\frac{c}{a} \right)^{0.75} + 0.14 \left(\frac{c}{a} \right)^{1.5} \right] \left(\frac{a}{t} \right)^2
 \end{aligned}$$

3.3.2 Limit load parameter

Solution 1

Local limit load equation [19]:

$$L_r = \frac{(1-\xi)^{1.38} \frac{\sigma_{bl}}{3} + \sqrt{(1-\xi)^{3.16} \frac{\sigma_{bl}^2}{9} + (1-\xi)^{3.14} \sigma_{ml}^2}}{(1-\xi)^2 R_e}$$

$$\xi = \frac{ac}{t(c+t)} \quad \text{for } W \geq c+t$$

$$\xi = \frac{ac}{tW} \quad \text{for } W < c+t$$
(3.13)

Solution 2

Global limit load equation [16], extension of [12]:

At $\alpha \leq \alpha_0$ (shallow crack):

$$\sigma_{ref} = \begin{cases} \frac{\gamma + \sqrt{\gamma^2 + d_1}}{d_1} \sigma_m, & \lambda = 0 \\ \frac{2\sigma_b}{3} \left\{ (1-\gamma)^2 + 2\gamma(\alpha-\gamma) \right\}, & \lambda = \infty \\ \frac{2\lambda + \gamma + \sqrt{(2\lambda + \gamma)^2 + d_1}}{d_1} \sigma_m, & 0 < \lambda < \infty \end{cases}$$
(3.14a)

At $\alpha > \alpha_0$ (deep crack):

$$\sigma_{ref} = \begin{cases} \frac{\gamma \frac{1-\alpha}{\alpha-\gamma} + \sqrt{\left(\gamma \frac{1-\alpha}{\alpha-\gamma}\right)^2 + \frac{\alpha}{\alpha-\gamma} d_2}}{d_2} \sigma_m, & \lambda = 0 \\ \frac{2\sigma_b}{3} \left\{ (1-\gamma) \left[2 - \alpha \frac{1-\gamma}{\alpha-\gamma} \right] + 2\gamma(1-\alpha) \right\}, & \lambda = \infty \\ \frac{2\lambda + \gamma \frac{1-\alpha}{\alpha-\gamma} + \sqrt{\left(2\lambda + \gamma \frac{1-\alpha}{\alpha-\gamma}\right)^2 + \frac{\alpha}{\alpha-\gamma} d_2}}{d_2} \sigma_m, & 0 < \lambda < \infty \end{cases}$$
(3.14b)

Here

$$\alpha_0 = 1, \quad \lambda = 0$$

$$\alpha_0 = \frac{1}{1-2\beta}, \quad \lambda = \infty$$

$$\alpha_0 = -\left(\lambda - \frac{1}{2}\right) + \sqrt{\left(\lambda - \frac{1}{2}\right)^2 + \frac{\lambda}{1-0.5\beta}}, \quad 0 < \lambda < \infty$$
(3.14c)

$$\alpha = \frac{a}{t}, \beta = \frac{c}{W}, \gamma = \alpha\beta, \lambda = \frac{\sigma_{bl}}{6\sigma_{mL}}$$

$$d_1 = (1-\gamma)^2 + 2\gamma(\alpha-\gamma), \quad d_2 = (1-\gamma) \left[2 - \frac{\alpha(1-\gamma)}{\alpha-\gamma} \right] + 2\gamma(1-\alpha)$$

Solution 3

Global limit load equation [32], no bending restraint:

$$L_r = \frac{\xi\sigma_{mL} + \frac{\sigma_{bl}}{3} + \sqrt{\left(\xi\sigma_{mL} + \frac{\sigma_{bl}}{3}\right)^2 + (1-\xi)^2\sigma_{mL}^2}}{(1-\xi)^2 R_c}$$

$$\xi = \frac{ac}{t(c+t)} \quad \text{for } W \geq c+t$$

$$\xi = \frac{ac}{tW} \quad \text{for } W < c+t$$
(3.15)

3.5 Quarter-elliptical corner crack

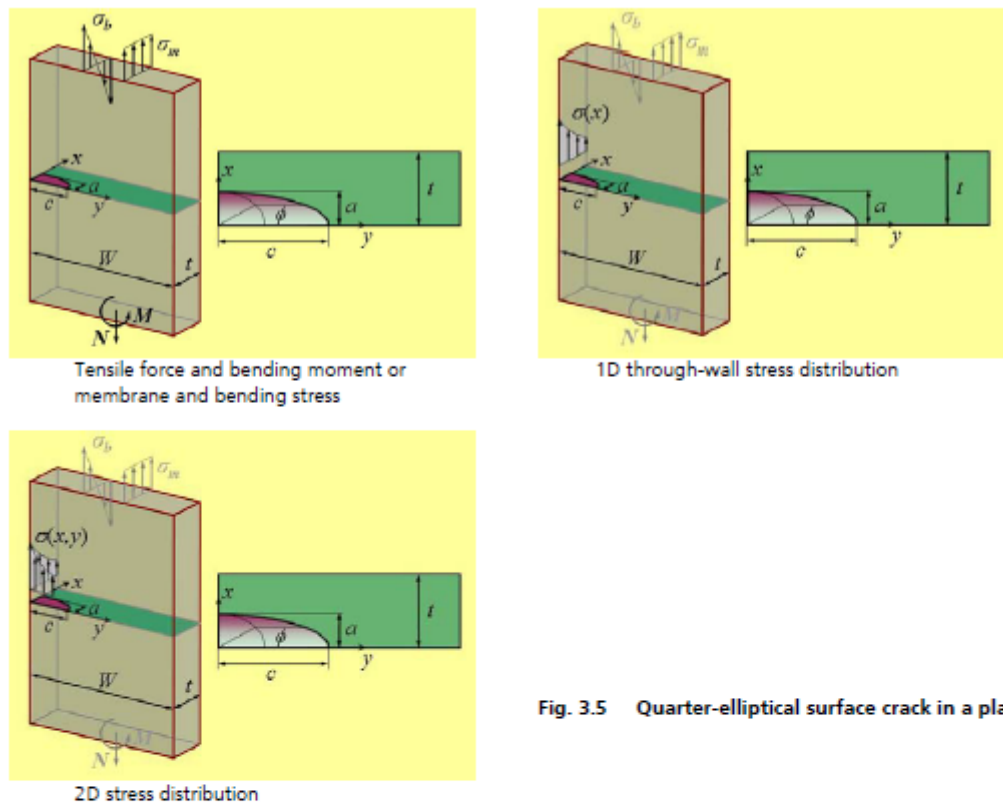


Fig. 3.5 Quarter-elliptical surface crack in a plate

Stress intensity factor, K_I

Solution	Reference	Validity range	Loading	Error	Default	Usage in FAP
1	[26]	$a/t \leq 0.9, 0.1 \leq a/c \leq 1.5, c/W \leq 0.5, 0^\circ \leq \phi \leq 90^\circ$	2D stress field	< 5%	•	-
2	[18]	$a/t < 1, 0.2 \leq a/c \leq 2, c/W \leq 0.5, 0^\circ \leq \phi \leq 90^\circ$	membrane and bending stress	~ 10%		FKM

Limit load parameter, L_r

Solution	Reference	Validity range	Loading	Default	Usage in FAP
1	[19]	$a/t \leq 0.8$	membrane and bending stress; linearization of the stress field	•	FKM
2	[16]	$a/t \leq 0.8$	membrane and bending stress; linearization of the stress field	-	-
3	[32]	$a/t \leq 0.8$	membrane and bending stress; linearization of the stress field	-	BS 7910

3.5.1 Stress intensity factor

Solution 1

Solution method: polynomial influence functions based of finite-element analyses [26].

The stress field in the crack plane is considered to be a 2D function of the coordinates x and y , as given by Eq. (2.9), with $m_{\max} = n_{\max} = 4$. The influence functions f_{mn} were numerically derived in [26] for polynomial type loading

$$\sigma_{mn} = \left(\frac{x}{a}\right)^m \left(\frac{y}{c}\right)^n,$$

assuming a wide plate with

$$W = \max(6t, 6c).$$

The stress intensity factor at an arbitrary point on the crack front is then calculated by

$$K\left(\frac{a}{c}, \frac{a}{t}, \frac{c}{W}, \phi\right) = \left[\sum_{m=0}^4 \sum_{n=0}^4 D_{mn} f_{mn}\left(\frac{a}{c}, \frac{a}{t}, \phi\right) \left(\frac{a}{t}\right)^{m+n} \left(\frac{a}{c}\right)^{-n} \right] \sqrt{\frac{\pi a}{Q}} f_w\left(\frac{c}{W}, \frac{a}{t}\right). \quad (3.20)$$

Here

$$\begin{aligned} Q &= 1 + 1.464(a/c)^{1.65}, a/c \leq 1 \\ Q &= 1 + 1.464(c/a)^{1.65}, a/c > 1 \end{aligned} \quad (3.21)$$

and the finite width correction is assumed according to [18]:

$$f_w = 1 - 0.2\lambda + 9.4\lambda^2 - 19.4\lambda^3 + 27.1\lambda^4, \quad \lambda = \frac{c}{W} \sqrt{\frac{a}{t}}. \quad (3.22)$$

Solution 2

Solution method: empirical formula based on finite-element calculations [18].

$$\begin{aligned}
 K &= (\sigma_m F_m + \sigma_b F_b) \sqrt{\frac{\pi a}{Q}} \\
 F_m &= \left[M_1 + M_2 \left(\frac{a}{t} \right)^2 + M_3 \left(\frac{a}{t} \right)^4 \right] g_1 g_2 f_\phi f_w \\
 F_b &= F_m [H_1 + (H_2 - H_1) \sin^p \phi] \\
 f_w &= 1 - 0.2\lambda + 9.4\lambda^2 - 19.4\lambda^3 + 27.1\lambda^4, \lambda = \frac{c}{W} \sqrt{\frac{a}{t}}
 \end{aligned} \tag{3.23}$$

At $a/c \leq 1$:

$$\begin{aligned}
 M_1 &= 1.08 - 0.03 \frac{a}{c}, M_2 = -0.44 + \frac{1.06}{0.3 + \frac{a}{c}}, M_3 = -0.5 + 0.25 \frac{a}{c} + 14.8 \left(1 - \frac{a}{c} \right)^{15} \\
 g_1 &= 1 + \left[0.08 + 0.4 \left(\frac{a}{t} \right)^2 \right] (1 - \sin \phi)^3, g_2 = 1 + \left[0.08 + 0.15 \left(\frac{a}{t} \right)^2 \right] (1 - \cos \phi)^3 \\
 Q &= 1 + 1.464 \left(\frac{a}{c} \right)^{1.65}, f_\phi = \left(\sin^2 \phi + \frac{a^2}{c^2} \cos^2 \phi \right)^{\frac{1}{4}} \\
 p &= 0.2 + \frac{a}{c} + 0.6 \frac{a}{t} \\
 H_1 &= 1 - 0.34 \frac{a}{t} - 0.11 \frac{a}{c} \frac{a}{t} \\
 H_2 &= 1 + \left(-1.22 - 0.12 \frac{a}{c} \right) \frac{a}{t} + \left[0.64 - 1.05 \left(\frac{a}{c} \right)^{0.75} + 0.47 \left(\frac{a}{c} \right)^{1.5} \right] \left(\frac{a}{t} \right)^2
 \end{aligned}$$

At $a/c > 1$:

$$\begin{aligned}
 M_1 &= \sqrt{\frac{c}{a}} \left(1.08 - 0.03 \frac{c}{a} \right), M_2 = 0.375 \left(\frac{c}{a} \right)^2, M_3 = -0.25 \left(\frac{c}{a} \right)^2 \\
 g_1 &= 1 + \left[0.08 + 0.4 \left(\frac{c}{a} \right)^2 \left(\frac{a}{t} \right)^2 \right] (1 - \sin \phi)^3, g_2 = 1 + \left[0.08 + 0.15 \left(\frac{c}{a} \right)^2 \left(\frac{a}{t} \right)^2 \right] (1 - \cos \phi)^3 \\
 Q &= 1 + 1.464 \left(\frac{c}{a} \right)^{1.65}, f_\phi = \left(\cos^2 \phi + \frac{c^2}{a^2} \sin^2 \phi \right)^{\frac{1}{4}} \\
 p &= 0.2 + \frac{c}{a} + 0.6 \frac{a}{t} \\
 H_1 &= 1 + \left(-0.04 - 0.41 \frac{c}{a} \right) \frac{a}{t} + \left[0.55 - 1.93 \left(\frac{c}{a} \right)^{0.75} + 1.38 \left(\frac{c}{a} \right)^{1.5} \right] \left(\frac{a}{t} \right)^2 \\
 H_2 &= 1 + \left(-2.11 + 0.77 \frac{c}{a} \right) \frac{a}{t} + \left[0.64 - 0.72 \left(\frac{c}{a} \right)^{0.75} + 0.14 \left(\frac{c}{a} \right)^{1.5} \right] \left(\frac{a}{t} \right)^2
 \end{aligned}$$

3.5.2 Limit load parameter

The limit load is determined using equations for the plate with a semi-elliptical crack. The results can appear to be slightly non-conservative.

Solution 1

Local limit load equation [19]:

$$L_y = \frac{(1-\xi)^{1.58} \frac{\sigma_{bL}}{3} + \sqrt{(1-\xi)^{3.16} \frac{\sigma_{bL}^2}{9} + (1-\xi)^{3.14} \sigma_{mL}^2}}{(1-\xi)^2 R_y}$$

$$\xi = \frac{ac}{t(c+t)} \quad \text{for } W \geq c+t \quad (3.24)$$

$$\xi = \frac{ac}{tW} \quad \text{for } W < c+t$$

Solution 2

Global limit load equation [16], extension of [12]:

At $\alpha \leq \alpha_0$ (shallow crack):

$$\sigma_{ref} = \begin{cases} \frac{\gamma + \sqrt{\gamma^2 + d_1}}{d_1} \sigma_m, & \lambda = 0 \\ \frac{2\sigma_b}{3} \left\{ (1-\gamma)^2 + 2\gamma(\alpha-\gamma) \right\}, & \lambda = \infty \\ \frac{2\lambda + \gamma + \sqrt{(2\lambda + \gamma)^2 + d_1}}{d_1} \sigma_m, & 0 < \lambda < \infty \end{cases} \quad (3.25a)$$

At $\alpha > \alpha_0$ (deep crack):

$$\sigma_{ref} = \begin{cases} \frac{\gamma \frac{1-\alpha}{\alpha-\gamma} + \sqrt{\left(\gamma \frac{1-\alpha}{\alpha-\gamma}\right)^2 + \frac{\alpha}{\alpha-\gamma} d_2}}{d_2} \sigma_m, & \lambda = 0 \\ \frac{2\sigma_b}{3} \left\{ (1-\gamma) \left[2 - \alpha \frac{1-\gamma}{\alpha-\gamma} \right] + 2\gamma(1-\alpha) \right\}, & \lambda = \infty \\ \frac{2\lambda + \gamma \frac{1-\alpha}{\alpha-\gamma} + \sqrt{\left(2\lambda + \gamma \frac{1-\alpha}{\alpha-\gamma}\right)^2 + \frac{\alpha}{\alpha-\gamma} d_2}}{d_2} \sigma_m, & 0 < \lambda < \infty \end{cases} \quad (3.25b)$$

Here

$$\begin{aligned}
\alpha_0 &= 1, \quad \lambda = 0 \\
\alpha_0 &= \frac{1}{1-2\beta}, \quad \lambda = \infty \\
\alpha_0 &= -\left(\lambda - \frac{1}{2}\right) + \sqrt{\left(\lambda - \frac{1}{2}\right)^2 + \frac{\lambda}{1-0.5\beta}}, \quad 0 < \lambda < \infty \\
\alpha &= \frac{a}{t}, \quad \beta = \frac{c}{W}, \quad \gamma = \alpha\beta, \quad \lambda = \frac{\sigma_{bl}}{6\sigma_{mL}} \\
d_1 &= (1-\gamma)^2 + 2\gamma(\alpha-\gamma), \quad d_2 = (1-\gamma)\left[2 - \frac{\alpha(1-\gamma)}{\alpha-\gamma}\right] + 2\gamma(1-\alpha)
\end{aligned} \tag{3.25c}$$

Solution 3

Global limit load equation [32], no bending restraint:

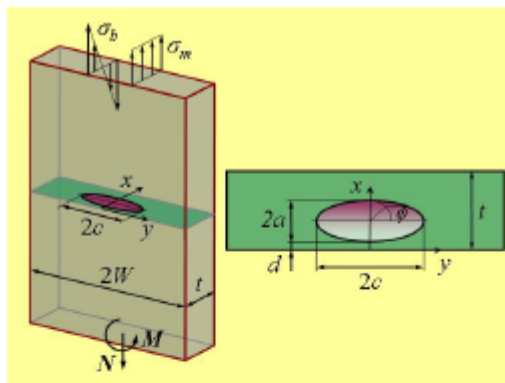
$$\begin{aligned}
L_r &= \frac{\xi\sigma_{mL} + \frac{\sigma_{bl}}{3} + \sqrt{\left(\xi\sigma_{mL} + \frac{\sigma_{bl}}{3}\right)^2 + (1-\xi)^2\sigma_{mL}^2}}{(1-\xi)^2 R_e} \\
\xi &= \frac{ac}{t(c+t)} \quad \text{for } W \geq c+t \\
\xi &= \frac{ac}{tW} \quad \text{for } W < c+t
\end{aligned} \tag{3.26}$$

The solution, Eq. (3.26), is used in [5] with the following definition of ξ :

$$\begin{aligned}
\xi &= \frac{ac}{t(c+2t)} \quad \text{for } W \geq c+2t \\
\xi &= \frac{ac}{tW} \quad \text{for } W < c+2t
\end{aligned}$$

This leads to an underestimation of the parameter L_r as compared to Eq. (3.26).

3.6 Elliptical embedded crack



Tensile force and bending moment or membrane and bending stress

Fig. 3.6 Elliptical embedded crack in a plate

Stress intensity factor, K_I

Solution	Ref.	Validity range	Loading	Error	De-fault	Usage in FAP
1	[1,22]	$0.125 \leq a/c \leq 1$, $a/(a+d) \leq 0.9$ or $a/(t-a-d) \leq 0.9$, $c/W \leq 0.5$, $180^\circ \leq \phi \leq 180^\circ$	membrane and bending stress	~5%	•	API 579, FKM

Limit load parameter, L_r

Solution	Ref.	Validity range	Loading	Error	De-fault	Usage in FAP
1	[32]	$a/(a+d) \leq 0.8$ or $a/(t-a-d) \leq 0.8$	membrane and bending stress; linearization of 1D stress field	-	•	API 579, BS 7910, DNV, FKM

3.6.1 Stress intensity factor

Solution 1

Solution method: empirical equation obtained by fitting numerical data [1,22].

$$K = (\sigma_{m0} F_m + \sigma_{b0} F_b) \sqrt{\frac{\pi a}{Q}} f_\phi f_w$$

$$\sigma_{m0} = \sigma_m + \sigma_b \left[1 - \frac{2}{t}(a+d) \right], \quad \sigma_{b0} = \sigma_b \frac{2a}{t} \quad (3.27)$$

$$f_\phi = \left(\sin^2 \phi + \frac{a^2}{c^2} \cos^2 \phi \right)^{\frac{1}{4}}, \quad f_w = \left[\sec \left(\frac{\pi c}{2W} \sqrt{\frac{2a}{t}} \right) \right]^{\frac{1}{2}}, \quad Q = 1 + 1.464(a/c)^{1.65}$$

$$F_m = \frac{1}{2} \sin^2 \phi [H_1(1 - \sin \phi) + H_2(1 + \sin \phi)] + H_3 \cos^2 \phi$$

$$H_1 = h_3 \left(\frac{a}{c}, \frac{a}{a+d} \right) h_1 \left(\frac{a}{c}, \frac{a}{t-a-d} \right)$$

$$H_2 = h_1 \left(\frac{a}{c}, \frac{a}{a+d} \right) h_3 \left(\frac{a}{c}, \frac{a}{t-a-d} \right)$$

$$H_3 = h_2 \left(\frac{a}{c}, \frac{a}{a+d} \right) h_2 \left(\frac{a}{c}, \frac{a}{t-a-d} \right) \quad (3.28)$$

$$h_1 \left(\frac{a}{c}, \beta \right) = 1 + \left[-0.04 + 0.085 \left(0.34 + \frac{a}{c} \right)^{-1} \right] \beta^2 + \left(0.05 - 0.03 \frac{a}{c} \right) \beta^4$$

$$h_2 \left(\frac{a}{c}, \beta \right) = 1 + \left[-0.03 + 0.075 \left(0.3 + \frac{a}{c} \right)^{-1} \right] \beta^2 + \left[0.08 - 0.024 \left(0.1 + \frac{a}{c} \right)^{-1} \right] \beta^4$$

$$h_3 \left(\frac{a}{c}, \beta \right) = 1 + \left[-0.06 + 0.07 \left(0.25 + \frac{a}{c} \right)^{-1} \right] \beta^2 + \left(0.643 - 0.343 \frac{a}{c} \right) \beta^4$$

$$F_b = - \left[0.5 + 0.2591 \left(\frac{a}{c} \right)^{1.5} - 0.09189 \left(\frac{a}{c} \right)^{2.5} \right] f_b \sin \phi$$

$$f_b = \frac{1}{2} (f_1 + f_2) - \frac{1}{2} (f_1 - f_2) \sin \phi \quad (3.29)$$

$$f_1 = 1 + \exp \left[-1.9249 - 3.9087 \left(\frac{a}{c} \right)^{0.5} + 4.1067 \left(\frac{a}{a+d} \right)^3 \right]$$

$$f_2 = 1 + \exp \left[-1.9249 - 3.9087 \left(\frac{a}{c} \right)^{0.5} + 4.1067 \left(\frac{a}{t-a-d} \right)^3 \right]$$

The membrane and bending stress components σ_{m0} and σ_{b0} in Eq. (3.27) are associated with the crack size and location. The solution due to membrane stress, Eq. (3.28), is according to [22] and is valid within $0.125 \leq a/c \leq 1$. The bending correction, Eq. (3.29), is given in [1] and applies for $0 \leq a/c \leq 1$.

3.6.2 Limit load parameter

Solution 1

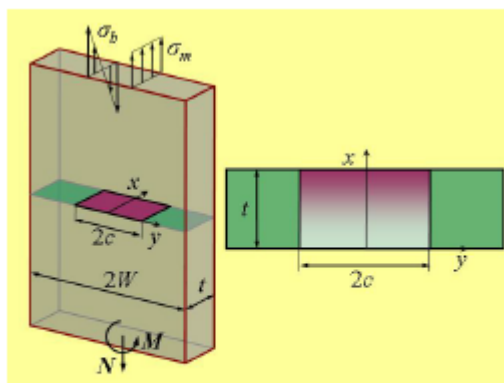
Solution is according to [32]:

$$L_r = \frac{\xi \sigma_{ml} + \frac{\sigma_{bl}}{3} + \sqrt{\left(\xi \sigma_{ml} + \frac{\sigma_{bl}}{3}\right)^2 + \left[(1-\xi)^2 + 4\xi \frac{d}{t}\right] \sigma_{ml}^2}}{\left[(1-\xi)^2 + 4\xi \frac{d}{t}\right] R_e}$$

$$\xi = \frac{2ac}{t(t+c)} \text{ for } W \geq t+c$$

$$\xi = \frac{2ac}{tW} \text{ for } W < t+c$$
(3.30)

3.7 Through-thickness crack



Tensile force and bending moment or membrane and bending stress

Fig. 3.7 Through-thickness crack in a plate

Stress intensity factor, K_I

Solu-tion	Reference	Validity range	Loading	Error	De-fault	Usage in FAP
1	[1]	$0 \leq c/W < 1$	membrane and bending stress	-	•	API 579

Limit load parameter, L_r

Solu-tion	Reference	Validity range	Loading	De-fault	Usage in FAP
1	[1,5]	$c/W \leq 0.8$	membrane and bending stress; linearization of 1D stress field	•	API 579, BS 7910

3.7.1 Stress intensity factor

Solution 1

Solution method: empirical equation [1].

$$\begin{aligned}
 K &= (\sigma_m F_m + \sigma_b F_b) \sqrt{\pi c} f_w \\
 F_m &= 1 \\
 F_b &= \frac{0.302327 + 70.50193\lambda + 110.305\lambda^2}{1 + 110.96\lambda + 98.7089\lambda^2 + 0.753594\lambda^3} \\
 \lambda &= \frac{t}{c\sqrt{10}} \\
 f_w &= \left[\sec\left(\frac{\pi c}{2W}\right) \right]^{\frac{1}{2}}
 \end{aligned} \tag{3.31}$$

3.7.2 Limit load parameter

Solution 1

Solution is given in [1,5]:

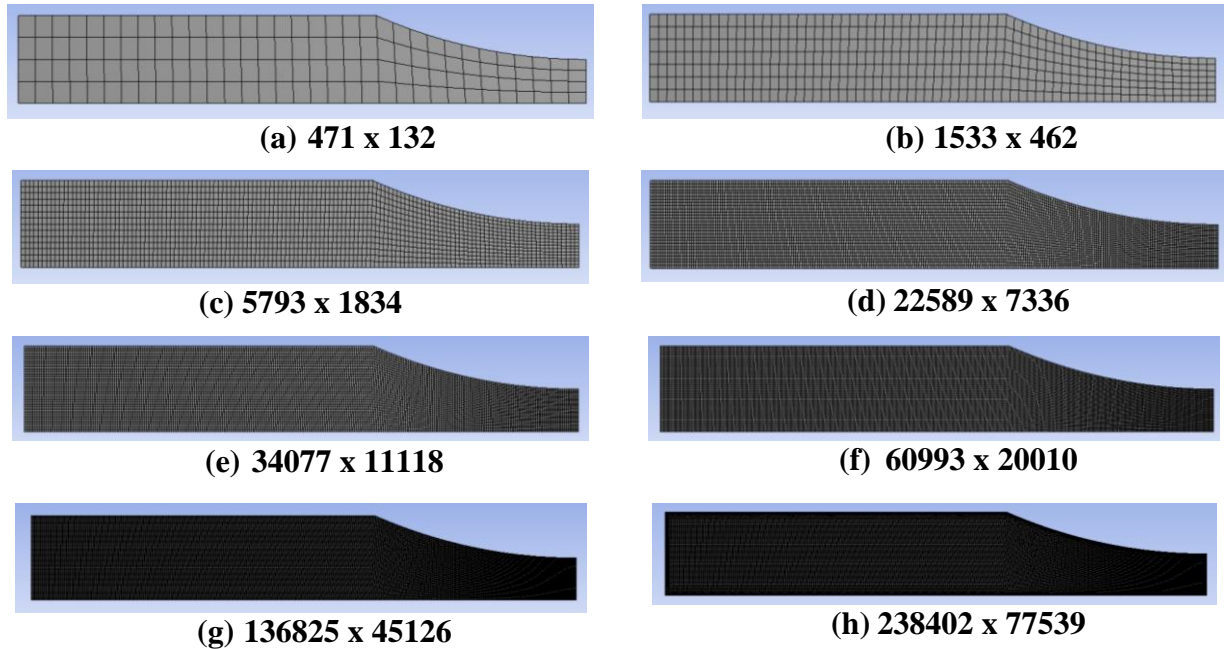
$$\begin{aligned}
 L_r &= \frac{\frac{\sigma_{bl}}{3} + \sqrt{\left(\frac{\sigma_{bl}}{3}\right)^2 + \sigma_{ml}^2}}{(1-\xi)R_e} \\
 \xi &= \frac{c}{W}
 \end{aligned} \tag{3.32}$$

In case of an infinitely wide plate, Eq. (3.32) coincides with the solution in [9,15].

APPENDIX B – CHAPTER 4

2D Model Plain Stress Analysis

2D Mesh Convergence Analysis



Mesh Division for 2D

Convergence Analysis for 2D Axial

2D Convergence Analysis for Axial Load PLANE183 (28)

Case Number	Nodes	Elements	Max. Stress (MPa)	Relative Error	Error ⁸
1	471	132	105.56		0.53%
2	1533	462	105.53	-0.03%	0.50%
3	5793	1834	105.53	0.00%	0.50%
4	22589	7336	105.54	0.01%	0.51%
5	34077	11118	105.54	0.00%	0.51%
6	60993	20010	105.54	0.00%	0.51%
7	136825	45126	105.54	0.00%	0.51%
8	238402 ⁹	77539	105.54	0.00%	0.51%

⁸ Error relatively compared with analytical solution.

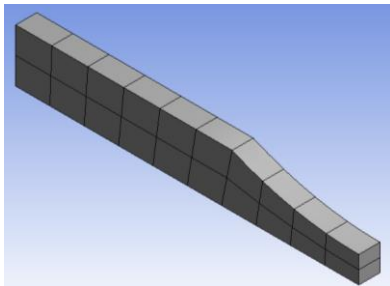
⁹ Refinement level 3 adopted on the edges.

2D Convergence Analysis for Bending Load PLANE183 (28)

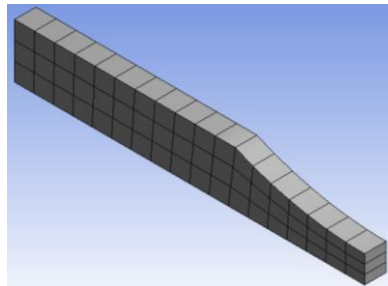
Case Number	Nodes	Elements	Max. Stress (MPa)	Relative Error	Error ⁸
1	875	264	103.62		0.60%
2	2933	924	103.64	0.02%	0.62%
3	11323	3668	103.64	0.00%	0.62%
<u>4</u>	<u>44653</u>	<u>14672</u>	<u>103.64</u>	<u>0.00%</u>	0.62%
5	67499	22236	103.64	0.00%	0.62%
6	121115	40020	103.65	0.01%	0.63%
7	272341	90252	103.65	0.00%	0.63%
8	471571 ⁹	362112	103.64	-0.01%	0.62%

3D Model Solid Analysis

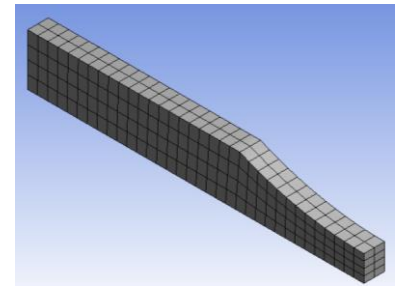
3D Mesh Convergence Analysis



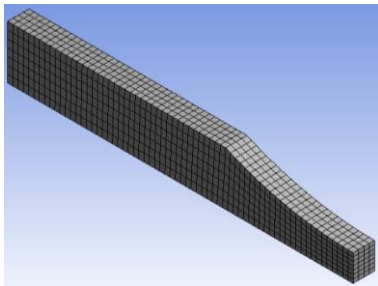
(a) 203 x 20



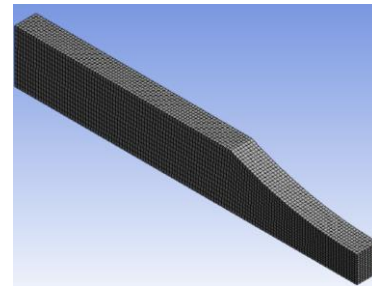
(b) 486 x 54



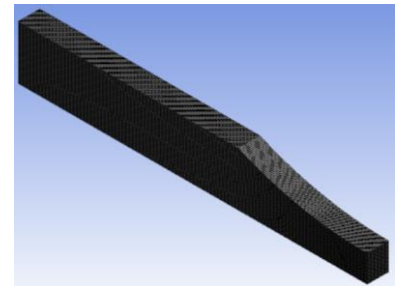
(c) 1805 x 272



(d) 9809 x 1848



(e) 67977 x 14672



(f) 506045 x 117376

Mesh Division for 3D Axial Example

Convergence Analysis for 3D Axial

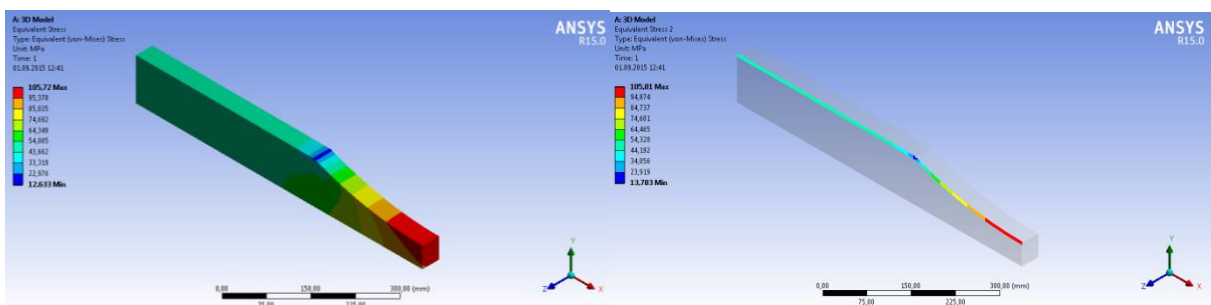
3D Convergence Analysis for Axial Load SOLID186

Nodes	Elements	Max Stress (MPa)	Relative Error	Error ⁶
203	20	106.74		1.66%
486	54	106.09	-0.61%	1.04%
1805	272	105.76	-0.31%	0.72%
9809	1848	105.72	-0.04%	0.69%
67977	14672	105.72	0.00%	0.69%
506045	117376	105.72	0.00%	0.69%
945217	222360	105.72	0.00%	0.69%

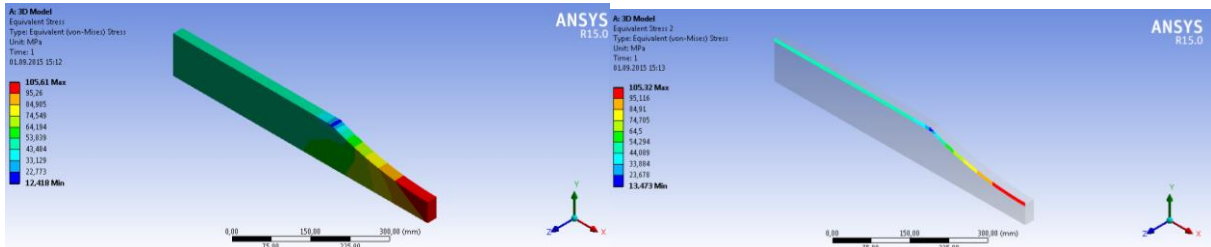
3D Convergence Analysis for Bending Load with $t = 80\text{mm}$ SOLID186

Nodes	Elements	Max Stress (MPa)	Relative Error	Error ⁶
353	40	107.05		3.93%
879	108	104.64	-2.25%	1.59%
3333	544	103.75	-0.85%	0.73%
18685	3696	103.69	-0.06%	0.67%
<u>133537</u>	<u>29568</u>	<u>103.71</u>	<u>0.02%</u>	0.69%
998957	234752	103.71	0.00%	0.69%
1875825	446080	103.71	0.00%	0.69%

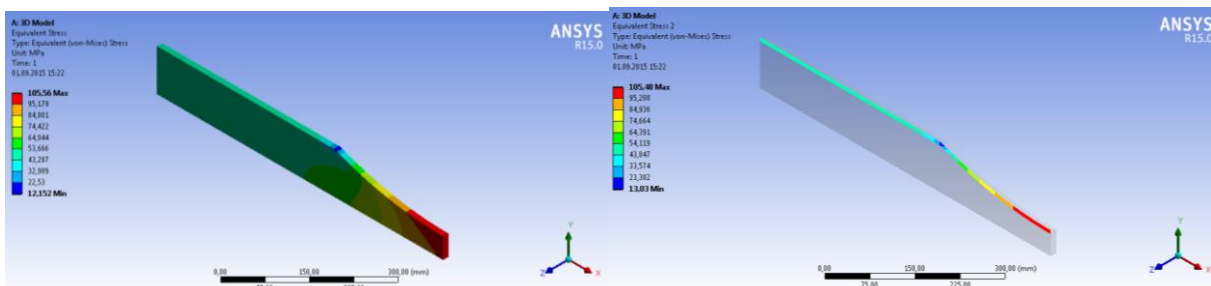
3D Model – Tensile Simulation



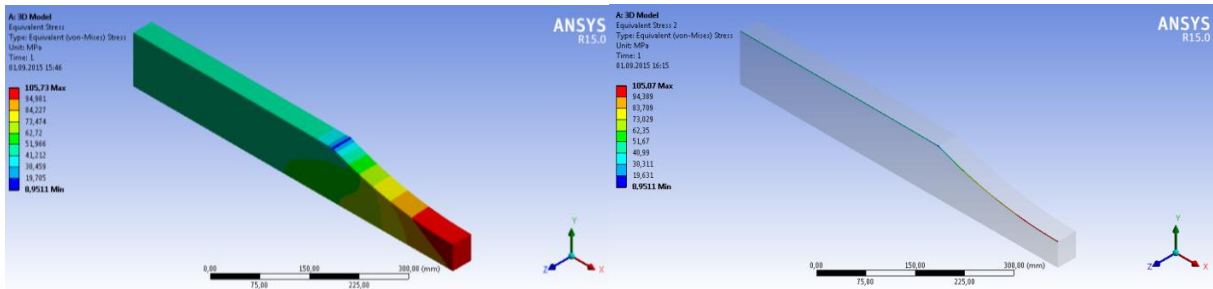
Result for 3D Ref Axial with Thickness 80mm



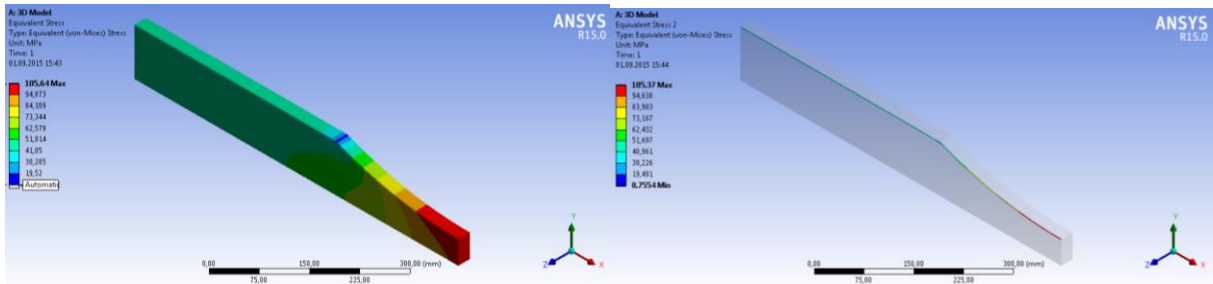
Result for 3D Ref Axial with Thickness 50mm



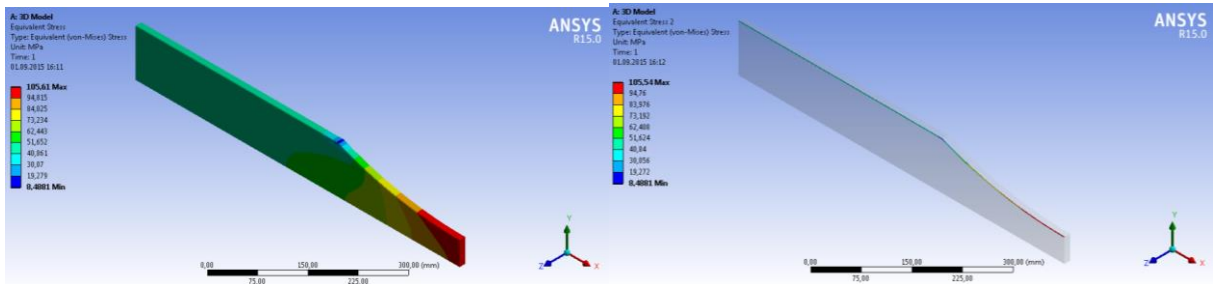
Result for 3D Ref Axial with Thickness 25mm



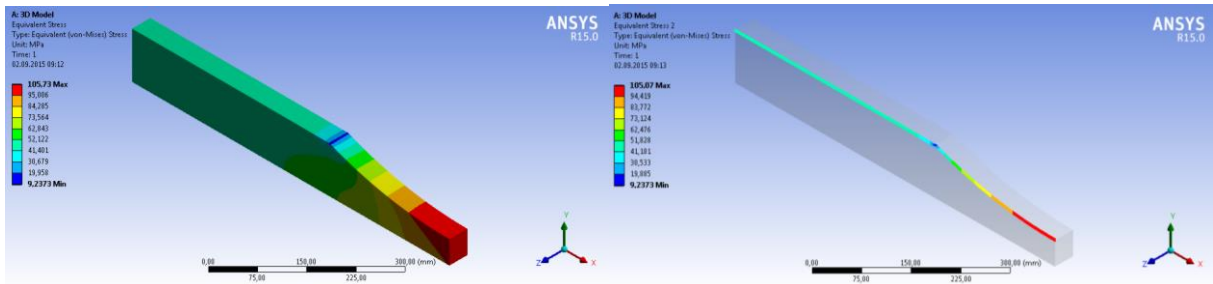
Result for 3D Axial IC with Thickness 80mm



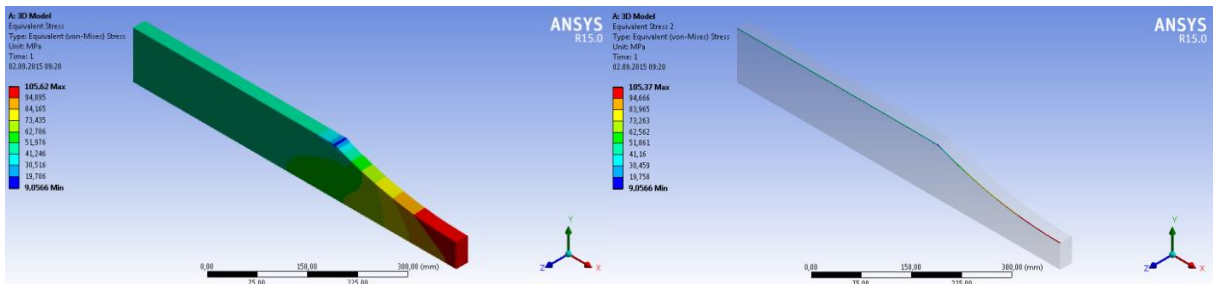
Result for 3D Axial IC with Thickness 50mm



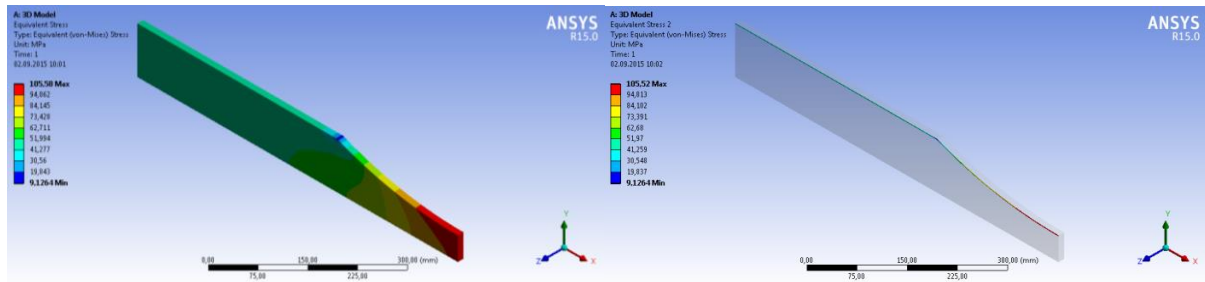
Result for 3D Axial IC with Thickness 25mm



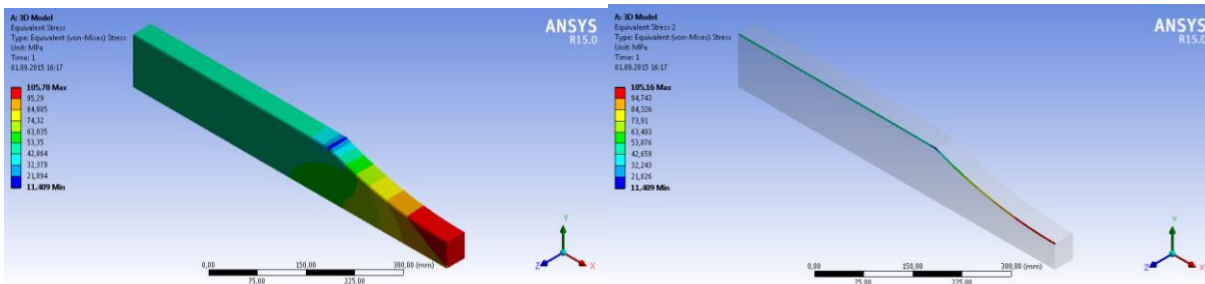
Result for 3D Axial 1R with Thickness 80mm



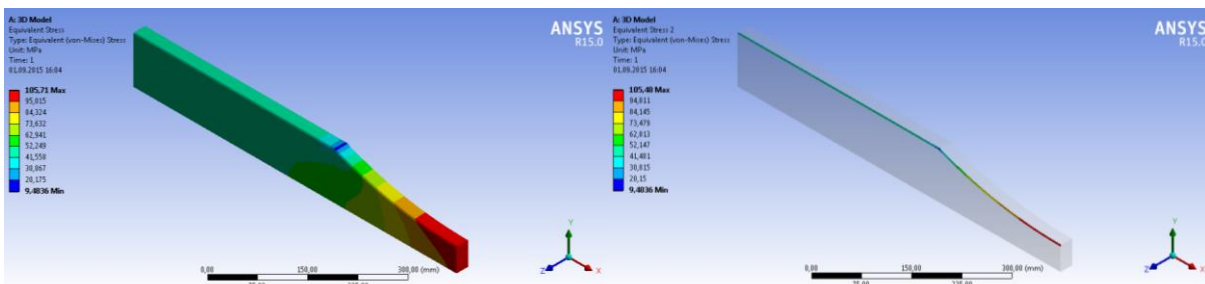
Result for 3D Axial 1R with Thickness 50mm



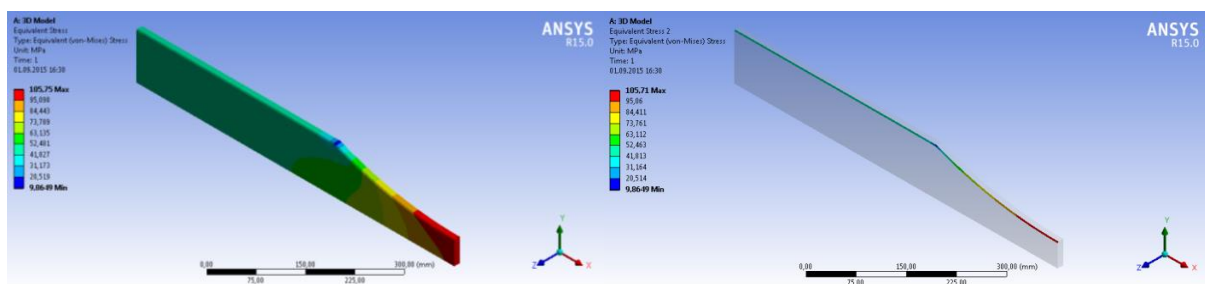
Result for 3D Axial 1R with Thickness 25mm



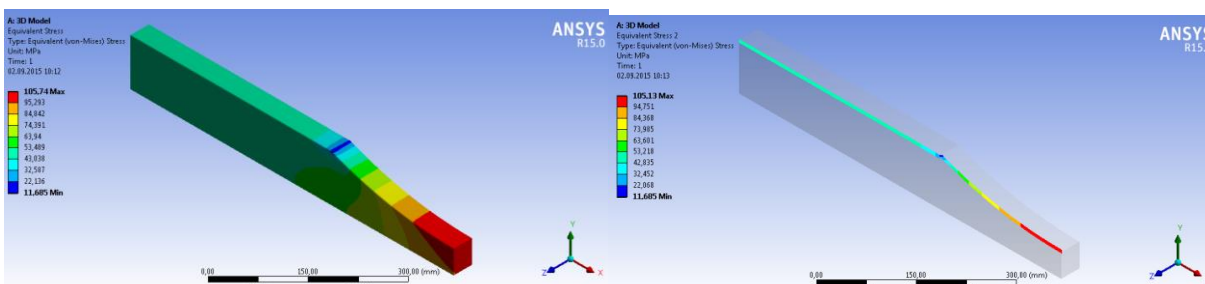
Result for 3D Axial 2C with Thickness 80mm



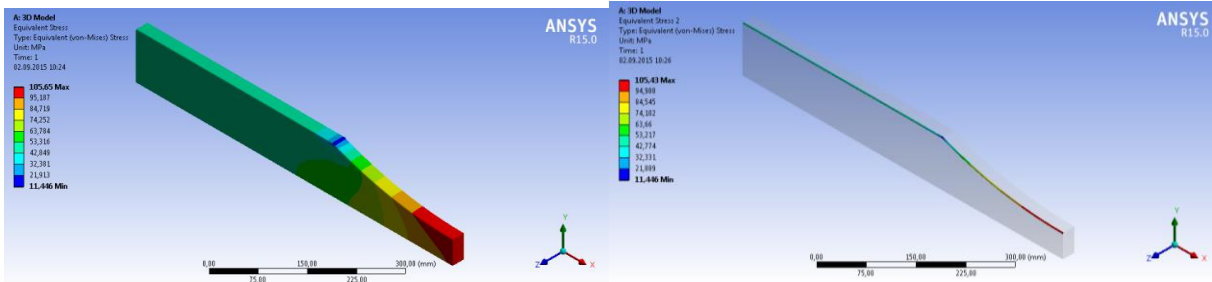
Result for 3D Axial 2C with Thickness 50mm



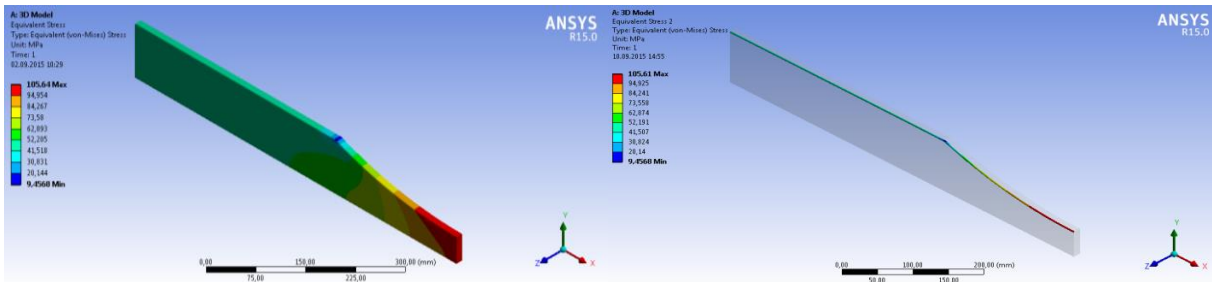
Result for 3D Axial 2C with Thickness 25mm



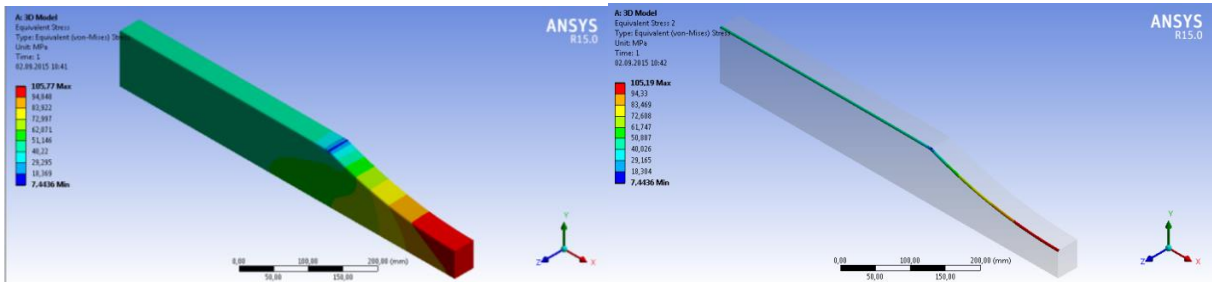
Result for 3D Axial 2R with Thickness 80mm



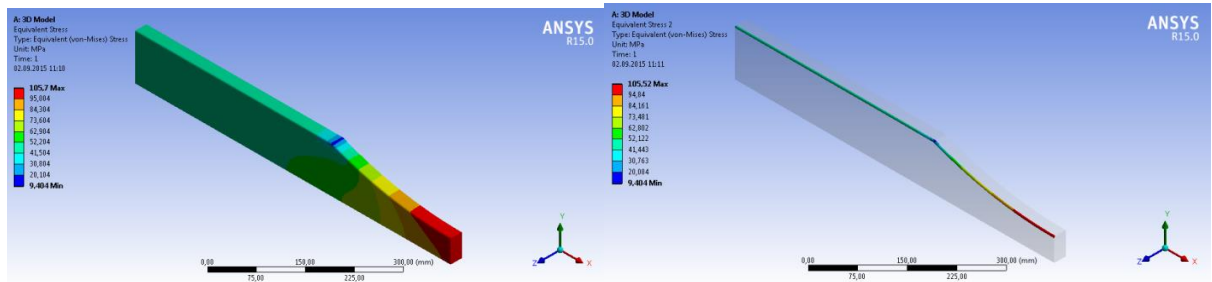
Result for 3D Axial 2R with Thickness 50mm



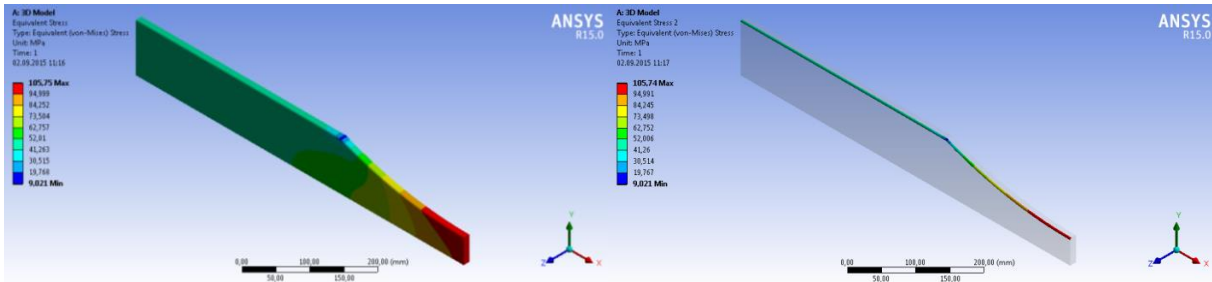
Result for 3D Axial 2R with Thickness 25mm



Result for 3D Axial 3R with Thickness 80mm

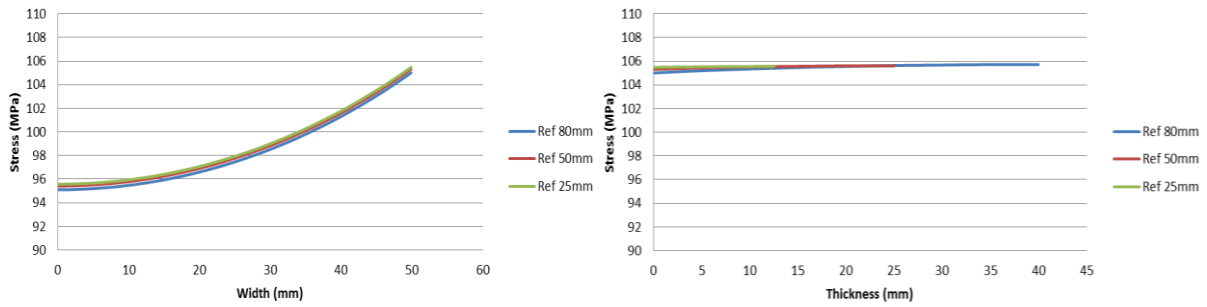


Result for 3D Axial 3R with Thickness 50mm

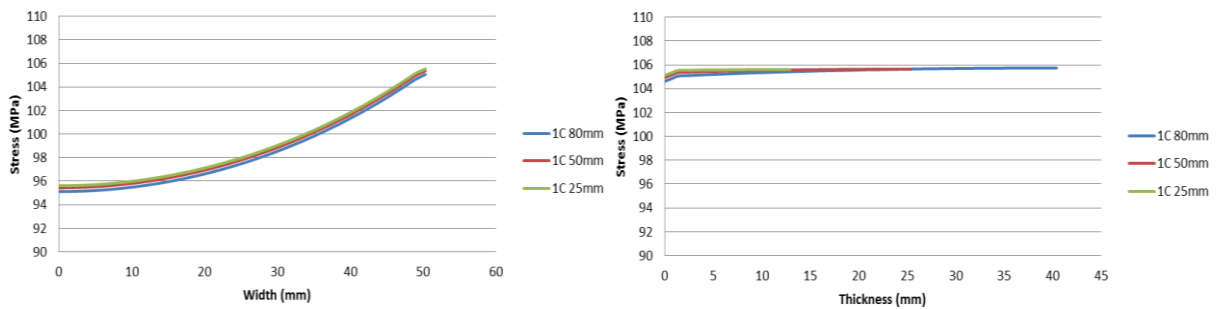


Result for 3D Axial 3R with Thickness 25mm

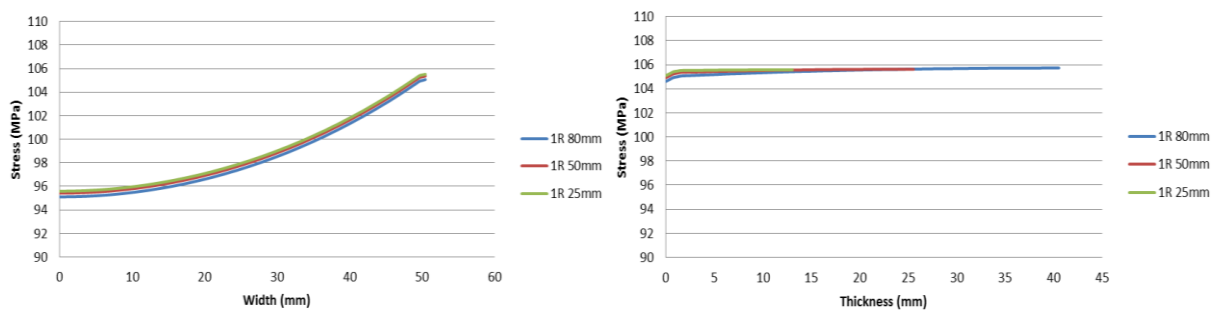
Stress Distribution for Axial Simulation



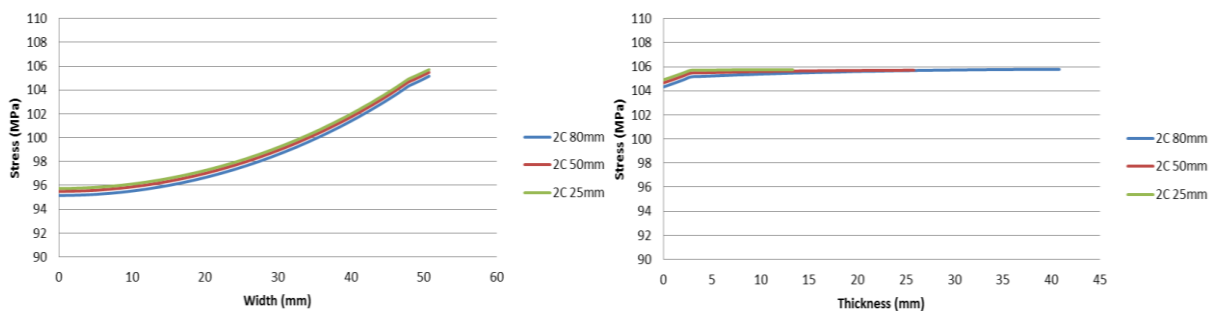
Axial 3D Ref Model Equivalent Stress Variation with Respect to Width and Thickness



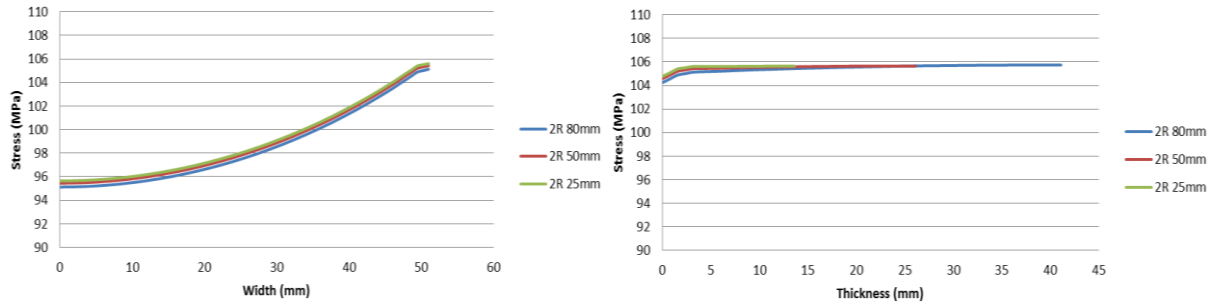
Axial 3D 1C Model Equivalent Stress Variation with Respect to Width and Thickness



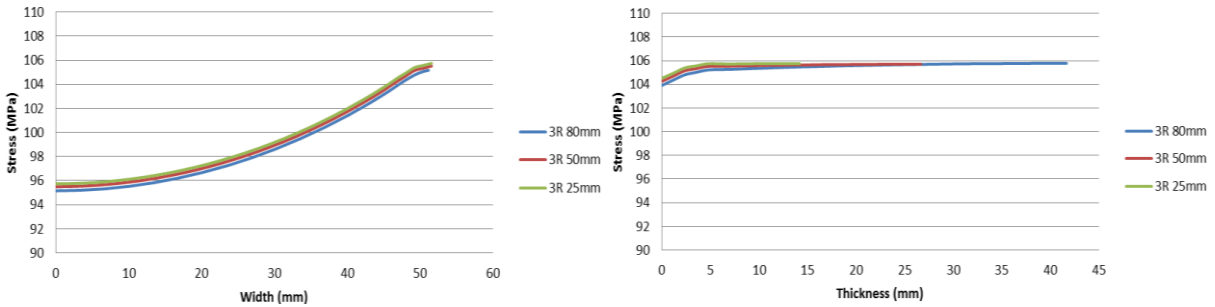
Axial 3D 1R Model Equivalent Stress Variation with Respect to Width and Thickness



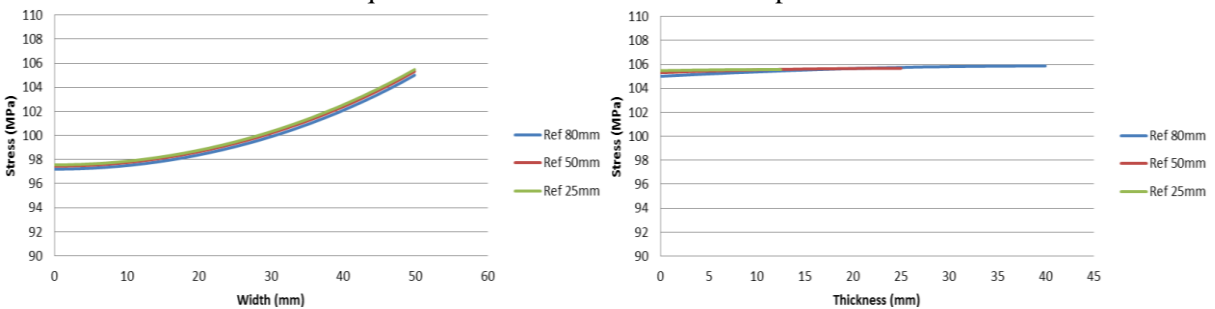
Axial 3D 2C Model Equivalent Stress Variation with Respect to Width and Thickness



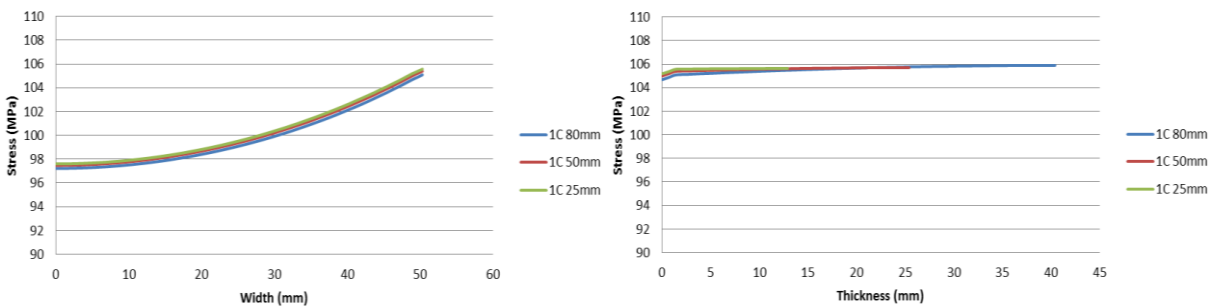
Axial 3D 2R Model Equivalent Stress Variation with Respect to Width and Thickness



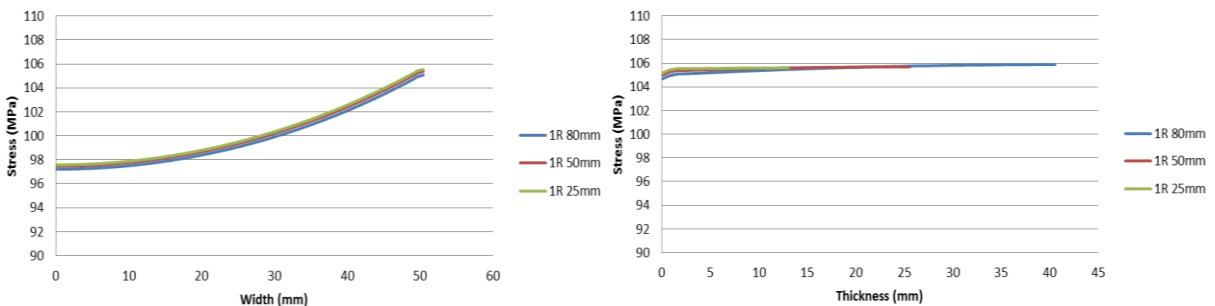
Axial 3D 3R Model Equivalent Stress Variation with Respect to Width and Thickness



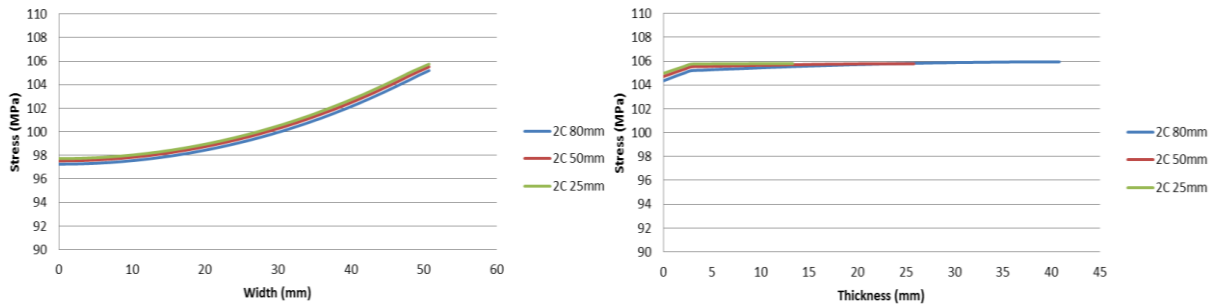
Axial 3D Ref Model Normal Stress Variation with Respect to Width and Thickness



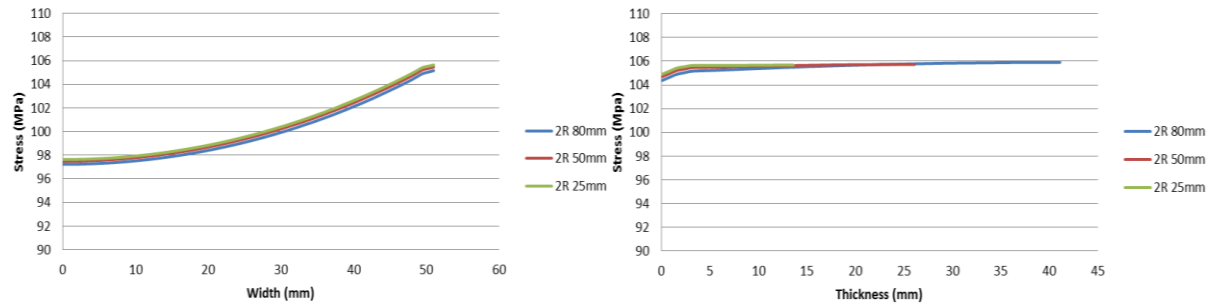
Axial 3D 1C Model Normal Stress Variation with Respect to Width and Thickness



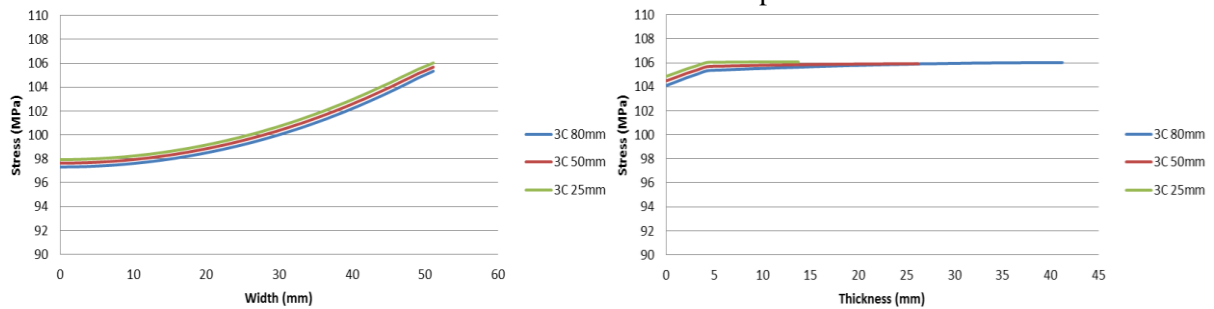
Axial 3D 1R Model Normal Stress Variation with Respect to Width and Thickness



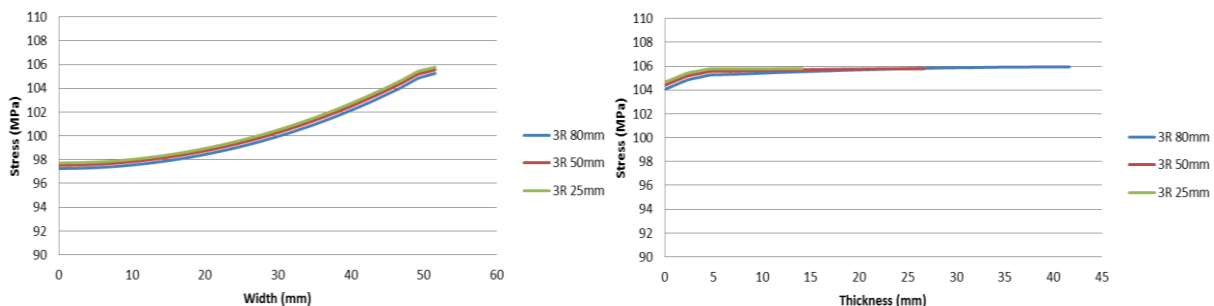
Axial 3D 2C Model Normal Stress Variation with Respect to Width and Thickness



Axial 3D 2R Model Normal Stress Variation with Respect to Width and Thickness

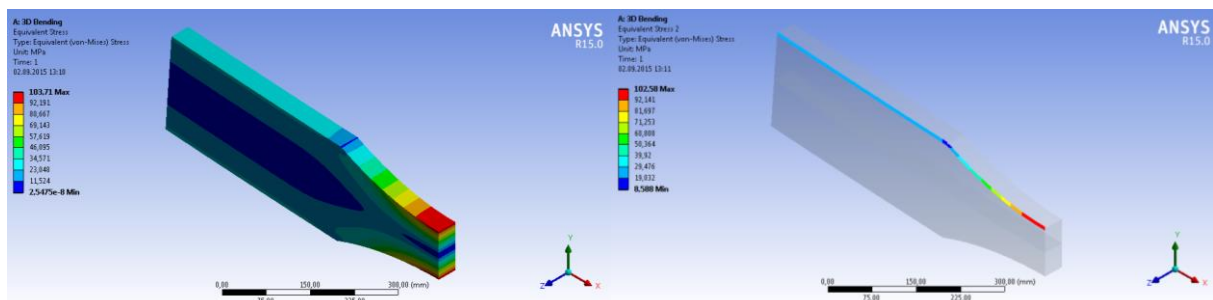


Axial 3D 3C Model Normal Stress Variation with Respect to Width and Thickness

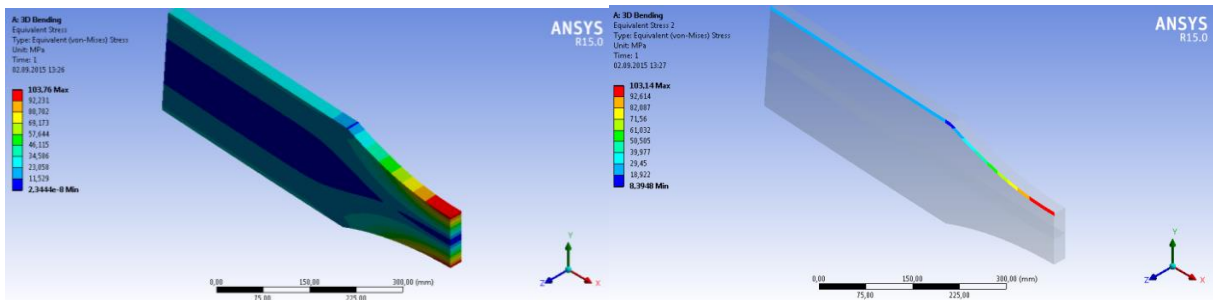


Axial 3D 3R Model Normal Stress Variation with Respect to Width and Thickness

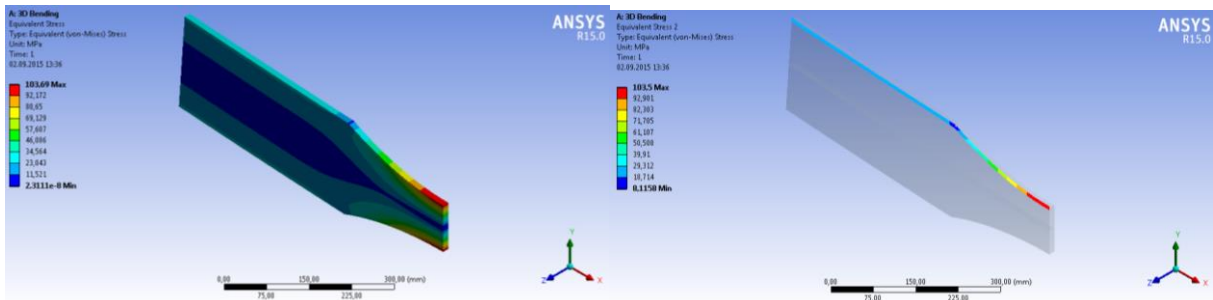
3D Model – Bending Simulation



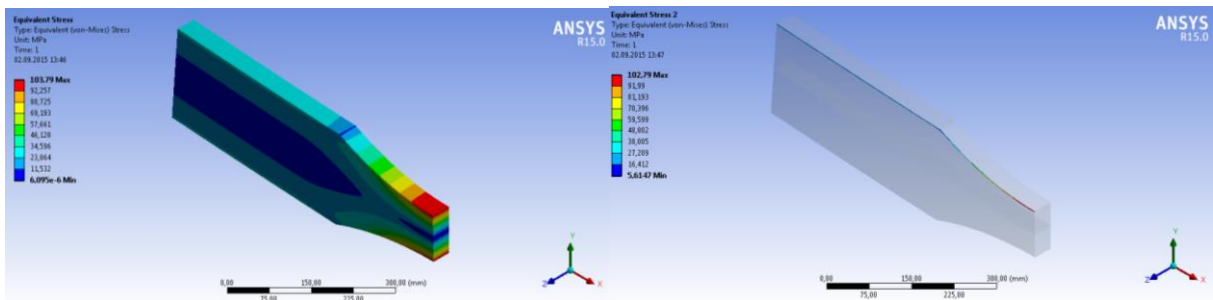
Result for 3D Ref Bending with Thickness 80mm



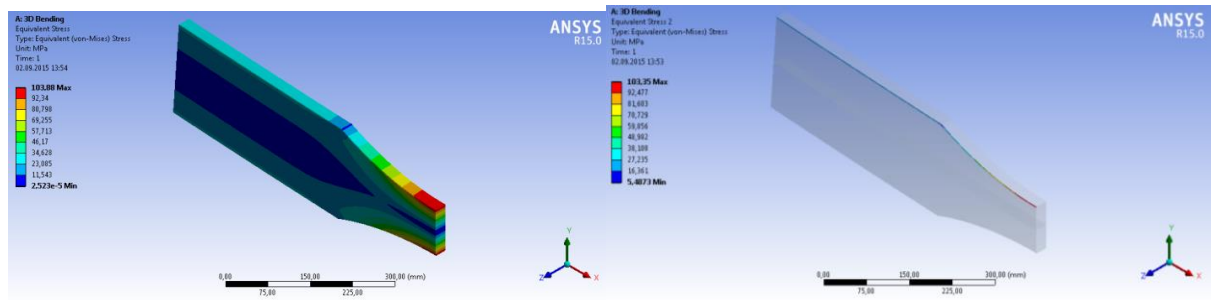
Result for 3D Ref Bending with Thickness 50mm



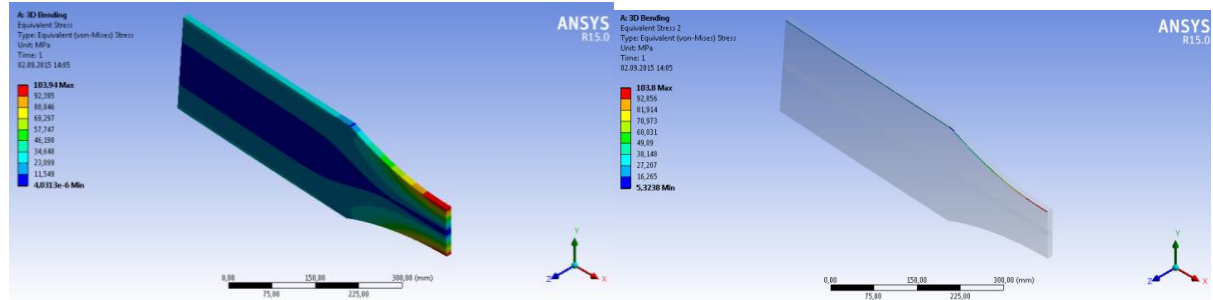
Result for 3D Ref Bending with Thickness 25mm



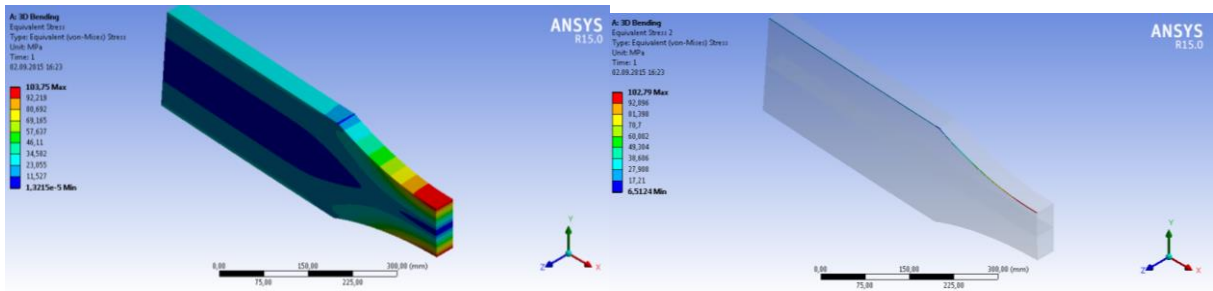
Result for 3D Bending 1C with Thickness 80mm



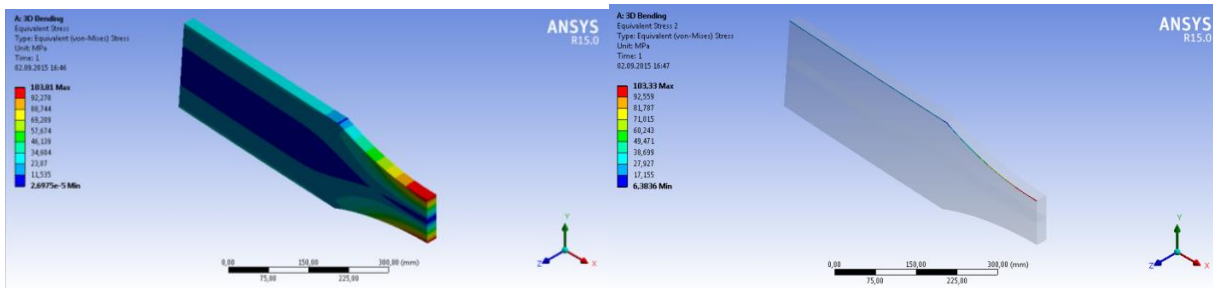
Result for 3D Bending 1C with Thickness 50mm



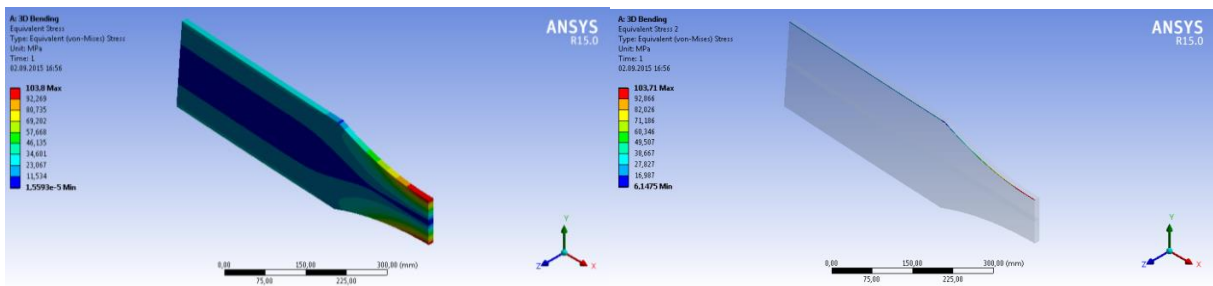
Result for 3D Bending 1C with Thickness 25mm



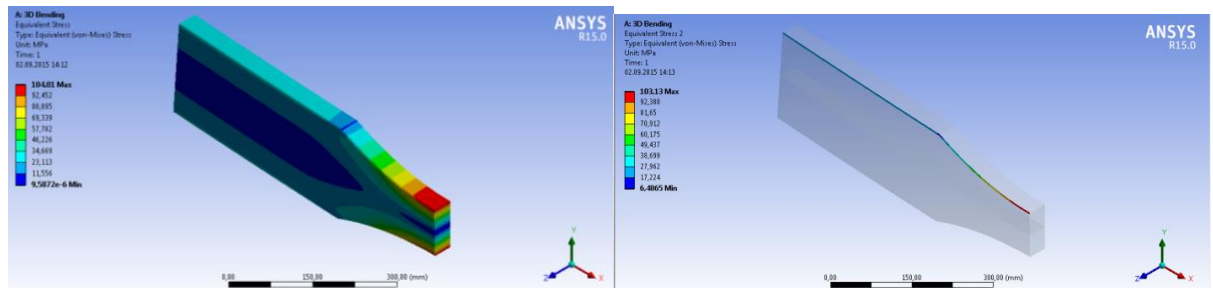
Result for 3D Bending 1R with Thickness 80mm



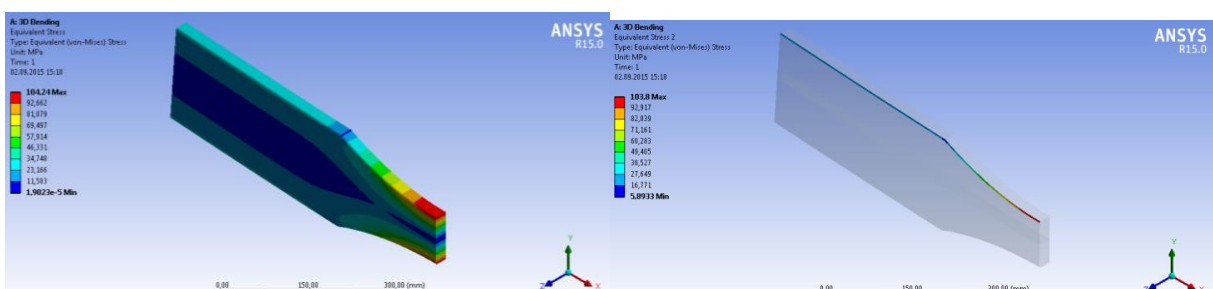
Result for 3D Bending 1R with Thickness 50mm



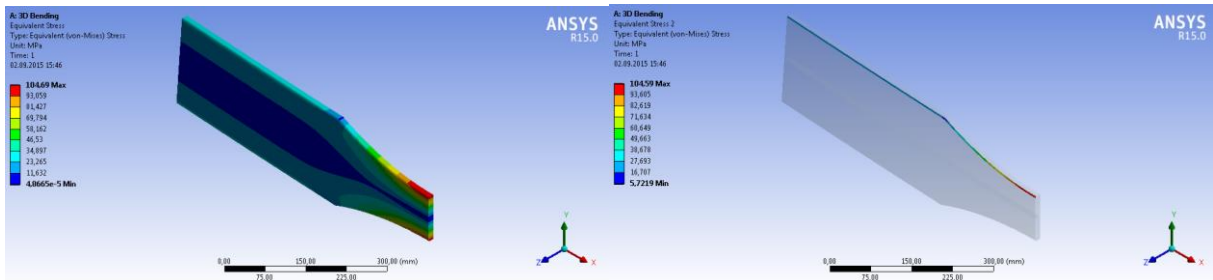
Result for 3D Bending 1R with Thickness 25mm



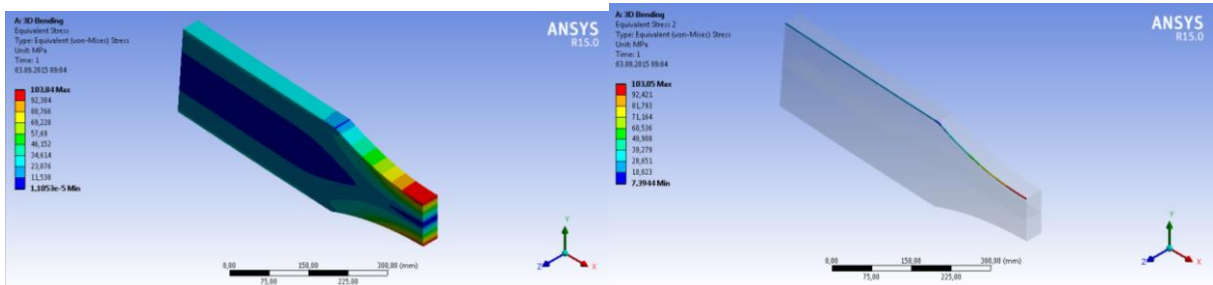
Result for 3D Bending 2C with Thickness 80mm



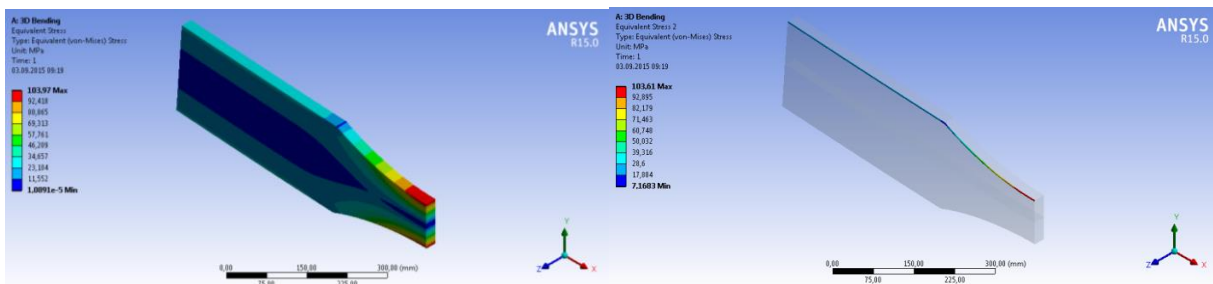
Result for 3D Bending 2C with Thickness 50mm



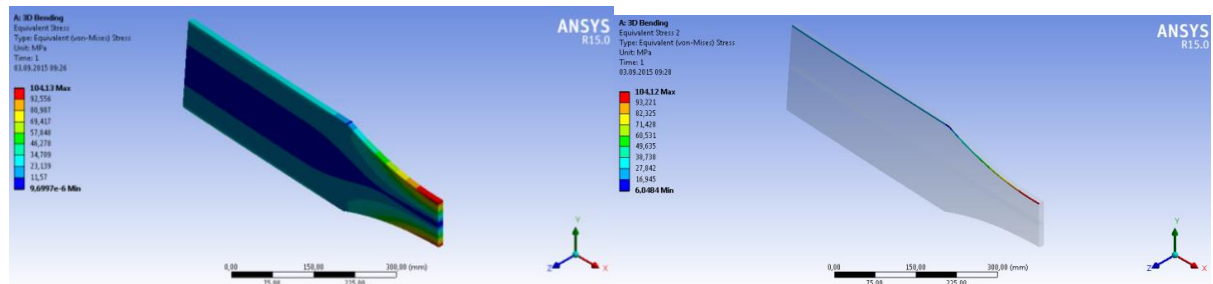
Result for 3D Bending 2C with Thickness 25mm



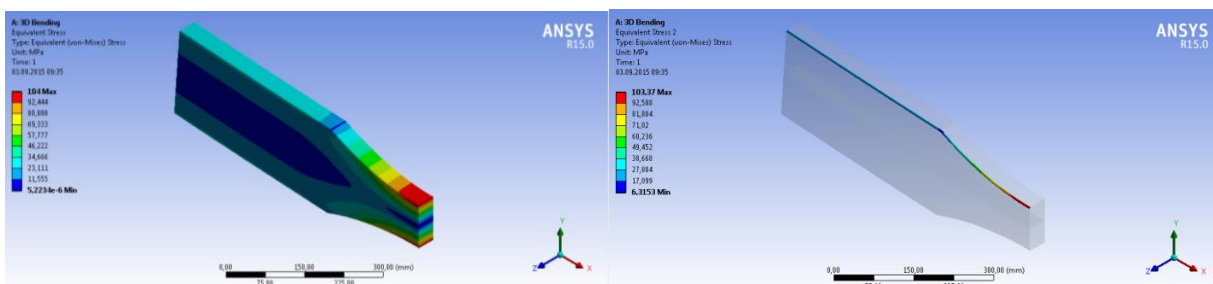
Result for 3D Bending 2R with Thickness 80mm



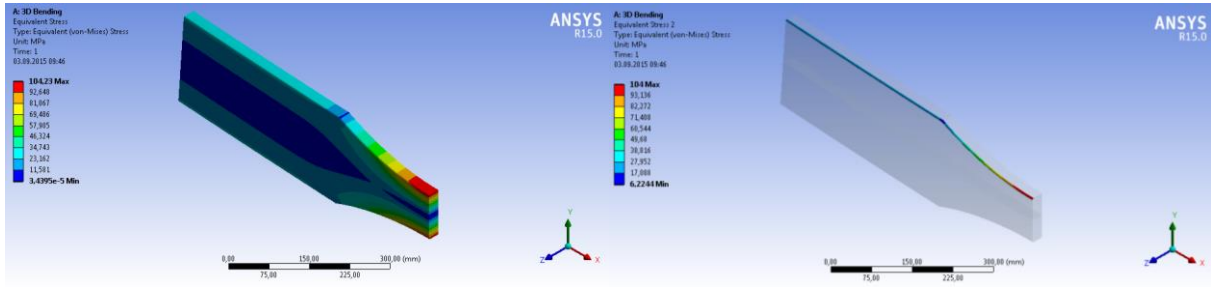
Result for 3D Bending 2R with Thickness 50mm



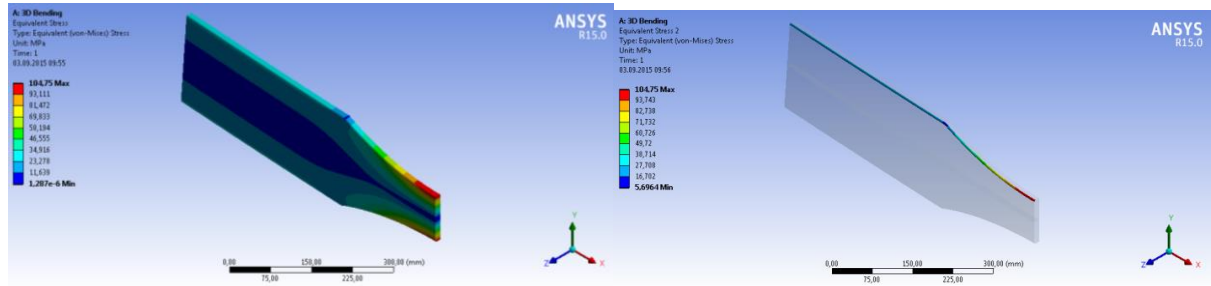
Result for 3D Bending 2R with Thickness 25mm



Result for 3D Bending 3R with Thickness 80mm

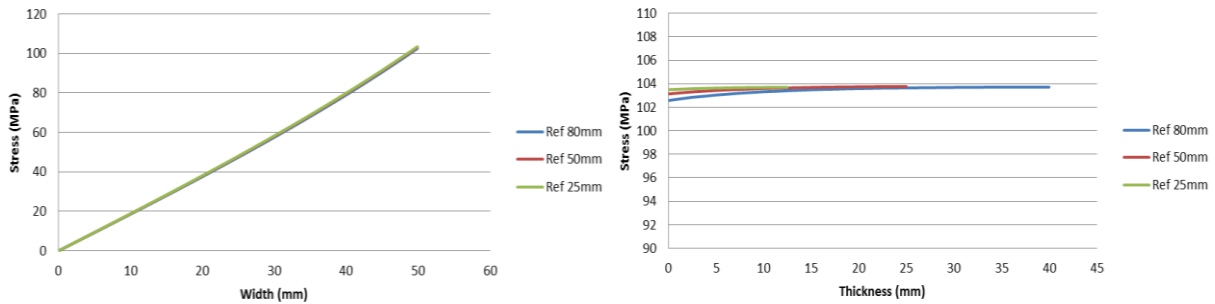


Result for 3D Bending 3R with Thickness 50mm

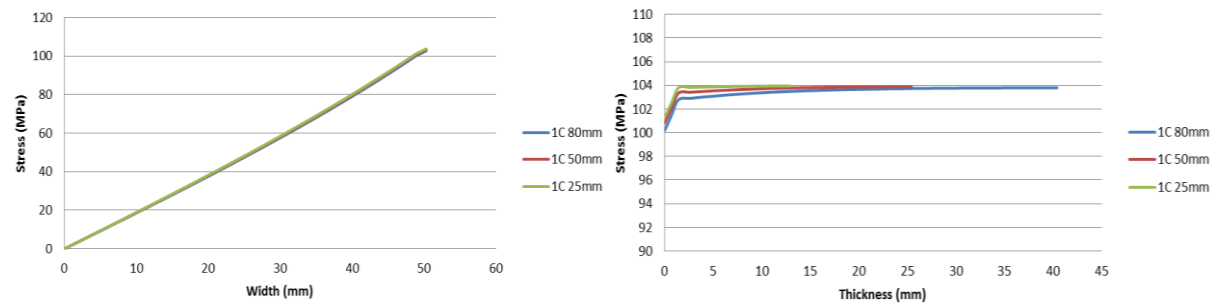


Result for 3D Bending 3R with Thickness 25mm

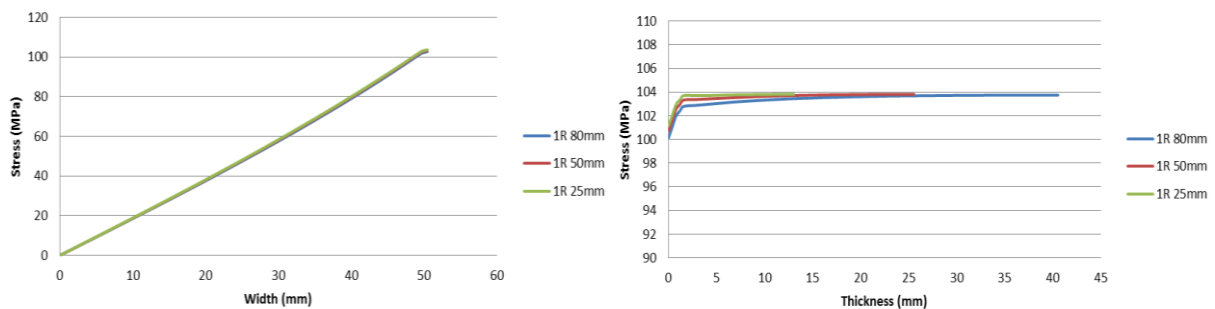
Stress Distribution for Bending Simulation



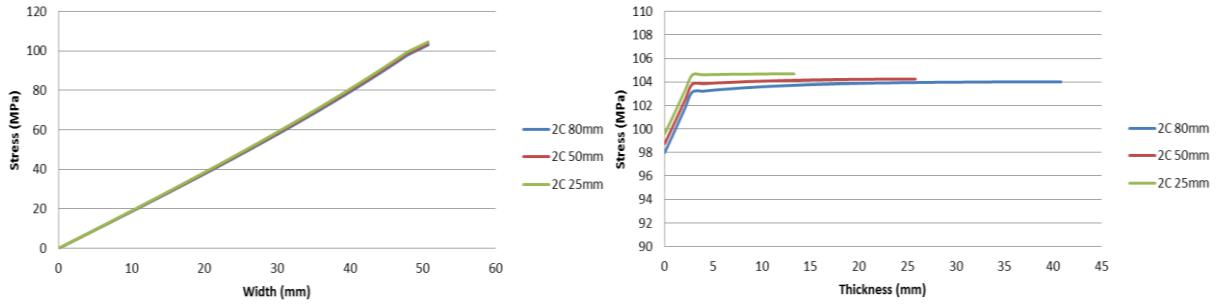
Bending 3D Ref Model Equivalent Stress Variation with Respect to Width and Thickness



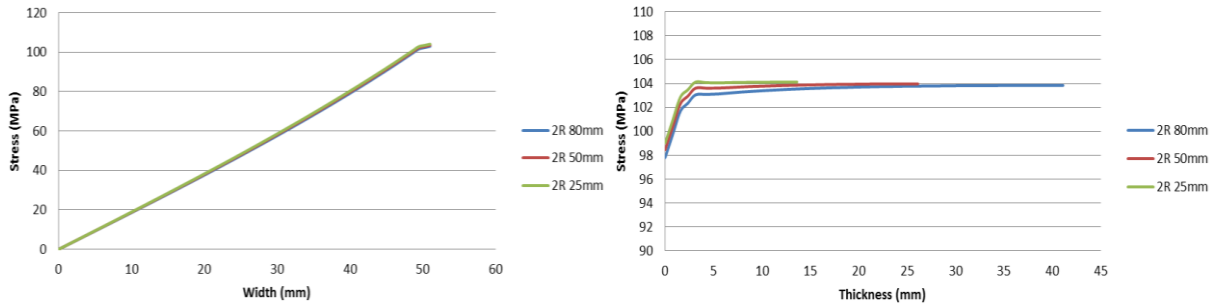
Bending 3D 1C Model Equivalent Stress Variation with Respect to Width and Thickness



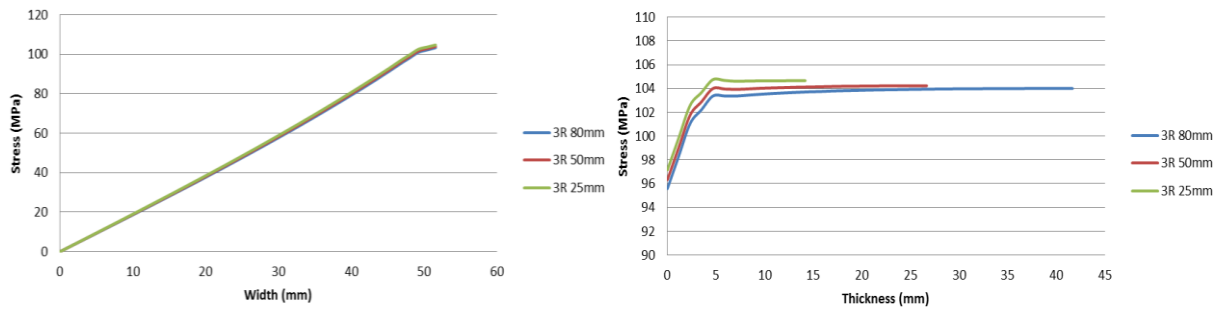
Bending 3D 1R Model Equivalent Stress Variation with Respect to Width and Thickness



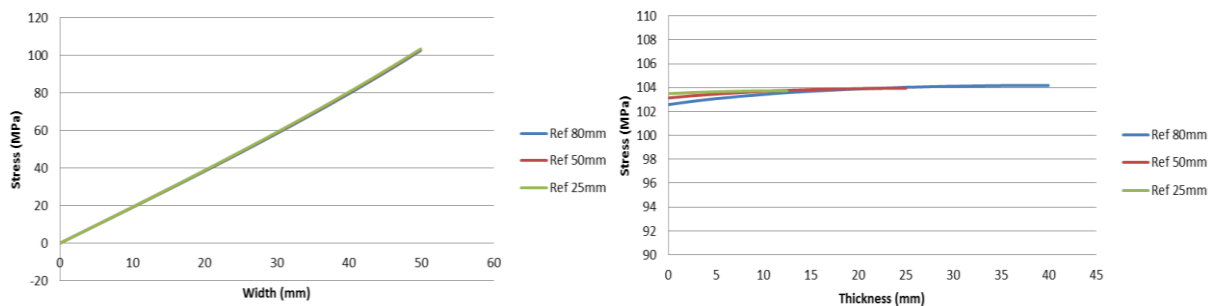
Bending 3D 2C Model Equivalent Stress Variation with Respect to Width and Thickness



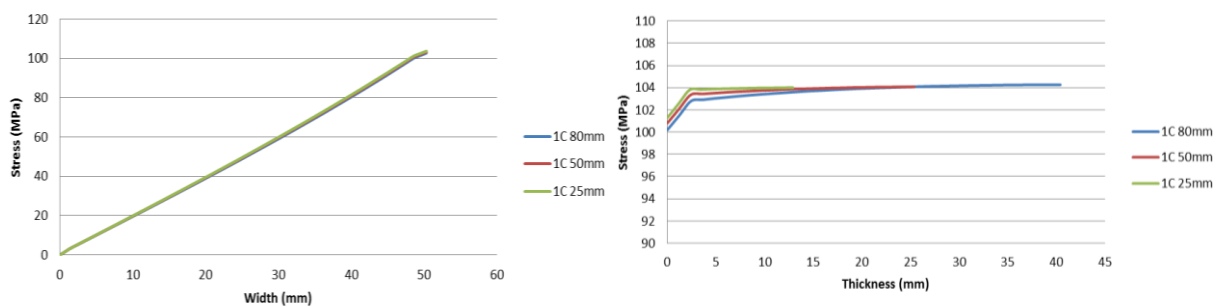
Bending 3D 2R Model Equivalent Stress Variation with Respect to Width and Thickness



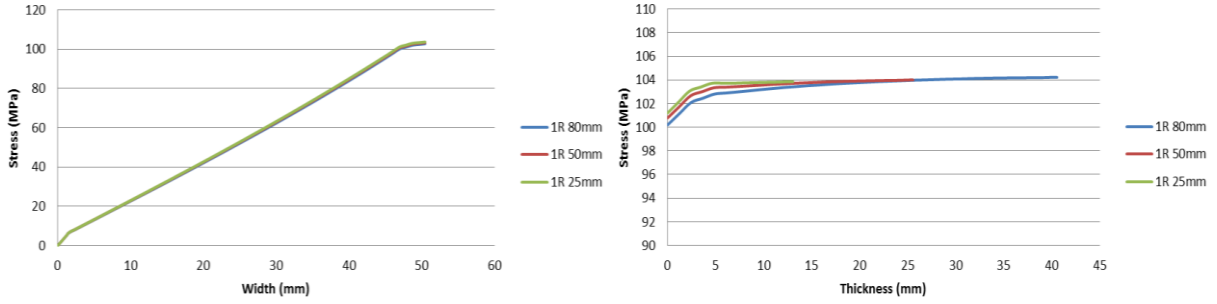
Bending 3D 3R Model Equivalent Stress Variation with Respect to Width and Thickness



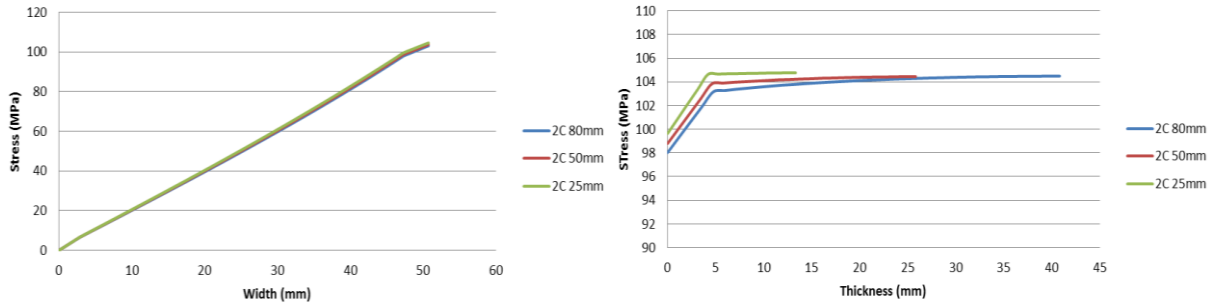
Bending 3D Ref Model Normal Stress Variation with Respect to Width and Thickness



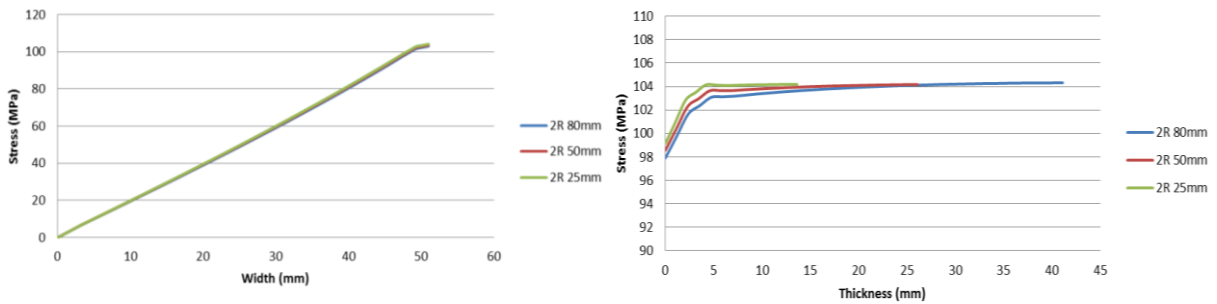
Bending 3D 1C Model Normal Stress Variation with Respect to Width and Thickness



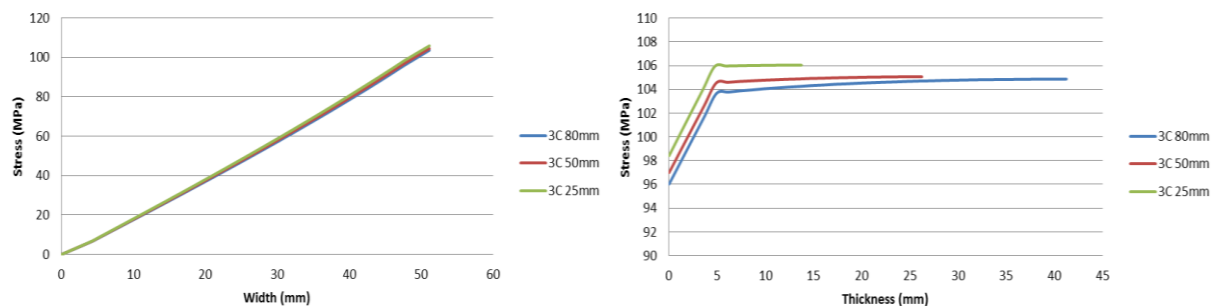
Bending 3D 1R Model Normal Stress Variation with Respect to Width and Thickness



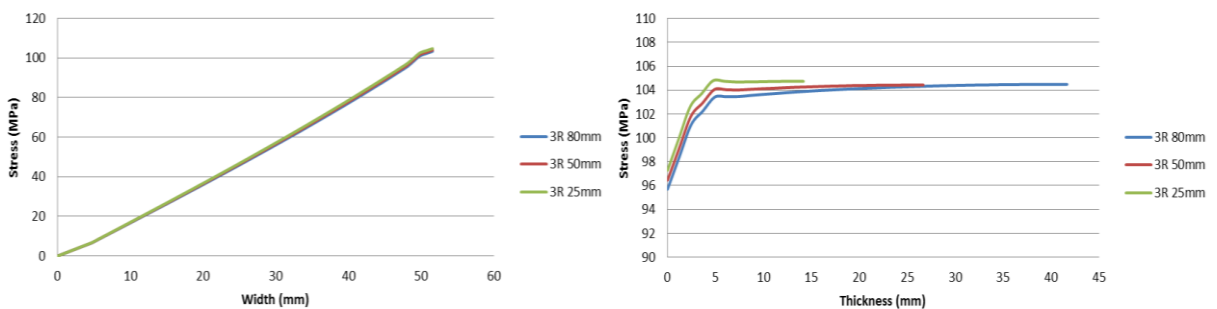
Bending 3D 2C Model Normal Stress Variation with Respect to Width and Thickness



Bending 3D 2R Model Normal Stress Variation with Respect to Width and Thickness



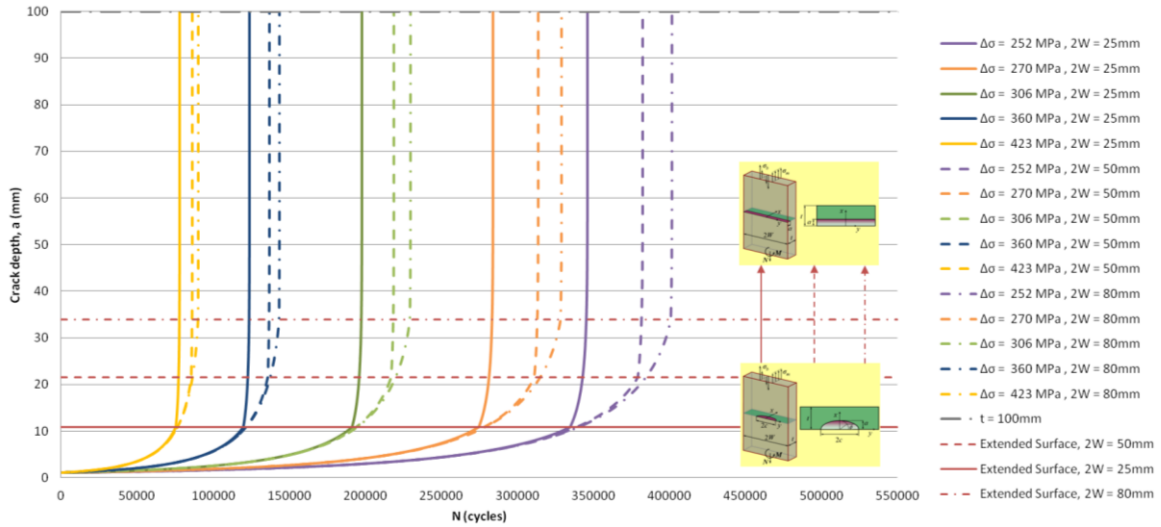
Bending 3D 3C Model Normal Stress Variation with Respect to Width and Thickness



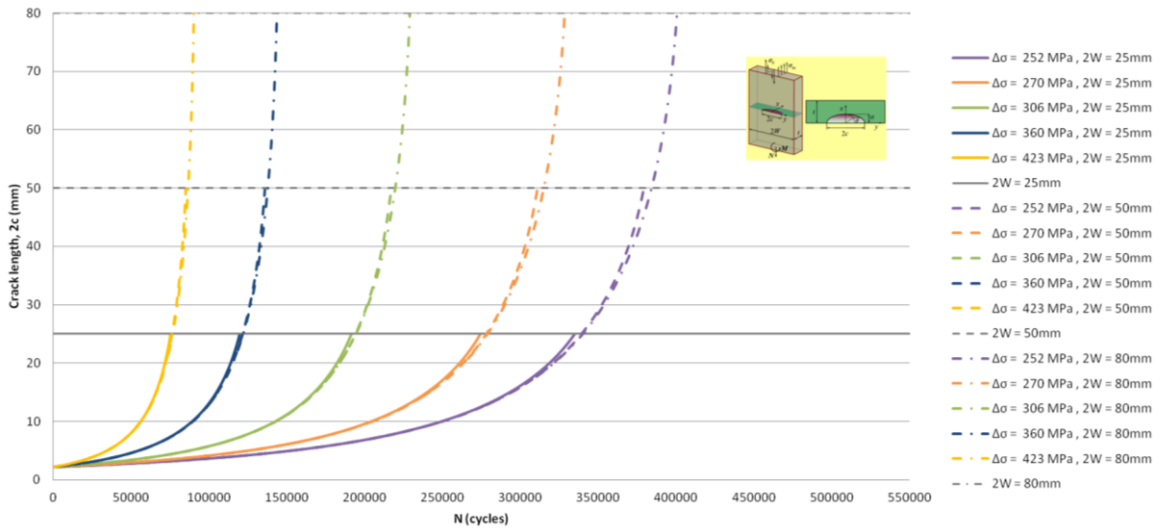
Bending 3D 3R Model Normal Stress Variation with Respect to Width and Thickness

Crack Propagation Analysis of Thermal Cut Edge Specimen

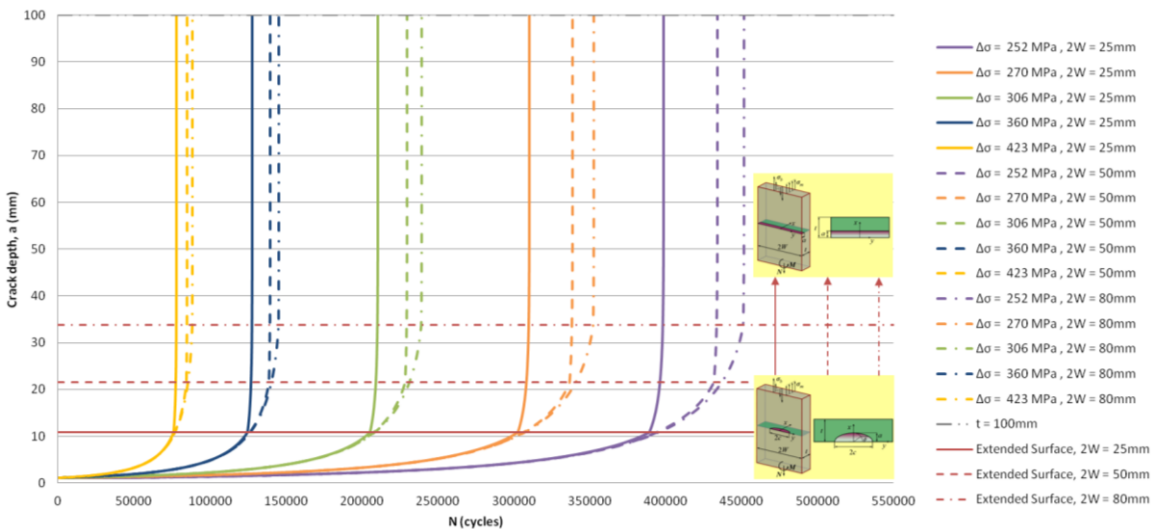
Thermal Cut Edge Crack Propagation Analysis for Axial Load



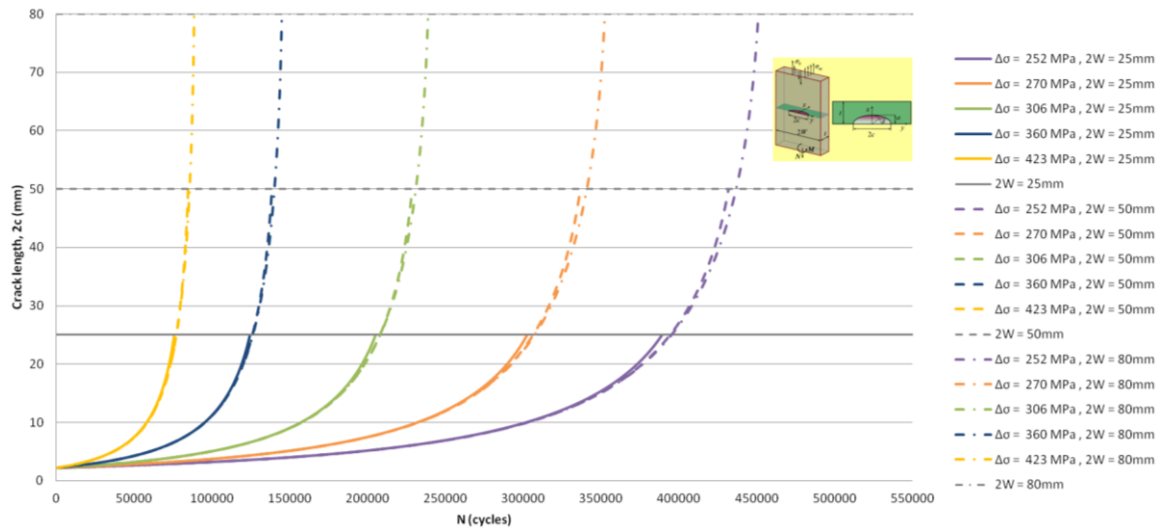
Semi-Elliptical Crack Depth Propagation for YP36 for Different Stress Ranges under Axial Load



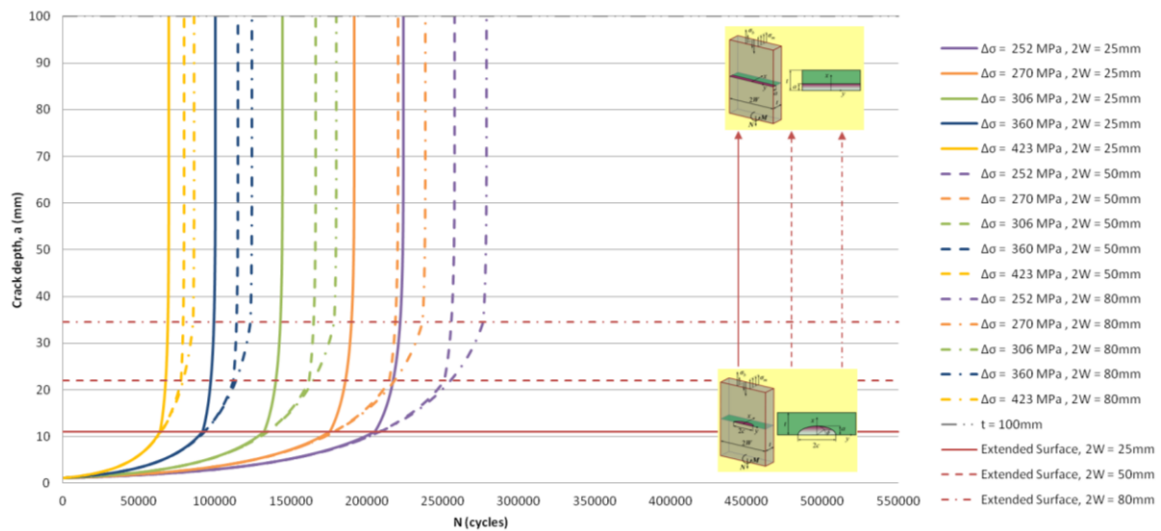
Semi-Elliptical Crack Length Propagation for YP36 for Different Stress Ranges under Axial Load



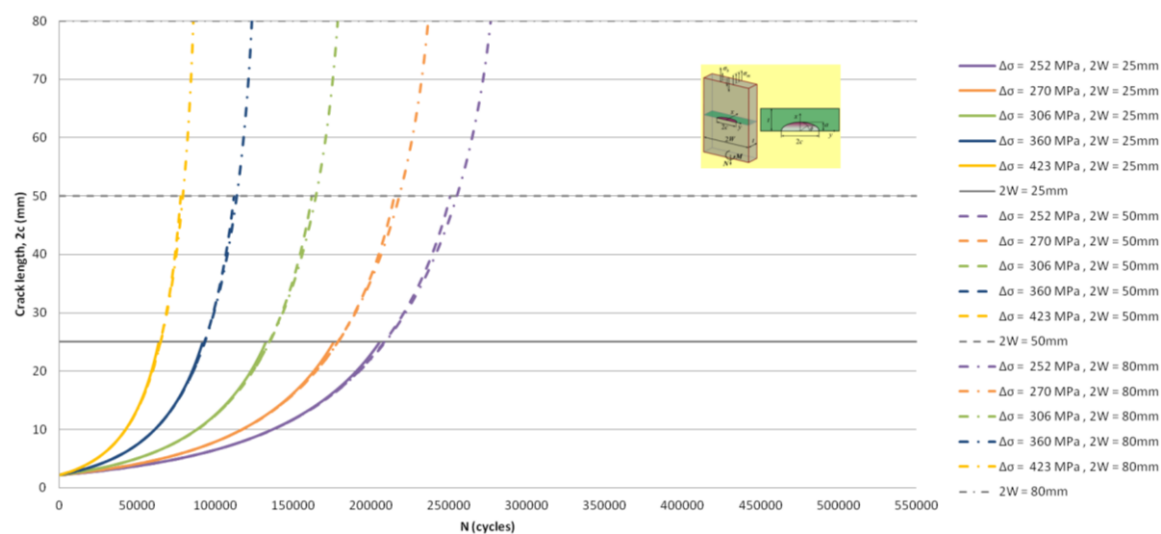
Semi-Elliptical Crack Depth Propagation for YP40 for Different Stress Ranges under Axial Load



Semi-Elliptical Crack Length Propagation for YP40 for Different Stress Ranges under Axial Load

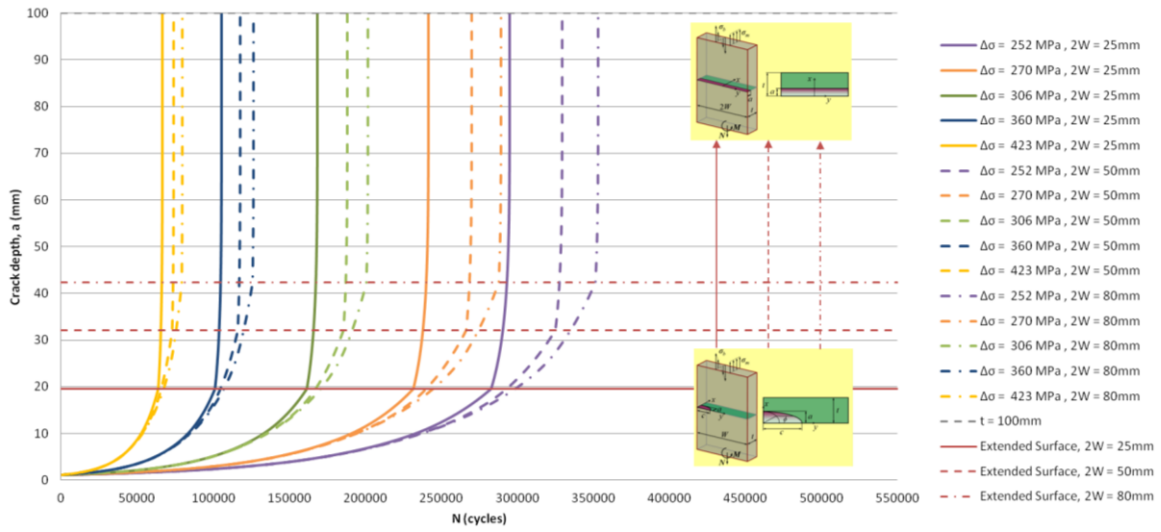


Semi-Elliptical Crack Depth Propagation for YP47 for Different Stress Ranges under Axial Load

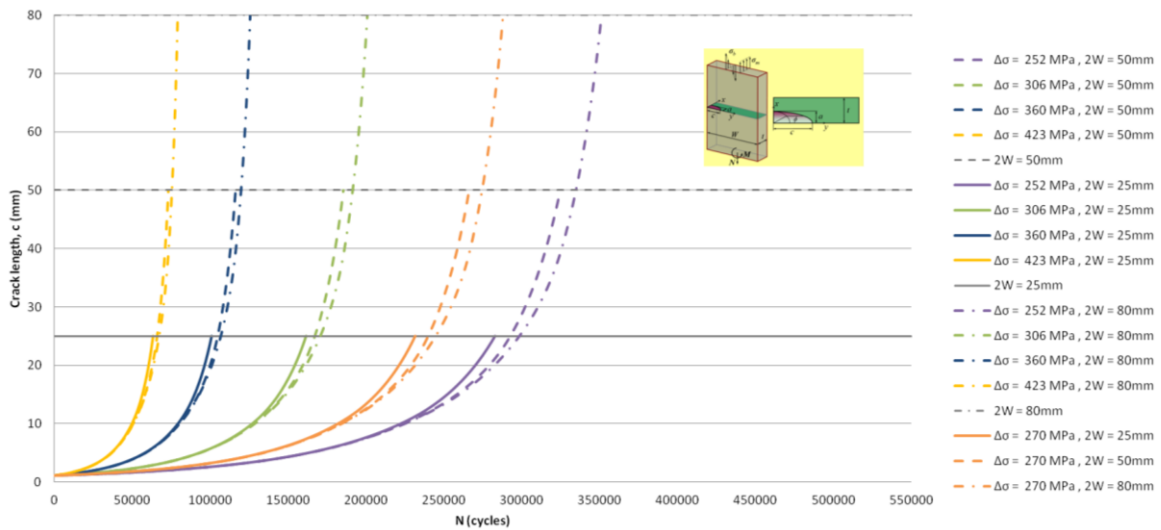


Semi-Elliptical Crack Length Propagation for YP47 for Different Stress Ranges under Axial Load

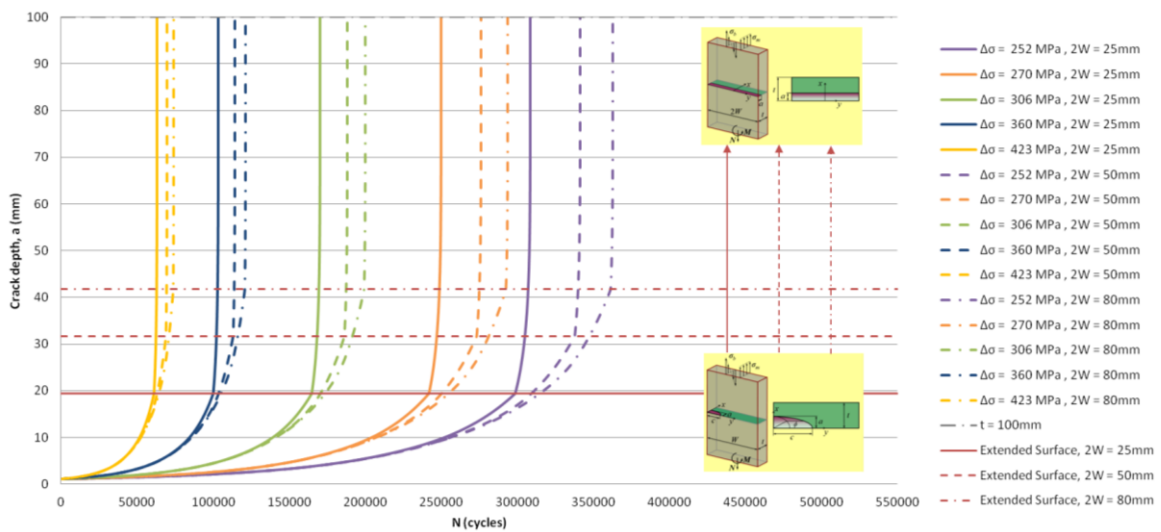
Thermal Cut Edge Crack Propagation Analysis for Bending Load



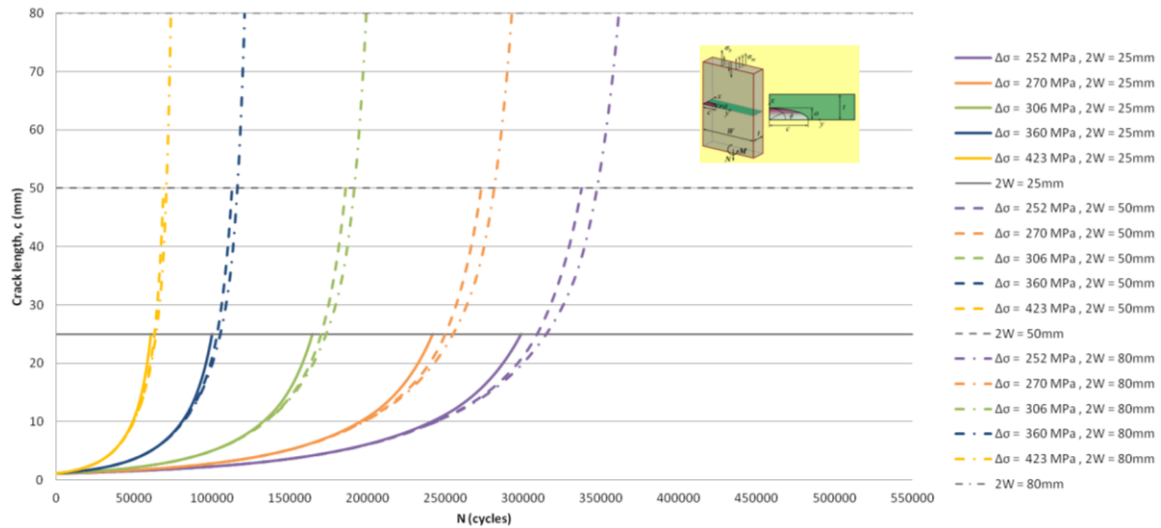
Corner-Elliptical Crack Depth Propagation for YP36 for Different Stress Ranges under Bending Load



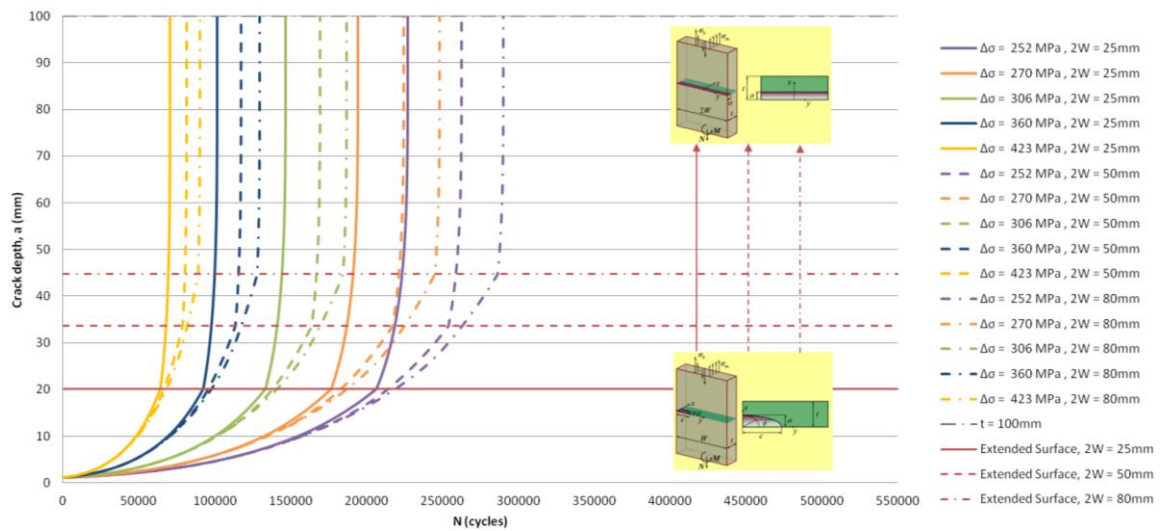
Corner-Elliptical Crack Length Propagation for YP36 for Different Stress Ranges under Bending Load



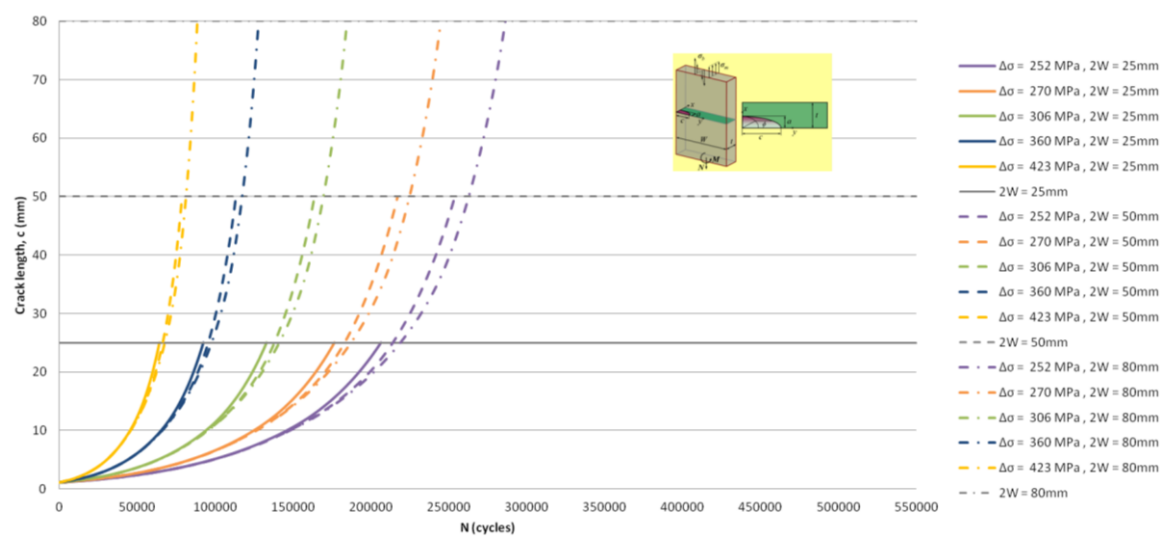
Corner-Elliptical Crack Depth Propagation for YP40 for Different Stress Ranges under Bending Load



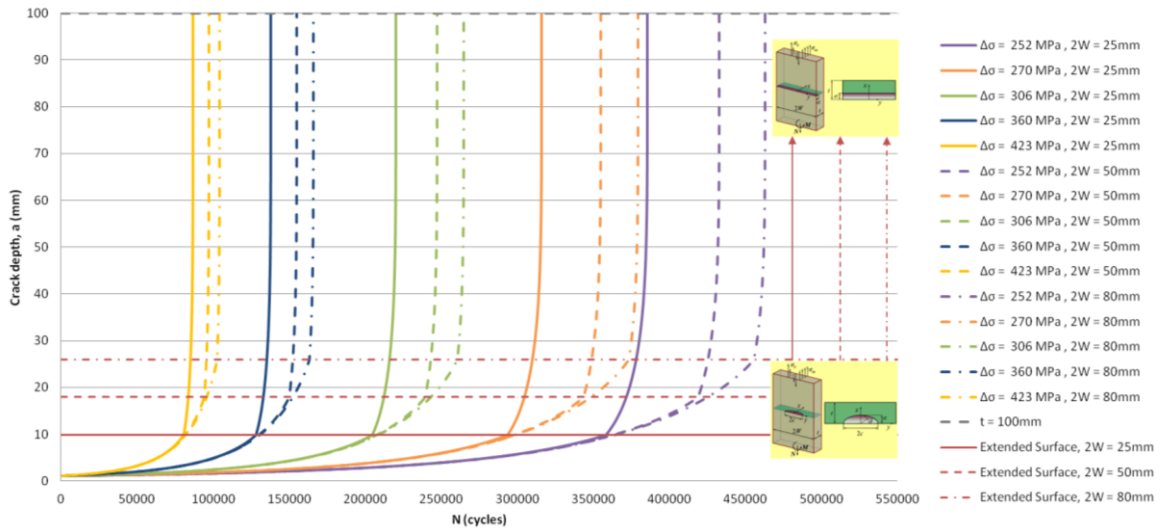
Corner-Elliptical Crack Length Propagation for YP40 for Different Stress Ranges under Bending Load



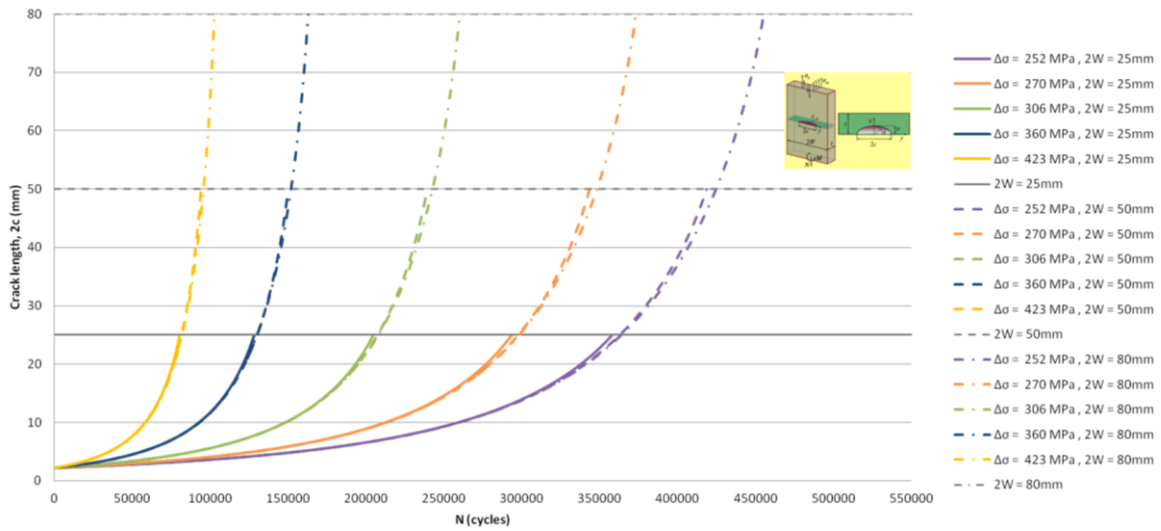
Corner-Elliptical Crack Depth Propagation for YP47 for Different Stress Ranges under Bending Load



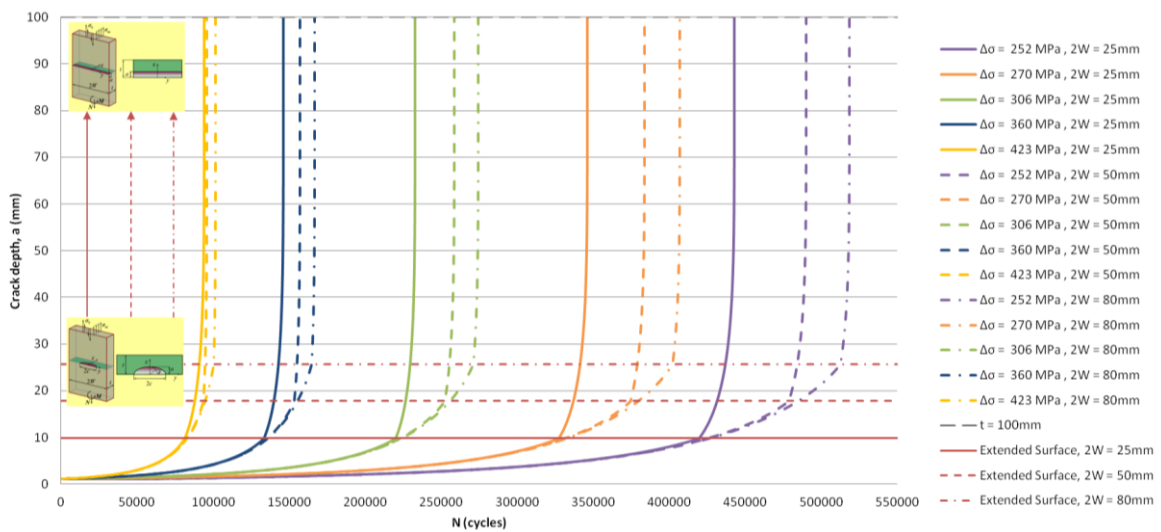
Corner-Elliptical Crack Length Propagation for YP47 for Different Stress Ranges under Bending Load



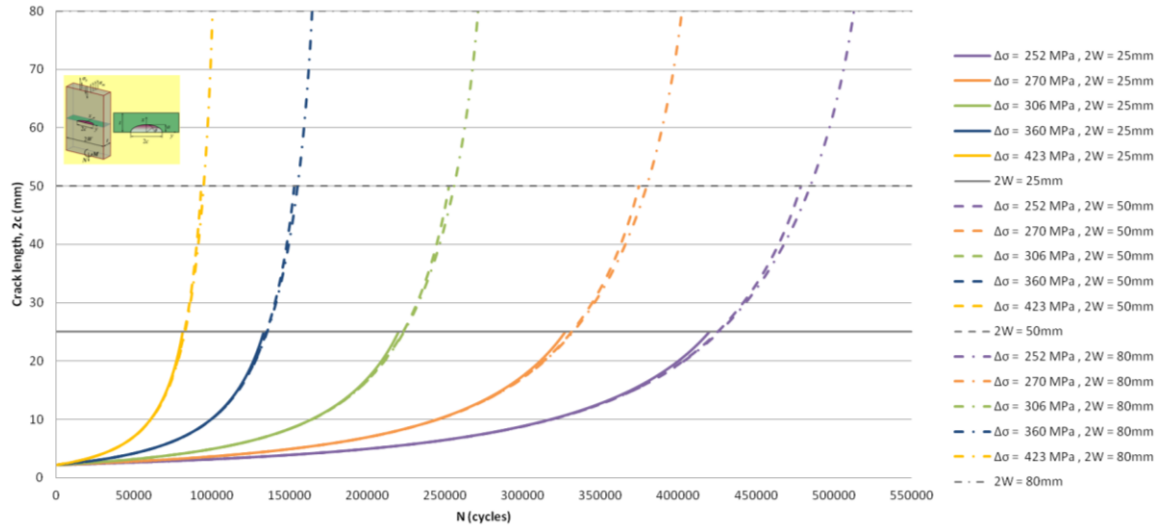
Semi-Elliptical Crack Depth Propagation for YP36 for Different Stress Ranges under Bending Load



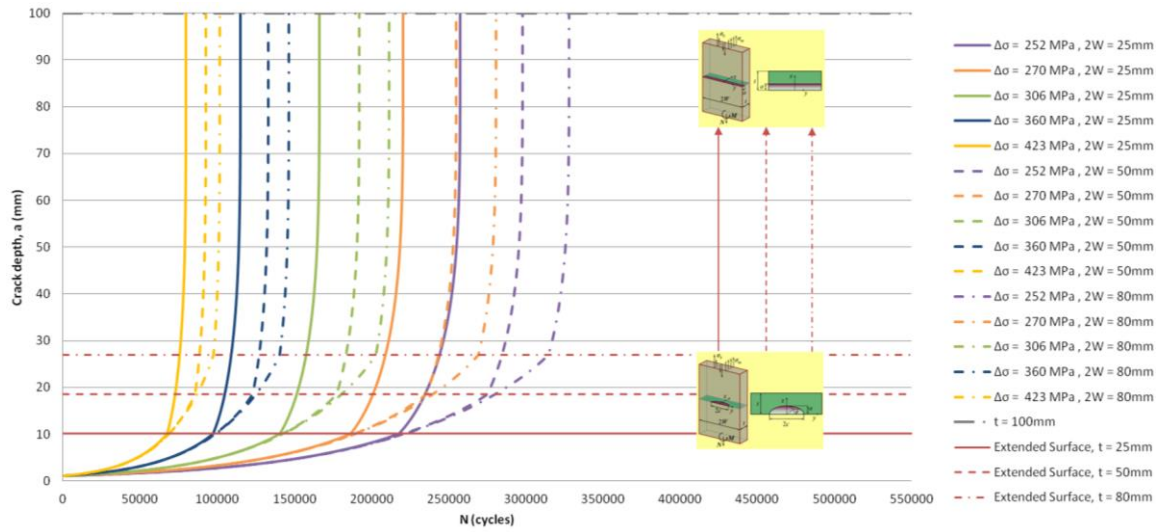
Semi-Elliptical Crack Length Propagation for YP36 for Different Stress Ranges under Bending Load



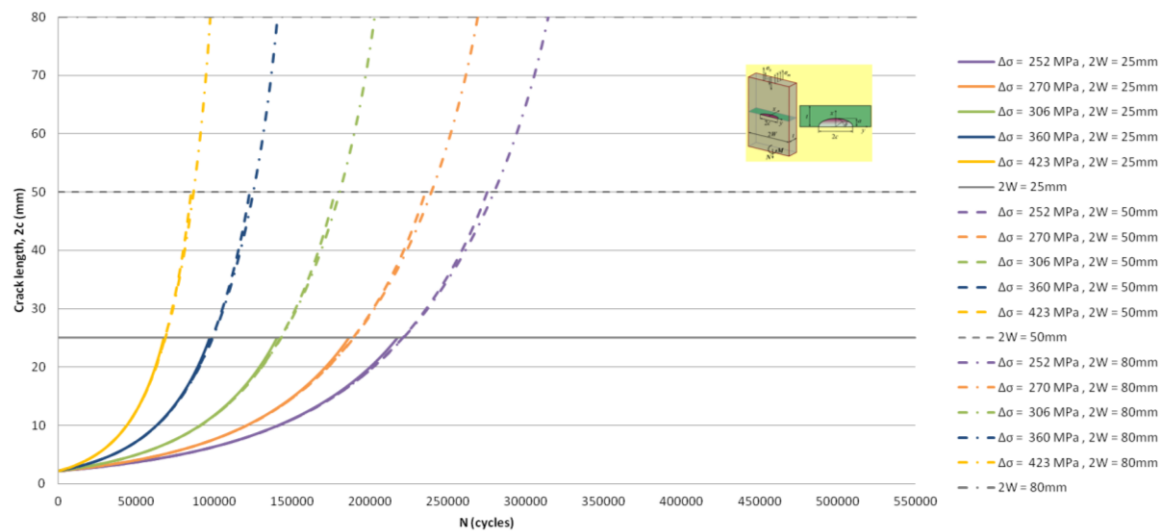
Semi-Elliptical Crack Depth Propagation for YP40 for Different Stress Ranges under Bending Load



Semi-Elliptical Crack Length Propagation for YP40 for Different Stress Ranges under Bending Load



Semi-Elliptical Crack Depth Propagation for YP47 for Different Stress Ranges under Bending Load



Semi-Elliptical Crack Length Propagation for YP47 for Different Stress Ranges under Bending Load